A STRAIN ENERGY BASED MULTIAXIAL HIGH-CYCLE FATIGUE LIFE EVALUATION MODEL FOR NOTCHED STRUCTURES

by

Burak Gezer

B.S, Mechanical Engineering, Yıldız Technical University, 2015

Submitted to the Institute for Graduate Studies in
Science and Engineering in partial fulfillment of
the requirements for the degree of
Master of Science

Graduate Program in Mechanical Engineering
Boğaziçi University

2020

This study is dedicated to two special women, meaning of my life, my mother Derya Çölmen and my sister Burcu Gezer. You have made me stronger and better than I could have ever imagined. I love you to the moon and back.

ACKNOWLEDGEMENTS

I would first like to express my sincere gratitude to my supervisor, Prof. Fazıl Önder Sönmez, for his guidance and support throughout my thesis study.

I also thank the committee members, Prof. Halit Süleyman Türkmen and Prof. Nuri Ersoy, for their comments and suggestions.

I owe my dear friend Kayhan Kömür a debt of gratitude for his contributions in my thesis and his emotional support.

ABSTRACT

A STRAIN ENERGY BASED MULTIAXIAL HIGH-CYCLE FATIGUE LIFE EVALUATION MODEL FOR NOTCHED STRUCTURES

In this study, a model is presented for high-cycle fatigue-life assessment of notched engineering components subjected to constant amplitude multiaxial proportional loads. The algorithm requires only material-dependent parameters available in material data sheets. Applicability of the proposed approach is independent of any experimentally determined factor for geometry as well as loading conditions. Instead, the effects of such factors are taken into consideration in this study through a newly introduced parameter called equivalent strain energy density. The formalized fatigue design methodology estimates the fatigue life by directly using elastic stress and strain fields around the notch in conjunction with Coffin-Manson-Basquin law. Stress/strain states developed in the part are determined via linear elastic finite element analysis. Predictions of the presented model are compared with many experimental results reported in the literature for specimens with various notch geometries made of different materials, including aluminium alloys and steels, subjected to different types of multi-axial loads and a remarkable level of accuracy is reached.

ÖZET

ÇENTİKLİ YAPILAR İÇİN GERİNİM ENERJİSİ TEMELLİ ÇOK EKSENLİ YÜKSEK DÖNGÜ YORULMA ÖMRÜ TAHMİN MODELİ

Bu çalışmada, sabit genlikli çok eksenli orantısal yüklemelere maruz kalan çentikli yapıların yüksek devir yorulma ömrü değerlendirmesi için bir model sunulmuştur. Algoritma yalnızca, malzeme veri tabanlarında mevcut olan malzemeye bağlı parametrelere ihtiyaç duymaktadır. Önerilen yaklaşımın uygulanabilirliği, geometriye ya da yükleme koşullarına dayalı olarak belirlenmiş herhangi bir deneysel faktörden bağımsızdır. Bunun yerine, bu tür unsurların etkileri, mevcut çalışmada geliştirilmiş olan eşdeğer gerilim enerji yoğunluğu adı verilen bir parametre ile hesaba katılmıştır. Formüle edilen yorulma tasarım metodolojisi, yorulma işlem bölgesine etki eden doğrusal elastik gerilim ve gerinim durumlarını doğrudan Coffin-Manson-Basquin yasası ile birlikte kullanarak yorulma ömrünü tahmin eder. Parça üzerinde hâkim olan gerilme / gerinim durumları lineer elastik sonlu elemanlar analizi ile belirlenir. Sunulan modelin tahminleri, farklı çok eksenli yüklere tabi tutulan, alüminyum alaşımı ve çelik gibi farklı malzemelerden yapılmış çeşitli çentik geometrilerine sahip örnekler için literatürde rapor edilen birçok deneysel sonuçla karşılaştırılmıştır ve dikkate değer bir doğruluk seviyesine ulaşılmıştır.

TABLE OF CONTENTS

LIST OF FIGURES

LIST OF TABLES

LIST OF SYMBOLS

a	Crack length
b	Axial fatigue strength exponent
b_0	Shear fatigue strength exponent
c	Axial fatigue ductility exponent
c_0	Shear fatigue ductility exponent
$D, \boldsymbol{D}, D_f$	Damage parameter
E	Elastic modulus
E_{RMS}	Root mean square logarithmic error
G	Shear modulus
K'	Coefficient of cyclic strain hardening
n	Total number of the examined measurements
n'	Exponent of cyclic strain hardening
N_f	Number of cycles to failure
N_f^{th}	Material endurance limit
R	Pearson's correlation coefficient
R	Cyclic stress ratio (Minimum stress/ Maximum stress)
R_m	Mean-stress factor
T_{RMS}	Mean square error
U	Strain energy density (elastic, plastic, total, alternating, averaged, threshold, equivalent or element base strain energy density depending on the subscripts and/or superscripts)
V	Volume (material or element base volume depending on the subscripts and/or superscripts)
V'	Volume of the high-energy region
W	Strain energy density
ΔK	Stress intensity factor
γ	Shear strain
γ_f'	Shear fatigue ductility coefficient

ε	Strain (elastic, plastic, total, maximum, principal, alternating, mean, Von-Mises equivalent, necking or normal strain depending on the subscripts and/or superscripts)
ε_f'	Axial fatigue ductility coefficient
λ	Biaxiality ratio
v	Poisson's ratio
ρ	Stress ratio (Normal stress/Shear stress)
ρ^*	Notch tip radius
σ	Stress (elastic, plastic, total, maximum, principal, alternating, mean, Von-Mises equivalent, hydrostatic, necking, normal stress or fatigue strength depending on the subscripts and/or superscripts)
σ_f'	Axial fatigue strength coefficient
σ_u	Ultimate tensile strength
σ_y	Yield strength
τ	Shear stress
τ_f'	Shear fatigue strength coefficient
ϕ	Phase angle

LIST OF ACRONYMS / ABBREVIATIONS

2D	Two Dimensional
3D	Three Dimensional
AM	Area Method
APDL	ANSYS Parametric Design Language
ASTM	American Society for Testing and Materials
CDM	Continuum Damage Mechanics
CS	Carpinteri-Spagnoli (Criterion)
DBCS	Dugdale Bilby Cottrell Swinden (Model)
FEM	Finite Element Modeling
FS	Fatemi-Socie (Parameter)
LM	Line Method
MCC	Minimum Circumscribed Circle (Concept)
MMCCM	Modified Manson-Coffin Curve Method
MWCM	Modified Wöhler Curve Method
PM	Point Method
SWT	Smith-Watson-Topper (Parameter)
TCD	Theory of Critical Distances
VM	Volume Method

1. INTRODUCTION

Most mechanical components experience repeated loads and then accumulation of microscopic damage caused by the resulting cyclic stresses eventually leads to fatigue fracture. Considering fatigue is the critical mode of failure in many engineering applications, a successful design process requires an effective fatigue assessment. Response of a structure to time varying effects highly depends on the material type as well as the geometry and loading conditions. Extensive studies in recent years have provided a deeper understanding of the fatigue problem. On the other hand, the challenging nature of this problem has not yet allowed a universal consensus to be reached.

An important difficulty encountered in fatigue-life estimation is irregular structure geometries. Many structural elements include geometric discontinuities, i.e. notches, leading to stress concentration, such as grooves, fillets, holes, and keyways. A notch may significantly reduce the fatigue life of a part. A fatigue-assessment model should correctly account for the effect of such a stress raiser. In order to account for the notch effect, many conventional methodologies in the literature either use experimentally determined coefficients that relate the data for smooth specimen to the notched one or directly include parameters depending on the notch geometry [1,2]. This seriously limits their applicability considering that, such values are available only for common geometries. Then, each new non-standard notch geometry requires a new experimental verification.

Another major challenge to be overcome in fatigue assessment is complex stress states. Unlike laboratory specimens, mechanical components are mostly subjected to quite complex multiaxial loads. Transmission shafts, which are rotating machine elements providing transmission of power and torque, and turbine blades are common machine elements subjected to combined torsion and bending. Also, rotor shaft of a helicopter, which drives rotor blades to provide lifting force, can be given as an example for structures subjected to various combinations of axial and torsional loads. Even if the externally applied load is uniaxial, a multiaxial stress state develops around a stress raiser. A generally applicable model should be able to predict the fatigue life of a part without resorting to experimentally

determined load and geometry factors. Increased dependence of a model to experimentally determined coefficients reduces its applicability.

Apart from its applicability to a wide range of geometries under various loading conditions, a model should be able to estimate the fatigue life using the readily available material properties. Many models highly recognized in the literature contain one or more additional material constants that are usually obtained by fitting the uniaxial experimental data [3-5]. This brings an additional workload and limits the use of such a model in industrial applications.

Many of the models proposed in the literature requires nonlinear structure analysis to determine the local plastic stress and strain states around the notch. This poses difficulty in industrial applications, if the part is large, computational burden of a nonlinear analysis will be high.

In the light of these problems that designers face, this study reports on an attempt to develop an alternative technique to accurately estimate the fatigue life of mechanical parts under constant-amplitude multiaxial loading conditions in the high cycle range. The presented fatigue assessment methodology does not include any loading or geometry-dependent parameters and in this way, it can be applied to nonstandard and irregularly shaped structures under a wide variety of loading conditions. The proposed model also uses only the material properties available in material data sheets. Fatigue-strength coefficient and exponent are the only material properties needed to apply the model. Nonlinear plastic structural analysis is not required. A linear analysis for calculating strain energy state around the notch is sufficient to apply the model.

As a final point to be noted, the proposed model in this study is a modified and improved version of the model previously developed by Sönmez and Karadeniz [6,7].

2. LITERATURE REVIEW

In recent years, increasing attention has been given to the study of multiaxial fatigue. Current studies can conventionally be classified as stress-strain based, energy based and fracture mechanics criteria. However, such a classification is deliberately avoided here because some studies involve multiple number of models built on different parameters. Instead, existing studies will be treated under the titles of continuum mechanics criteria and fracture mechanics criteria, which are related to crack nucleation and propagation phases, respectively.

2.1. Continuum Mechanics Criteria

In this section, crack initiation issue is addressed under the continuum mechanics framework. Theory of Critical Distances (TCD), Continuum Damage Mechanics (CDM) and critical plane approach, which are widely used in the literature, will be discussed briefly. However, as the current trend is concentrated in certain methods and some models are a combination of multiple methods, such an extra subcategorization will not be attempted. Relevant approaches will be outlined in detail in chronological order as much as possible. Similar approaches will be reviewed together. It is worth noting that the models that will be mentioned in this section may include large amount of material plasticity i.e. propagation stage. The criterion here is that the fatigue process has been handled from the very beginning.

The foundations of the theory of critical distances (TCD), which is an approach used to predict the effects of stress raisers on fatigue behaviour, were first laid by Neuber [8,9]. Assuming the elastic stress in the vicinity of stress raisers does not reach those values figured through the continuum mechanics theory, Neuber postulated that average of the elastic stress acting along a critical distance from the notch root is the effective stress damaging the fatigue process zone. Afterwards, Peterson [10] advanced a simplified way to apply Neuber's line method (LM). He suggested that the stress controlling the fatigue failure is not an averaged elastic stress over a critical distance from the hot-spot, but rather the stress state at a point located at a certain distance from the notch core (PM). Recently, Taylor [11] and Bellet [12], adopting a similar approach, averaged the elastic stress over semi-circular area and half

sphere which are centred at the apex of the stress, respectively. Their models are classified in the literature as area method (AM) and volume method (VM), respectively.

The nucleation, growth, accumulation and, ultimately, merging of the microcavities in the material not only induce the crack initiation process, but also cause deterioration in the mechanical properties of the material like decrease in strength, toughness, stability, rigidity. This type of deterioration is called material damage. The studies conducted by Hult [13], Lemaitre and Chaboche [14], Lemaitre [15,16], Chaboche [17,18,19], Krajcinovic [20] and, Krajcinovic and Fonseka [21] in the last quarter of the 20th century revealed the physical relationship between the material damage and the mechanical behavior of the material in terms of certain mechanical variables. According to their argument, so-called the theory of damage mechanics, the severity of damage in a mechanical element is represented by a scalar function $\boldsymbol{D}$, which is called damage [22]. Damage is a function of the stress-strain states and, its value varies from zero to one depending on the level of material deterioration.

In conjunction with damage mechanics, the critical plane approach has been accepted in the literature and widely used in practice as it accounts for hardening due to phase changes and its applicability is not confined to metallic materials. The critical plane criterion is an application of the continuum mechanics methods rather than being a new method. After determining the plane most likely to be the crack initiation plane, coordinate transformations are made to evaluate the stress and strain states corresponding to this plane and damage parameter is defined as a function of those values. One of the most striking ideas of determining the critical plane was put forward by Brown and Miller in 1973 [23]. According to their argument, crack initiates on the plane experiencing the maximum shear stress and, propagates along the plane normal to the maximum normal stress direction.

The rest of this section deals with the approaches based on aforementioned methods. Only multi-axial approaches are included in this review. Although some early studies are mentioned, recent approaches are more fully discussed.

In 1987, Socie [24] proposed a successfully modified version of Smith-Watson-Topper parameter (SWT) [25], which is applicable to both proportional and non-proportional multiaxial loadings. Assuming that the critical plane is the plane with the maximum normal

strain range, $\Delta\varepsilon_1$, Socie expressed the normal strain energy density in the critical plane in terms of the maximum principal strain, $\Delta\varepsilon_1$, and the maximum normal stress, $\sigma_{n,max}$, acting on this plane,

$$W_a = \sigma_{n,max}\frac{\Delta\varepsilon_1}{2} = \frac{\sigma_f'^2}{E}\left(2N_f\right)^{2b} + \sigma_f'\varepsilon_f'\left(2N_f\right)^{b+c} \tag{2.1}$$

where σ_f' is the axial fatigue strength coefficient, ε_f' is the axial fatigue ductility coefficient, b is the axial fatigue strength exponent, c is the axial fatigue ductility exponent, and E is the elastic modulus.

Subsequently, Fatemi and Socie [3], inspired by Brown and Miller's critical plane approach [23], came up with a new parameter, so-called Fatemi-Socie parameter (FS parameter). Considering the friction effect induced by the irregular crack surfaces, which is known to extend the fatigue life by reducing stress at the crack tip, they replaced the normal component of the strain in Brown and Miller's model by the normal stresses. Thus, the parameter representing the damage on the plane of maximum shear strain amplitude was formed as a function of maximum normal stress and maximum shear strain amplitude on the critical plane. Fatemi-Socie parameter is expressed as

$$\frac{\Delta\gamma_{max}}{2}\left(1 + k\frac{\sigma_{n,max}}{\sigma_y}\right) = constant \tag{2.2}$$

where $\frac{\Delta\gamma_{max}}{2}$ and $\sigma_{n,max}$ are the maximum shear strain amplitude and the maximum normal stress on the critical plane, respectively, and σ_y is the yield strength. k is the material constant accounting for the impact of normal stress.

Combining the FS parameter with the Manson–Coffin–Basquin relationship, the following fatigue life model can be obtained,

$$\frac{\Delta\gamma_{max}}{2}\left(1 + k\frac{\sigma_{n,max}}{\sigma_y}\right) = \frac{\tau_f'}{G}\left(2N_f\right)^{b_0} + \gamma_f'\left(2N_f\right)^{c_0} \tag{2.3}$$

Fatemi-Socie critical plane model is a commonly used approach because it adequately explains the hardening effect due to non-proportionality and accounts for mean stress effect through the maximum normal stress term.

Afterwards, Shamsaei and Fatemi [26,27] introduced a new model applicable to steels under multiaxial loading by combining the FS parameter [3] with the Roessle-Fatemi hardness method [28] to address the problem of the absence of material fatigue properties, a major challenge encountered in fatigue life calculations. Their Brinell hardness (HB) based life estimation model is given the following,

$$\frac{\Delta\gamma_{max}}{2}\left(1+k\frac{\sigma_{n,max}}{\sigma_y}\right)=\left[A\left(2N_f\right)^{-0.09}+B\left(2N_f\right)^{-0.56}\right]\left[1+kC\left(2N_f\right)^{-0.09}\right] \quad (2.4)$$

This model is formulated under the assumption that the value of the coefficient k in the FS parameter is about 1.0 and the elastic modulus for steel materials is equal to 200,000 MPa. The parameters A, B and C, which are used to represent the common material fatigue parameters such as axial fatigue strength coefficient, are given in terms of Brinell hardness as

$$A=\frac{5.53(HB)+293}{200000} \quad (2.5)$$

$$B=\frac{0.48(HB)^2-731(HB)+286500}{200000} \quad (2.6)$$

$$C=\frac{1}{0.0022(HB)+0.382} \quad (2.7)$$

As a disadvantage, the use of this model is limited to steel materials only.

In 1997, Lagoda and Macha [29] developed a new strain energy density rate parameter, simply be named as the power density of stresses parameter or shortly power parameter. Accordingly, they defined the local notch-tip stress, σ_a, based power parameter as follows,

$$P_a = \left[\frac{\sigma_a^2}{2E} + \frac{1-n'}{1+n'}\sigma_a\left(\frac{\sigma_a}{K'}\right)^{1/n'}\right]\omega \tag{2.8}$$

where ω is an angular frequency, K' is the coefficient of cyclic strain hardening and n' is the exponent of cyclic strain hardening.

One year later, Lagoda and Macha [30] conducted a comprehensive study to examine power parameter model's reliability. They compared their model with the prominent energy models by Neuber [31] and Molski and Glinka [32]. Neuber's parameter of the amplitude of local strain-energy density and the equivalent strain-energy density parameter by Molski and Glinka are as below, respectively,

$$W_{aN} = \frac{\sigma_a^2}{2E} + \frac{\sigma_a}{2[\sigma_a(K')^{-1}]^{1/n'}} \tag{2.9}$$

$$W_{aMG} = \frac{\sigma_a^2}{2E} + \frac{\sigma_a}{1+n'[\sigma_a(K')^{-1}]^{1/n'}} \tag{2.10}$$

By taking full advantage of the Manson-Coffin-Basquin equation and the Ramberg-Osgood relationship, fatigue life models for parameters proposed by Neuber [31], Molski and Glinka [32], and Lagoda and Macha [30] can be stated as follows, respectively,

$$W_{aN} = \frac{(\sigma_f')^2}{2E}(2N_f)^{2b} + \frac{1}{2}\sigma_f'\varepsilon_f'(2N_f)^{b+c} \tag{2.11}$$

$$W_{aMG} = \frac{(\sigma_f')^2}{2E}(2N_f)^{2b} + \frac{1}{1+n'}\sigma_f'\varepsilon_f'(2N_f)^{b+c} \tag{2.12}$$

$$W_{aLM} = \frac{P_a}{\omega} = \frac{(\sigma_f')^2}{2E}(2N_f)^{2b} + \frac{1-n'}{1+n'}\sigma_f'\varepsilon_f'(2N_f)^{b+c} \tag{2.13}$$

The models were applied to notched specimens made of 10HNAP steel subjected to pure bending, pure torsion, combined bending and torsion load conditions The results were compared with experimental results obtained by the authors [30].

Considering the fatigue parameters determined for smooth specimens under pure tension-compression loading, Lagoda and Macha [30], to reflect the effect of stress gradient, used the following relationship between the damage (D_f) and the lifetime (N_f) of smooth and notched parts,

$$\frac{D_f}{D_f'} = \frac{N_f'}{N_f} = \frac{S_0}{S_f} \tag{2.14}$$

where prime ($'$) represents the values of notched specimen, S_0 is the area of the nominal cross section of the specimen and, S_f is the area of the active part of this section. Accordingly, they figured the fatigue life of the notched parts by multiplying the N_f values corresponding to each model with the ratio of S_0/S_f. The results showed that, their power parameter model, together with the Molski and Glinka's equivalent strain energy density model, worked well for notched structures under random loading. On the other hand, the model developed by Lagoda and Macha requires parameters that relate the smooth specimen to the notched one in order to be applied to the notched parts. This limits its applicability considerably.

At the beginning of the 21st century, Papadopoulos [5] presented a stress based critical plane type life prediction model. The applicability of the model was limited to high-cycle fatigue under proportional and non-proportional multiaxial loads with constant amplitude. While doing this, Papadopoulos made use of the generalized shear stress amplitude, a quantity previously introduced by him [33] and denoted as T_a, as a criterion in determining the critical plane. The plane on which T_a attains its peak value was considered the critical plane. The fatigue limit criterion propounded by Papadopoulos [5] can be written as

$$maxT_a + \alpha_\infty \sigma_{H,max} \leq \gamma_\infty \tag{2.15}$$

where $\sigma_{H,max}$ is the maximum value of hydrostatic stress, $max[\sigma_{kk}(t)/3]$. It can also be written as sum of the mean stress and the stress amplitude, $\sigma_{H,amp} + \sigma_{H,mean}$, in the critical plane. The material parameters α_∞, γ_∞ and the generalized shear stress amplitude, T_a, are also given in the following form,

$$\alpha_\infty = \frac{3(s_{-1} - s_0)}{2(2s_0 - s_{-1})} \tag{2.16}$$

$$\gamma_\infty = \frac{s_0 s_{-1}}{2(2s_0 - s_{-1})} \tag{2.17}$$

$$T_a(\varphi, \theta) = \sqrt{\frac{1}{\pi}\int_0^{2\pi} \tau_a^2(\varphi, \theta, \chi) d\chi} \tag{2.18}$$

where s_0 and s_{-1} are the fatigue limit in zero-to-tension and the fatigue limit in fully reversed tension-compression, respectively and φ, θ, and χ are the angles related to the critical plane.

Finally, corresponding fatigue life criterion was formulated by Papadopoulos as

$$\frac{maxT_a + 3(t_{-1}/f_{-1} - 1/2)\sigma_{H,a}}{1 - \frac{3}{t_{-1}}(t_{-1}/f_{-1} - 1/2)\sigma_{H,m}} = \kappa N^{-\lambda} + t_{-1} \tag{2.19}$$

As seen in the equation, the model uses four material parameters (t_{-1}, f_{-1}, κ and λ). Here, t_{-1} is the fatigue limit under fully reversed torsion and f_{-1} is the fatigue limit under fully reversed bending. The parameters κ and λ are determined through S-N curves. The excessive number of parameters that need to be determined empirically makes the use of the Papadopoulos model complicated.

Bearing in mind that variation in principal stress directions has an impact on the fatigue behavior, Carpinteri and Spagnoli [34] attempted to formulate a new fatigue failure criterion for hard metals (brittle) by correlating the principal axes with the critical plane. To eliminate the problem of variation in the principal stress directions, they considered averaged principal

stress directions derived through suitable weight functions and suggested the following criterion, known as the Carpinteri-Spagnoli (C-S) criterion in the literature,

$$\sigma_{eq} = \sqrt{\sigma_m^2 + \left(\frac{\sigma_{af}}{\tau_{af}}\right)^2 \tau_a^2} \tag{2.20}$$

Their criterion to define the equivalent stress, σ_{eq}, consists of the maximum normal stress, σ_m, and the shear stress amplitude, τ_a, prevailing on the critical plane. Since no effect of it on fatigue strength of hard metals is observed, mean shear stress is not taken into account. Also, the expression σ_{af} in the formula represents the normal stress fatigue limit for bending and, τ_{af} symbolizes the shear stress fatigue limit for torsion. Both are calculated under fully reversed load circumstances.

By nature of the stress-based models, Carpinteri-Spagnoli criterion can be applied only in long-life fatigue regimes. On the other hand, model adequately accounts for the non-proportionality and mean stress effects.

Additionally, Carpinteri et al. [35] advanced the above study and developed a strain-based version of the Carpinteri-Spagnoli criterion to predict the fatigue life of plain metallic parts. In this revised version, normal and shear strain amplitudes on the critical plane were included, instead of stress components. An equivalent strain amplitude, $\varepsilon_{a,eq}$, as a function of normal and shear strains was formed to be damage parameter as

$$\varepsilon_{a,eq} = \sqrt{\left(\varepsilon_{w,a}\right)^2 + 3\left(\gamma_{uw,a}\right)^2} \tag{2.21}$$

where $\varepsilon_{w,a}$ and $\gamma_{uw,a}$ are the normal strain amplitude and the shear strain amplitude related to the critical plane.

Combining the equivalent strain amplitude parameter with Manson-Coffin equation, the researchers generated a new fatigue life model valid for constant amplitude multiaxial loading in the low/medium cycle regime, as the other strain-based models,

$$\sqrt{\left(\varepsilon_{w,a}\right)^2 + 3\left(\gamma_{uw,a}\right)^2} = \frac{\sigma_f'}{E}\left(2N_f\right)^b + \varepsilon_f'\left(2N_f\right)^c \tag{2.22}$$

No extra experimental procedure was carried out by authors. They examined the validity of their model by analyzing the strain controlled experimental data of plain hollow cylindrical specimens made of Inconel 718 and 1045 Steel reported by Socie et al. [36] and, Fatemi and Stephens [37].

Susmel and Lazzarin [38] assumed that the critical plane coincides with the plane where the maximum shear stress amplitude, τ_a, develops. To identify the maximum shear stress amplitude, they benefited from the Papadopoulos's [39] minimum circumscribed circle concept [MCC]. A stress ratio parameter including the maximum shear stress amplitude and the maximum normal stress, $\sigma_{n,max}$, affecting the critical plane was defined as follows,

$$\rho = \frac{\sigma_{n,max}}{\tau_a}(\emptyset^*, \theta^*) \tag{2.23}$$

where $\emptyset^*$and $\theta^*$are the angles that define the initiation plane.

Considering a modified Wöhler diagram which plots, in logarithmic scale, the relationship between the shear stress amplitude and the number of cycles to failure, the authors [38] presented a model for estimating the fatigue life of the components under multiaxial loading conditions,

$$N_f = \left[\frac{\tau_{A,Ref}(\rho)}{\tau_a(\emptyset^*, \theta^*)}\right]^{k_\tau(\rho)} \cdot N_{Ref} \tag{2.24}$$

where N_{Ref} is the reference number of cycles, $\tau_{A,Ref}(\rho)$ is the fatigue strength corresponding to such reference and, $k_\tau\ (\rho)$ is the negative inverse slope of Wöhler curve. The degree of accuracy of the model highly depends on the number of experimental data (i.e. number of curves) used to determine the reference fatigue strength and the inverse slope of curves, which are a function of the stress ratio parameter, ρ.

Later on, Lazzarin and Susmel [38,40] calibrated their model for high-cycle fatigue by using a linear combination of experimental data from uniaxial fully reversed constant amplitude tension (ρ =1) and torsion (ρ =0) tests,

$$\tau_{A,Ref(\rho)} = \left[\tau_{A,Ref(\rho=1)} - \tau_{A,Ref(\rho=0)}\right] \times \rho + \tau_{A,Ref(\rho=0)} \tag{2.25}$$

$$k_{\tau(\rho)} = \left[k_{\tau(\rho=1)} - k_{\tau(\rho=0)}\right] \times \rho + k_{\tau(\rho=0)} \tag{2.26}$$

The model succesfully accounts for mean stress effect and non-proportionality. Thanks to the fact that Wöhler curves can be revised using the fatigue strength reduction factor, K_f, this model can also be applied to notched structures. On the other hand, when the value of the stress ratio parameter exceeds 1.0, the applicability of the model becomes questionable.

In parallel with that study, Susmel and Taylor [1] employed the modified Wöhler curve method (MWCM) in conjunction with the point method (PM) and devised a new multiaxial fatigue life estimation model for notched components. The model was set forth to be valid for medium cycle regime ($10^4 - 10^6$ cycles).

Since El Haddad parameter serves the purpose only in high-cycle fatigue, Susmel and Taylor [1] defined a new critical distance-fatigue life relation for medium-cycle regime,

$$L_M = AN_f^B \tag{2.27}$$

Material constants A and B are calculated through two calibration curves plotted for fully reversed loading.

With a difference from the Susmel and Lazzarin's stress ratio parameter [38], Susmel and Taylor [1] used an effective stress ratio parameter, ρ_{eff}, here,

$$\rho_{eff} = \frac{m\sigma_{n,m} + \sigma_{n,a}}{\tau_a} \tag{2.28}$$

where m is the mean stress sensitivity index. The authors [1] stated that, once the stress distribution along the focus path is calculated analytically or numerically, modified Wöhler curve related to any material point located on that path at any distance, r, from the crack initiation point can be sketched and thus, the number of cycles to failure, $N_{f,e}$, can be predicted at such point by employing the following relationship,

$$\frac{L_M}{2} - r = 0 \;\; \rightarrow \frac{AN_{f,e}^{B}}{2} - r = 0 \tag{2.29}$$

By 2012, Walat et al. [41] revealed four different models by defining different damage parameters as well as different critical plane selections. These models were actually generalized forms for low-cycle states of the patterns previously produced by the authors for high-cycle regime. Thus, they were capable of accounting for both low-cycle and high-cycle conditions. A pair of strain criterion were proposed:

(i) A damage parameter composed of the maximum normal ($\varepsilon_{a\eta}$) and shear ($\varepsilon_{a\eta s}$) strains on the plane of maximum normal strain, in conjunction with the Manson-Coffin-Basquin relationship, was defined as follows,

$$b\varepsilon_{a\eta s} + \varepsilon_{a\eta} = \frac{\sigma_f'}{E}\left(2N_f\right)^b + \varepsilon_f'\left(2N_f\right)^c \tag{2.30}$$

where b is a material constant to be obtained through the experimental procedure.

(ii) Another strain criterion was put forward considering the critical plane being the same as the plane of maximum shear strain,

$$2\frac{\varepsilon_{axx}}{\gamma_{axy}}\varepsilon_{a\eta s} + \frac{2}{1-v_{eff}}\left[1 - \frac{\varepsilon_{axx}}{\gamma_{axy}}\left(1+v_{eff}\right)\right]\varepsilon_{a\eta} = \frac{\sigma_f'}{E}\left(2N_f\right)^b + \varepsilon_f'\left(2N_f\right)^c \tag{2.31}$$

where v_{eff} is efficient Poisson's ratio [42,43].

One couple of generalized energy criteria accompanied the strain criteria:

(i) A fatigue life model consisting of the amplitude of both stress ($\sigma_{a\eta}, \tau_{a\eta s}$) and strain ($\varepsilon_{a\eta}, \varepsilon_{a\eta s}$) components acting on the plane of maximum normal strain energy density was introduced as

$$\frac{\beta}{2}\tau_{a\eta s}\varepsilon_{a\eta s}sgn\left[\tau_{a\eta s}, \varepsilon_{a\eta s}\right] + \frac{1}{2}\sigma_{a\eta}\varepsilon_{a\eta}sgn\left[\sigma_{a\eta}, \varepsilon_{a\eta}\right] = \frac{\left(\sigma_f'\right)^2}{2E}\left(2N_f\right)^{2b} + \frac{1}{2}\sigma_f'\varepsilon_f'\left(2N_f\right)^{b+c} \tag{2.32}$$

where β is a material constant determined from uniaxial data.

(ii) Lastly, the energy criterion based on the plane of maximum shear strain energy density was proposed in the form below,

$$W_{aeq} = 2\frac{\sigma_{axx}\varepsilon_{axx}}{\tau_{axy}\gamma_{axy}}\frac{\left(1+v_{eff}\right)}{8}\sigma_{axx}\varepsilon_{axx} + \frac{4}{1-v_{eff}}\left[1-\frac{\sigma_{axx}\varepsilon_{axx}}{2\tau_{axy}\gamma_{axy}}\right]\frac{\left(1-v_{eff}\right)}{8}\sigma_{axx}\varepsilon_{axx} \tag{2.33}$$

and

$$W_{aeq} = \frac{\left(\sigma_f'\right)^2}{2E}\left(2N_f\right)^{2b} + \frac{1}{2}\sigma_f'\varepsilon_f'\left(2N_f\right)^{b+c} \tag{2.34}$$

As a final remark, the authors tested their criterion's reliability via extensive experimental data from literature and pointed out that while the criterion on the plane of maximum normal strain and maximum shear strain energy density are highly promising, other models remained incapable to meet some conditions, such as non-proportional hardening for some materials.

Ince and Glinka [44] presented two novel damage parameters. They considered the plane experiencing the maximum amount of damage, rather than the extreme stress-strain planes, as the critical plane. Their so-called generalized strain energy (GSE) damage

parameter can be expressed in terms of normal and shear stresses and strains on such plane as follows,

$$W_{gen}^{*} = \left(\tau_{max} \frac{\Delta\gamma^{e}}{2} + \frac{\Delta\tau}{2} \frac{\Delta\gamma^{p}}{2} + \sigma_{n,max} \frac{\Delta\varepsilon_{n}^{e}}{2} + \frac{\Delta\sigma_{n}}{2} \frac{\Delta\varepsilon_{n}^{p}}{2} \right)_{max} = f(N_f) \qquad (2.35)$$

The superscripts e and p symbolise elastic and plastic quantities, respectively. The GSE parameter pretty well accounts for the hardening due to non-proportional loading and the non-zero mean stress effect through the elastic and plastic energy terms for plain specimens. On the other hand, when the model is applied to notched samples, its prediction performance decreases. Moreover, by normalizing the shear strain energy terms (first two terms) with the shear stress amplitude, $\frac{\Delta\tau}{2}$, and the normal strain energy terms (3rd and 4th terms) with the normal stress amplitude, $\frac{\Delta\sigma_n}{2}$, Ince and Glinka derived a new parameter named as generalized strain amplitude (GSA) parameter from generalized strain energy parameter. A deficiency about this parameter is that while GSA parameter gives good results under uniaxial stresses, it cannot show the same performance in multi-axial loading conditions.

Their generalized strain amplitude parameter can be written as

$$\frac{\Delta\varepsilon_{gen}^{*}}{2} = \left(\frac{\tau_{max}}{\tau_{f}'} \frac{\Delta\gamma^{e}}{2} + \frac{\Delta\gamma^{p}}{2} + \frac{\sigma_{n,max}}{\sigma_{f}'} \frac{\Delta\varepsilon_{n}^{e}}{2} + \frac{\Delta\varepsilon_{n}^{p}}{2} \right)_{max} = f(N_f) \qquad (2.36)$$

Susmel et al. [45,46] published two different studies introducing their so-called modified Manson-Coffin curve method (MMCCM), which predicts the fatigue life of metallic materials. In fact, this approach was nothing but a new version adapted to strains of the modified Wöhler curve method (MWCM) [38,40], which is known to be a stress-based approach.

Sensitive to phase angle changes and mean stress effect, the MMCCM model was formulated as follows,

$$\gamma_a = \frac{\tau'_f(\rho)}{G}\left(2N_f\right)^{b(\rho)} + \gamma'_f(\rho)\cdot\left(2N_f\right)^{c(\rho)} \tag{2.37}$$

Here, $\tau'_f(\rho), \gamma'_f(\rho), b(\rho)\ and\ c(\rho)$ are material functions depending on the stress ratio, ρ (recall: $\rho = \sigma_{n,max}/\tau_a$), in the plane of maximum shear strain amplitude, γ_a(max). By performing appropriate experiments, such functions can be calibrated. The authors [45,46] used the fully reversed torsional and uniaxial plain curves for calibration and obtained the following explicit forms,

$$\frac{\tau'_f(\rho)}{G} = \rho\cdot(1+v_e)\frac{\sigma'_f}{E} + (1-\rho)\frac{\tau'_f}{G} \tag{2.38}$$

$$\gamma'_f(\rho) = \rho\cdot\left(1+v_p\right)\varepsilon'_f + (1-\rho)\gamma'_f \tag{2.39}$$

$$c(\rho) = \frac{c\cdot c_0}{(c_0-c)\rho + c} \tag{2.40}$$

$$b(\rho) = \frac{b\cdot b_0}{(b_0-b)\rho + b} \tag{2.41}$$

where v_e is elastic Poisson's ratio.

Modified Manson-Coffin curve model can be applicable in both plain and notched specimens. On the other hand, correct determination of the stress/strain states at the component's hot spot is a highly tricky issue [46].

Liu et al. [47] provided a stress-fatigue life relation for components with stress raisers. In order to obtain the effective stress at notch root, they adopted the volume method (VM). The plane of maximum shear stress range was considered crack initiation plane i.e. critical plane. A hemisphere volume with radius of 1.54L centred the maximum stress point was appointed as process zone. After the stress gradient at each material point within the fatigue process zone was converted into the critical plane's stress components, τ and σ_n, maximum effective stresses were acquired by averaging those of values over the control volume, V, as follows,

$$\tau_{FI} = \frac{1}{V}\int f(\tau)\, dv \tag{2.42}$$

$$\sigma_{n,FI} = \frac{1}{V}\int f(\sigma_n)\, dv \tag{2.43}$$

where τ_{FI} and $\sigma_{n,FI}$ are the effective shear stress and the effective normal stress, respectively.

Finally, a damage parameter model for notched elements was proposed by Liu and co-workers [47] on the basis of the effective stresses,

$$\sqrt{3\left(\tau_{\max,FI}/2\right)^2 + k\left(\sigma_{n,\max,FI}\right)^2} = \sigma_f'\left(2N_f\right)^b \tag{2.44}$$

Apart from volume concept, this model can easily be applied to plain specimens by employing the maximum shear stress amplitude, $\Delta\tau_{max}$, instead of the effective shear stress and the maximum normal stress, $\sigma_{n,max}$, instead of the effective normal stress in such a plane,

$$\sqrt{3(\Delta\tau_{max}/2)^2 + k\left(\sigma_{n,max}\right)^2} = \sigma_f'\left(2N_f\right)^b \tag{2.45}$$

Carpinteri et al. [48] correlated the critical plane with averaged principal directions through an off-angle, just as it was done in reference [34]. Linking the averaged principal directions to the critical plane, this angle was defined as follows,

$$\delta = \frac{3}{2}\left[1 - \left(\frac{\tau_{af,-1}}{\sigma_{af,-1}}\right)^2\right] 45^\circ \tag{2.46}$$

where $\sigma_{af,-1}$ and $\tau_{af,-1}$ are fully reversed normal and shear stress fatigue limits, respectively. An equivalent normal stress was expressed by a linear combination of stress components acting on the critical plane,

$$\sigma_{eq,a} = B\tau_{\eta s,a} + K\sigma_{\eta,a} \tag{2.47}$$

The weighing factors, B and K, are evaluated in terms of the fatigue limits, $\sigma_{af,-1}$ and $\tau_{af,-1}$, and the angle between the critical plane and the fatigue fracture plane, β, considering the uniaxial pure tension and pure torsion conditions as

$$B = \frac{\frac{\sigma_{af,-1}}{\tau_{af,-1}} - \frac{\sin(90° + 2\beta)}{\cos^2\beta}}{\frac{\sin(2\beta)\sin(90° + 2\beta)}{2\cos^2\beta} + \cos(90° + 2\beta)} \tag{2.48}$$

$$K = 2 - \frac{\sigma_{af,-1}}{\tau_{af,-1}} \tag{2.49}$$

As the last step, Carpinteri et al. [48] followed a method based on the regression equation recommended by American Society for Testing and Materials (ASTM) [49] in determining fatigue life,

$$N_{cal} = 10^{A_\sigma + m_\sigma \log(\sigma_{eq,a})} \tag{2.50}$$

where A_σ and m_σ are the regression equation coefficients to be determined under fully reversed bending.

Another comprehensive study for fatigue assessment of notched samples was conducted by Branco et al. [4,50]. Assuming that both the plain and the notched components fail when the total strain energy density at the crack initiation sites achieves a threshold value, Branco and his associates created a new fatigue assessment model for lateral U-shaped notched round bars under constant amplitude, proportional bending and torsion. The method was based upon the assumption that a notched part is exposed to the same damage as the plain one, if the crack initiation sites experience the identical stress-strain states. Thus, the stress concentration phenomena could be explained via smooth samples. By performing fully reversed strain controlled tests for plain specimens, a fatigue master curve correlating the total strain energy density, ΔW_T, to the number of cycles to failure was built by the authors as follows,

$$\Delta W_T = \kappa_t \left(2N_f\right)^{\alpha_t} + \Delta W_{0t} \tag{2.51}$$

where κ_t and α_t are two material constants, and ΔW_{0t} is the elastic energy limit for tension. Branco and coworkers [4,50] employed the line method (LM) of the theory of critical distances (TCD) in order to calculate the uniaxial equivalent stress for notched samples. El-Haddad parameter was used to define the critical distance.

Afterwards, Branco et al. [51] improved the aforementioned study and used Ellyin's method [52] in order to directly compute the total strain energy density. According to Ellyin's model, the total strain energy density at the crack initiation site can be expressed in terms of elastic strain energy density, ΔW_e^+, and plastic strain energy density, ΔW_p, by the following equation,

$$\Delta W_T = \Delta W_e^+ + \zeta \Delta W_p \tag{2.52}$$

where ζ is multiaxial coefficient. ΔW_e^+ and ΔW_p are defined by the following formulas,

$$\Delta W_e^+ = \frac{1+v}{3E}\left(\sigma_{eq}^{max}\right)^2 + \frac{1-2v}{6E}\left[\sum_{i=1}^{3}\left(\sigma_i^a + \sigma_i^m\right)\right]^2 \tag{2.53}$$

$$\Delta W_p = \frac{2(1-n')}{1+n'}\left(2K'\right)^{-1/n'} \cdot \left(\Delta\sigma_{eq}\right)^{(1+n')/n'} \tag{2.54}$$

where K' is the coefficient of cyclic hardening and n' is the cyclic hardening exponent. After evaluating the total strain energy density around the fatigue process zone, an effective strain energy density parameter can be calculated by using the line method.

Not long ago, Liao and Zhu [53] designed a new energy based-fatigue model for the specimens with geometric discontinuities. As a starting point, they took the idea that not only the grains along the crack path, but also the ones surrounding them are determining factors in the fatigue assessment procedure. Stress field intensity (SFI) approach developed by Yao [54] about a quarter-century before this study was a guide for the researchers.

Considering the stress state within a local fatigue failure region, Ω, Yao defined the stress field intensity damage parameter as

$$\sigma_{FI} = \frac{1}{V}\int f(\sigma_{ij})\,\varphi(\vec{\boldsymbol{r}})dv \quad in\ \Omega \tag{2.55}$$

where $f(\sigma_{ij})$ is function of the equivalent stress and $\varphi(\vec{\boldsymbol{r}})$ is the weight function. Yao [54] determined the weight function as a linear combination of the distance from any material point in local damage region to the critical point, r, the direction angle between such points, θ, and, the relative stress gradient, c_*, as follows,

$$\varphi(\vec{\boldsymbol{r}}) = 1 - c_* r(1+\sin\theta) \ \rightarrow\ \left(c_* = \left|\frac{1}{\sigma_{max}}\cdot\frac{d\sigma}{dr}\right|\right) \tag{2.56}$$

Assuming both the smooth and the notched specimens have the same fatigue lives as long as their history of the stress field intensity within the local damage region is identical, after determining σ_{FI}, fatigue life of a notched component can be evaluated through the S-N diagram. On the other hand, determining the stress field intensity and the radius of the fatigue failure region is laborious and time consuming [53].

Referring to the Yao's stress field intensity parameter, Liao and Zhu [53] proposed a new damage parameter called energy field intensity, W_{FI},

$$W_{FI} = \frac{1}{V_W}\int f(W_{ij})\,\varphi_W(\vec{\boldsymbol{r}})dv \quad in\ \ \Omega_W \tag{2.57}$$

where $f(W_{ij})$ is a function of energy dissipation. Modifying the Ellyin's total strain energy density model [52], it can be written in the form

$$f(W_{ij}) = \Delta W^{t+} = \Delta \mathrm{W}_a^{t+} + \Delta \mathrm{W}_s^{t+} \tag{2.58}$$

Liao and Zhu [53] related the process zone radius with the modified total strain energy density, ΔW^{t+}. They assumed the radius of the effective damage zone is equal to the

distance from the notch root to the point where value of the maximum modified total strain energy density decreases to its half. Finally, they clarified the last undetermined term in their formula: the weight function, $\varphi_W(\vec{r})$. Substituting the weight function into the criterion, the energy field intensity parameter took its final form as

$$W_{FI} = \frac{1}{V_W}\int \Delta W_i^{t+}\left(1 - \frac{1}{\Delta W_{max}^{t+}}\cdot\frac{\partial(\Delta W_i^{t+})}{\partial r} + r(1+\sin\theta_W)\right)dv \tag{2.59}$$

They employed the following fatigue master curve relation, depending on the material parameters p and q, to evaluate fatigue life of notched samples,

$$W_{FI} = p\left(2N_f\right)^q \tag{2.60}$$

2.2. Fracture Mechanics Criteria

Only a few approaches will be briefly discussed in this section, as it is slightly related to the content of the work being conducted.

Brown and Miller [55] modified the Dugdale Bilby Cottrell Swinden (DBCS) [56,57] model and obtained a plastic zone size expression for biaxial loading as

$$r_p = a\left(sec\left(\pi\Big/\left((\lambda-1)+\sqrt{\left(4\frac{{\sigma_y}^2}{\sigma^2}-3(\lambda-1)^2\right)}\right)\right)-1\right) \tag{2.61}$$

where sec means secant series, a is the crack length, λ is the biaxiality ratio and, σ_y is the yield strength.

As clearly seen in this formula, the plastic zone size approaches infinity as the applied loads approach the yield strength. In order to remove this problem, Brown and Miller, inspiring by the minor revision done by Tomkins [58] on the DBCS model, replaced the yield strength by the ultimate tensile strength. Correlating the crack growth equation they

developed earlier [59] with the pseudo plastic zone size mentioned above, they defined a crack growth rate expression as follows,

$$\frac{da}{dN} = 18\left(\frac{\sigma_u}{E}\right)^2 a \times \frac{1}{2}\left[\pi \Big/ \left((\lambda - 1) + \sqrt{\left(16\frac{{\sigma_u}^2}{\Delta\sigma^2} - 3(\lambda-1)^2\right)}\right)\right]^2 \tag{2.62}$$

In conclusion, by integrating this equation between the initial and the final crack lengths, a_0 and a_f, the authors determined the crack propagation life, N_p, as follows,

$$\left(\frac{1}{2}\gamma_{max}\right)^2 [D^2 + 2D(1-\lambda) + 4(1-\lambda)^2] = \left[\frac{\sigma_u}{E}(1+v)(1-\lambda)^2\right]^2 \tag{2.63}$$

and

$$D = 3\pi\left(\frac{\sigma_u}{E}\right)\sqrt{\frac{N_p}{\ln\left(\frac{a_f}{a_0}\right)}} \tag{2.64}$$

Paris type equation [60], which relates the crack growth rate with the stress intensity factor range, has been largely used in practice. Tanaka [61] was one of them who made the most of the Paris's precious formula. In order to evaluate rate of the mixed mode fatigue crack propagation (combined mode I and mode II loading), Tanaka defined a new effective stress intensity factor range in the following form,

$$\Delta K_{eff} = \left[\Delta {K_I}^4 + 8\Delta {K_{II}}^4\right]^{0.25} \tag{2.65}$$

His model was designed based on the assumption that deformations arisen from the different loading modes are not interactive. Tanaka suggests that his effective stress intensity factor can be improved to account for the combination of three modes [62].

In 1992, Xiangqiao et al. [63] introduced a different effective stress intensity factor range as

$$\Delta K_{eff} = \frac{1}{2}\cos\left(\frac{\theta_0}{2}\right)[\Delta K_I(1+\cos(\theta_0)) - 3\Delta K_{II}\sin(\theta_0)] \tag{2.66}$$

where θ_0 is the angle representing the crack growth path and is determined through the maximum tangential stress criterion. One shortcoming about this model is that it was not verified by experimental data.

Earlier this century, Paris model was reinterpreted by Kujawski [64] with different driving force parameter. Just like Walker did in [65], to eliminate the insensitivity of the Paris criterion to the mean stress effect, Kujawski revised the model and proposed the following expression,

$$\Delta K_K = (\Delta K^+)^{(1-p)} K_{max}^p \tag{2.67}$$

where p is the driving force constant depending on the material and the environmental condition. Following the empirical determination of the Kujawski model constants, fatigue crack growth behaviour of a given material can be correlated for various stress ratio values. On the other hand, this model was established ignoring the compressive effects. Only the tensile part of stress intensity range, ΔK^+, was considered. Therefore, using this model for stress ratios in the range of $0 \leq R \leq 1$ gives more accurate results.

Noroozi et al. [66] suggested that a crack can be considered as a narrow notch. Thus, crack growth behaviour could be explained through the analysis carried out for a notch with the tip radius ρ^*. Assuming the material consists of the identical imaginary square material blocks of which a side length is equal to the notch tip radius, Noroozi et al. correlated the fatigue crack growth rate with the average growth rate over a block as follows,

$$\frac{da}{dN} = \frac{\rho^*}{N} = C\left[(\Delta K_{tot})^{(1-p)} K_{max,tot}^p\right]^\gamma \tag{2.68}$$

The crack growth constant, C, the fatigue crack growth equation exponent, γ, and the model driving force constant, p, were given in terms of the basic material fatigue properties as

$$C = 2\rho^* \left[\frac{\left(\psi_{y,1}\right)^2}{2^{(n'+3)/(n'+1)} \sigma_f' \varepsilon_f' \pi E \rho^*} \right]^{-(1/(b+c))} \tag{2.69}$$

$$\gamma = -\frac{2}{b+c} \tag{2.70}$$

$$p = \frac{n'}{n'+1} \tag{2.71}$$

Here, as a symbol that we are not familiar with, $\psi_{y,1}$ was described by the authors as the averaging constant corresponding to first block. The authors states that, as this model is created by including the residual stress effect into the crack growth driving force, it is applicable to a wide variety of loading conditions as long as the stress ratio is in the range of $-2 < R < 0.7$.

3. AN OVERVIEW OF THEORETICAL BACKROUND AND FORMULATION OF THE PRESENTED MODEL

3.1. Analytical Formulation

In this study, an energy approach is adopted as a practical way to evaluate the crack initiation life of mechanical components with a stress raiser. A new strain energy parameter called equivalent strain energy density is defined as a measure of the material damage in the structures.

The proposed model is applicable in high cycle fatigue regime where the contribution of the plastic deformation to the material damage remains relatively low compared to elastic deformation and, mostly negligible. Considering reversed strain fluctuation between $-\varepsilon_{max}$ and ε_{max} and assuming a linearly elastic stress-strain relation, alternating strain energy density, $U_a(J/m^3)$, is expressed in terms of alternating elastic stress, σ_a, and alternating elastic strain, ε_a, as follows,

$$U_a = \int_0^{\varepsilon_{max}} \sigma d\varepsilon = \int_0^{\varepsilon_{max}} E\varepsilon d\varepsilon = \frac{E\varepsilon_{max}^2}{2} = \frac{E\varepsilon_a^2}{2} = \frac{\sigma_a \varepsilon_a}{2} \tag{3.1}$$

The relationship between the alternating strain, ε_a, and the number of cycles to failure, N_f, can be found using by Coffin-Manson-Basquin equation [67] as

$$\varepsilon_a = \varepsilon_a^e + \varepsilon_a^p = \frac{\sigma_f'}{E}\left(2N_f\right)^b + \varepsilon_f'\left(2N_f\right)^c \tag{3.2}$$

where σ_f' is the axial fatigue strength coefficient, ε_f' is the axial fatigue ductility coefficient, b is the axial fatigue strength exponent, c is the axial fatigue ductility exponent, and E is the elastic modulus. The superscripts e and p represent the elastic and the plastic quantities, respectively. Ignoring effect of the plastic deformation on the fatigue life, the equation is simplified to

$$\varepsilon_a \cong \varepsilon_a^e = \frac{\sigma_f'}{E}\left(2N_f\right)^b \tag{3.3}$$

which is nothing but the strain version of the Basquin's equation [68], indeed. Substituting Equation (3.3), Equation (3.1) becomes

$$U_a = \frac{\left(\sigma_f'\right)^2}{2E}\left(2N_f\right)^{2b} \tag{3.4}$$

This relation, in its presented form, can only be applied to uniform parts under uniaxial loading, not parts containing geometric discontinuities leading to stress concentration. On the other hand, a complex multiaxial stress state develops around a stress raiser, even under uniaxial loading. In the case of multiaxiality, alternating strain energy at a given material point is expressed in terms of alternating stress and strain components, σ_{aij} and ε_{aij}, as

$$U_a = \frac{1}{2}\sum_{i=1}^{3}\sum_{j=1}^{3}\sigma_{aij}\varepsilon_{aij} \tag{3.5}$$

and the corresponding fatigue life can be calculated by

$$U_a = \frac{1}{2}\sum_{i=1}^{3}\sum_{j=1}^{3}\sigma_{aij}\varepsilon_{aij} = \frac{\left(\sigma_f'\right)^2}{2E}\left(2N_f\right)^{2b} \tag{3.6}$$

One may conjecture that cracks in high cycle regime initiate from a micro crack or a micro flaw and the density and size of the microcracks substantially affect the number of cycles to failure. An evaluation based on the local extreme point may be misleading as the micro flaw containing the point where the maximum stress develops may not be the critical one. Such a choice mostly results in overly conservative estimates. On the other hand, considering the highly stressed regions have a much more determining effect on the fatigue life compared to low-stressed regions, it is obvious that a calculation based on just the arithmetic average of the alternating strain energy values around the notch will yield highly non-conservative results. In the light of such information, a region consisting of the points

having alternating strain energy values greater than a threshold value surrounding the stress raiser can be assumed as a control volume to account for the effect of the highly stressed region on the fatigue life.

The threshold alternating strain energy density, U_a^{th}, can be calculated by

$$U_a^{th} = \frac{\left(\sigma_f'\right)^2}{2E}\left(2N_f^{th}\right)^{2b} \tag{3.7}$$

where N_f^{th} is the effective material endurance limit. If the calculated fatigue life at a point around the notch is larger than N_f^{th}, that point is disregarded in fatigue-life assessment of the notch.

Considering only the material points having alternating strain energies greater than U_a^{th}, i.e. the points within the high-energy control volume, averaged alternating strain energy density is obtained as follows,

$$U_{avg} = \frac{1}{V'}\iiint_{V'} U_a dV = \frac{1}{V'}\iiint_{V'} \frac{1}{2}\sum_{i=1}^{3}\sum_{j=1}^{3}\sigma_{aij}\varepsilon_{aij}\, dV \tag{3.8}$$

where V' is the volume of the high-energy region.

Actually, in the control volume, high-stressed regions have much more determining effect than the low-stressed regions. So much so that a 10% increase in stress level may reduce the life to its half. Accordingly, a fatigue-life assessment performed using only the averaged alternating strain energy density (Equation (3.8)) as the equivalent parameter will be far from reflecting the actual value. It should be modified to include the said effect. On the other hand, the number of cycles to failure calculated at a material point is a measure of the contribution of that point to the fatigue life of the structure. Accordingly, alternating strain energy value of each material point within the control volume may be normalized by a well-defined function of its corresponding fatigue life to account for the effects of the highly stressed points on the fatigue life of the part, in direct proportion to their intensities.

In the proposed fatigue assessment model U_a is normalized by N_f^{-4b} and then the equivalent alternating strain energy density is obtained as

$$U_{ea} = \frac{\iiint_{V'} \frac{U_a}{N_f^{-4b}} dV}{\iiint_{V'} \frac{1}{N_f^{-4b}} dV} \tag{3.9}$$

Accordingly, once the stress and strain states are determined, the alternating strain energy for each material point in the control volume is calculated using Equation (3.5). Thus, following the calculation of corresponding fatigue lives at each point by Equation (3.6), equivalent alternating strain energy density can be figured by Equation (3.9).

Finally, the fatigue life of a component is given as

$$U_{ea} = \frac{\left(\sigma_f'\right)^2}{2E}\left(2N_f\right)^{2b} \tag{3.10}$$

3.2. Finite Element Modeling (FEM) Formulation

Since the analytical solution is only available for certain geometries and it is not always possible to analytically determine the stress and strain states in the parts with complex geometry, finite element modeling (FEM) is generally employed to determine the stress/strain distribution in irregularly shaped parts.

After determining the alternating elastic stress, σ_{aij}^k, and the alternating elastic strain, ε_{aij}^k, in element k by finite element analysis, the alternating strain energy density in that element, U_a^k, can be calculated using the following formula,

$$U_a^k = \frac{1}{2}\sum_{i=1}^{3}\sum_{j=1}^{3} \sigma_{aij}^k \varepsilon_{aij}^k \tag{3.11}$$

In parallel with the analytical method, fatigue life corresponding to the element k is obtained by

$$U_a^k = \frac{\left(\sigma_f'\right)^2}{2E}\left(2N_f^k\right)^{2b} \tag{3.12}$$

As a final step, the equivalent alternating strain energy density formulated in Equation (3.9) can be reinterpreted in terms of the discrete parameters of finite element model as

$$U_{ea} = \frac{\sum_{k=1}^{n} V_k U_a^k / \left(N_f^k\right)^{-4b}}{\sum_{k=1}^{n} V_k / \left(N_f^k\right)^{-4b}} \tag{3.13}$$

where V_k is the volume of element k. As noted before, only the elements with a strain energy density value exceeding the threshold energy density are considered.

4. RESULTS AND DISCUSSIONS

4.1. Fatigue-Life Evaluation through the Proposed Model

In order to evaluate the prediction performance of the model mentioned above, a comprehensive study is conducted using a large number of experimental data obtained from the literature. ANSYS Parametric Design Language (APDL) is used to develop a code to determine the stress and strain states and also to implement the presented fatigue analysis methodology for fatigue life estimation.

Assuming all examined materials are linear elastic and isotropic, a linear elastic finite element analysis is performed for each different sample. However, in many engineering applications, the maximum equivalent stress at the notch exceeds the yield strength of the material resulting in local yielding. This affects the accuracy of the calculated stress and strain values to some extent. In such a case, as shown schematically in Figure 4.1, a linear structural analysis over predicts stresses, but under predicts strains. On the other hand, considering strain energy density is equal to the area under stress-strain curve, strain energy density in locally yielded zone is more correctly calculated by a linear analysis compared to stress and strain values. As long as large plastic deformations do not occur, the proposed model can give reasonably accurate estimations.

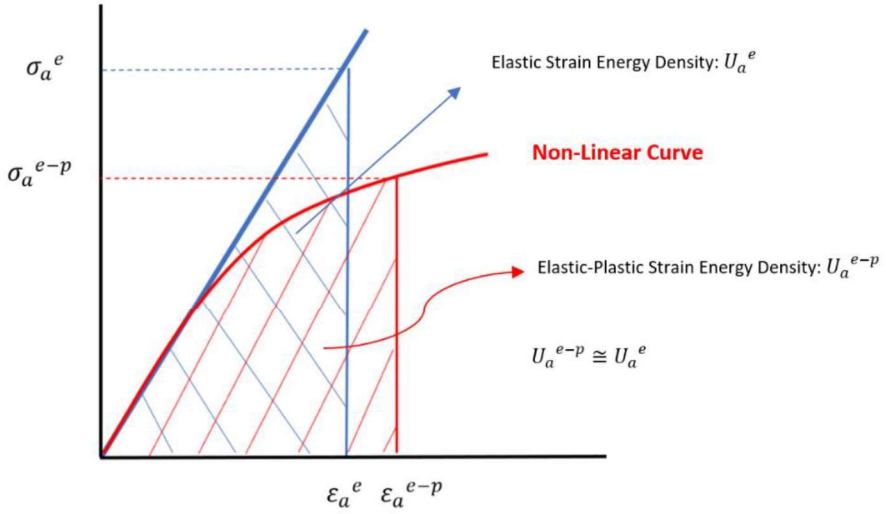

Figure 4.1. A schematic stress-strain diagram for linear and non-linear curves.

Geometries of the samples are modelled in finite element code and then meshed. In order to shorten the analysis time, only a section containing the critical region is considered in some samples, while it is not found necessary such a simplification for most of the parts due to the low number of experimental data.

The presented model can be applied for the parts under constant-amplitude multiaxial loading conditions. In the region where the concentrated forces are applied, locally high stresses develop. On the other hand, according to Saint-Venant principle, as the distance from the application point of a force becomes large, the effects of stress concentration weaken rapidly. Accordingly, at a sufficiently large distance from the loading points, the local effects decay and a smooth stress distribution prevails. Here, considering the Saint-Venant principle, to prevent such a stress concentration developing in the structure, remote loading is resorted. That is to say, an extra part defined with another material and subjected to said forces is appended to the actual body to transmit stresses smoothly. The ways the loads are applied will be depicted and mentioned in detail in the following subsection.

4.2. Comparison of Experimental Results and Model Predictions for Fully Reversed Proportional Loading

4.2.1. Modeling and Results for Al-Si Alloy Grooved Shaft Specimen

The fatigue-life assessment model is first applied to a round bar with a circular groove under combined tension and torsion loading with constant amplitude. The geometry and the dimensions of the specimen are illustrated in Figure 4.2.

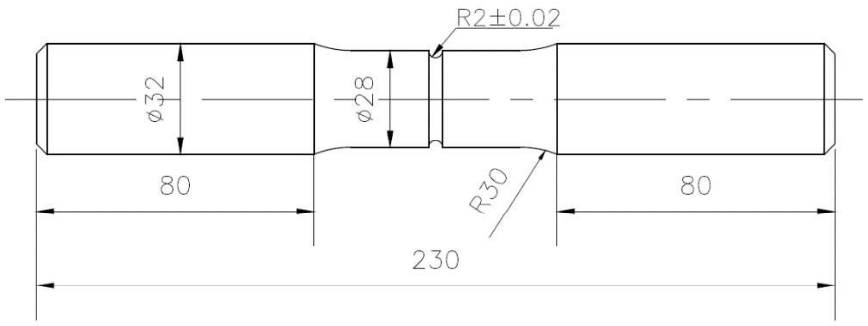

Figure 4.2. A scheme of the grooved round bar. The dimensions are given in millimetres.

The specimen is made of Aluminium-Silicon (Al-Si) alloy. The chemical composition and the material properties of Al-Si alloy reported by Liu et al. [69] are given in Table 4.1 and Table 4.2, respectively.

Table 4.1. Chemical composition of Al-Si Alloy (%) [69].

Si	Cu	Ni	Mg	Fe	Mn	Ti	Zn	Al
12.37	5.28	2.67	0.82	0.42	0.2	0.106	0.006	78.128

Table 4.2. Mechanical properties of the Al-Si alloy at room temperature [69].

Elastic Modulus, E (Pa)	7.80E+10
Poisson's Ratio, v	0.3
Axial Fatigue Strength Coefficient, $\sigma_f{}'$ (Pa)	3.98E+08
Axial Fatigue Strength Exponent, b	-0.0843
Yield Strength, σ_y (Pa)	2.12E+08

Making use of the axisymmetric cross-sectional geometry, analyses are performed in two dimension. PLANE83, which is a two-dimensional 8-node axisymmetric structural solid element, is used as the element type. Convergence analyses are carried out by trying different element sizes and a mesh size is chosen such that increasing the number of elements has insignificant effect on the predicted fatigue life. The model includes 30,739 elements and 93,706 nodes. The finite element model nearby the critical zone is shown in Figure 4.3.

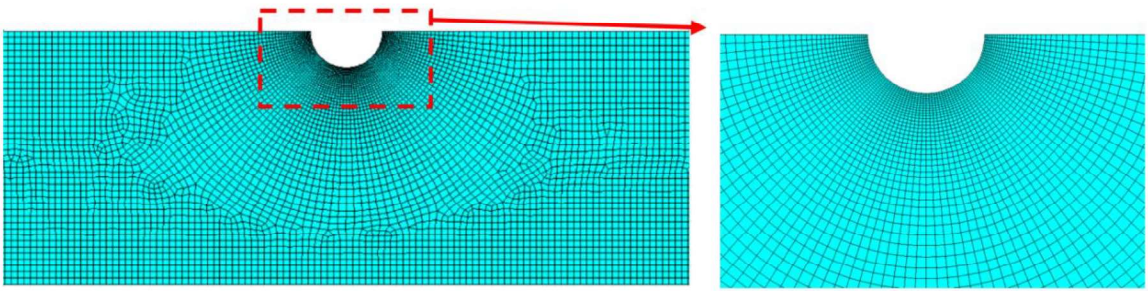

Figure 4.3. The finite element model around the critical region.

In order to prevent stress concentrations due to concentrated forces, a highly stiff section with an elastic modulus much greater than that of the specimen is appended to the structural model, and the loads are applied to that section. A section with the same elastic modulus as the structure is inserted between the stiff section and the main body to ensure a smooth stress transmission. As shown in Figure 4.4, a transverse point force in the z direction is applied to the corner of the stiff section to generate the given torque for each loading condition and a given axial stress in y direction is applied to far edge of that part.

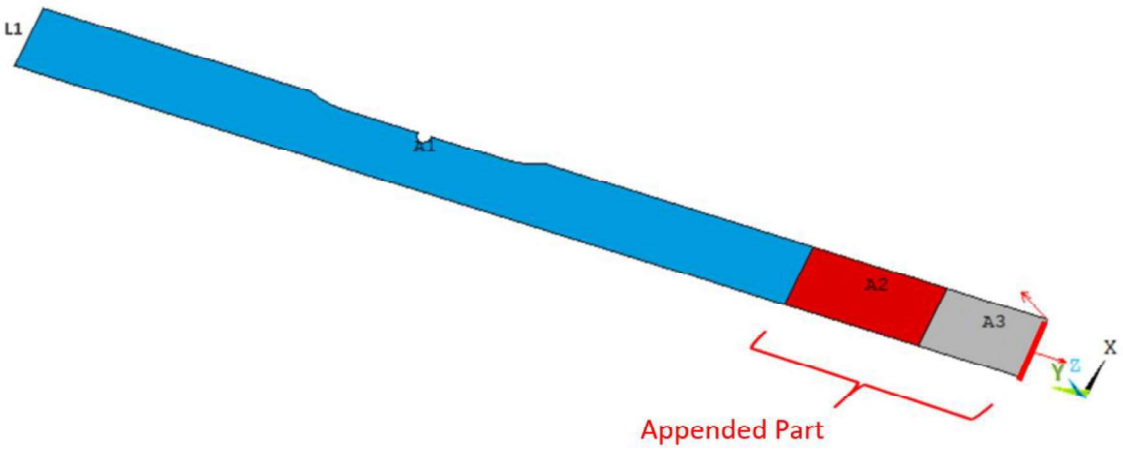

Figure 4.4. Loading pattern of the grooved shaft specimen made of Al-Si alloy.

The axisymmetric round bar is represented by the area A1 in two-dimensional space. y axis of the global coordinate system is defined as the axis of symmetry. In order to apply axisymmetric forces like axial force and non-axisymmetric ones like torque, proper boundary conditions should be imposed on the model. Since different loading types require different boundary conditions in ANSYS, each one is solved separately, and the obtained results are superposed. The movement of the edges on the symmetry axis is restricted in the x and z directions for tensile loading and z direction for torsional loading, while the top side, i.e. edge L1, is not allowed to move in y and z directions for both.

Because the material is assumed to be linear and elastic, only elastic modulus and Poisson's ratio is defined in the material model.

The fatigue-life estimation methodology estimates the fatigue lifetime based on the values of elastic stress and strain components calculated by the linear structural analysis.

The elements belonging to the appended sections are unselected so that only the elements of the main sample are taken into account. Among these, only the ones having a life less than the threshold life, N_f^{th}, are considered. Although aluminium does not have any endurance limit, N_f^{th} is taken as 5×10^6 cycles for both aluminium alloys and steels in this study. If fatigue life of an element is calculated to be above this upper limit value, it is assumed to have no effect on the overall fatigue behaviour of the part.

Experimental fatigue lives of the specimens for crack initiation reported by Liu et al. [69] and the predicted values corresponding to each load combination are presented in Table 4.3 and the correlation between the experimental values and the model estimates can be seen in Figure 4.5.

Table 4.3. Experimental results for Al-Si alloy notched round bar reported in the study [69] and the predictions of the presented model.

Loading Case	Applied Axial Load (N)	Applied Torque (N.m)	Equivalent Nominal Stress (MPa)	Stress Concentration Factor $K_t = \frac{\sigma_{eqv,max}}{\sigma_{eqv,nom}}$	Experimental Crack Initiation Life, $N_{f(exp)}$	Predicted Life, N_f
1	34,461	63	76.2	2.33	38,448	121,946
2	31,180	57	68.9	2.33	190,220	251,418
3	28,741	52.5	63.5	2.33	515,580	441,733

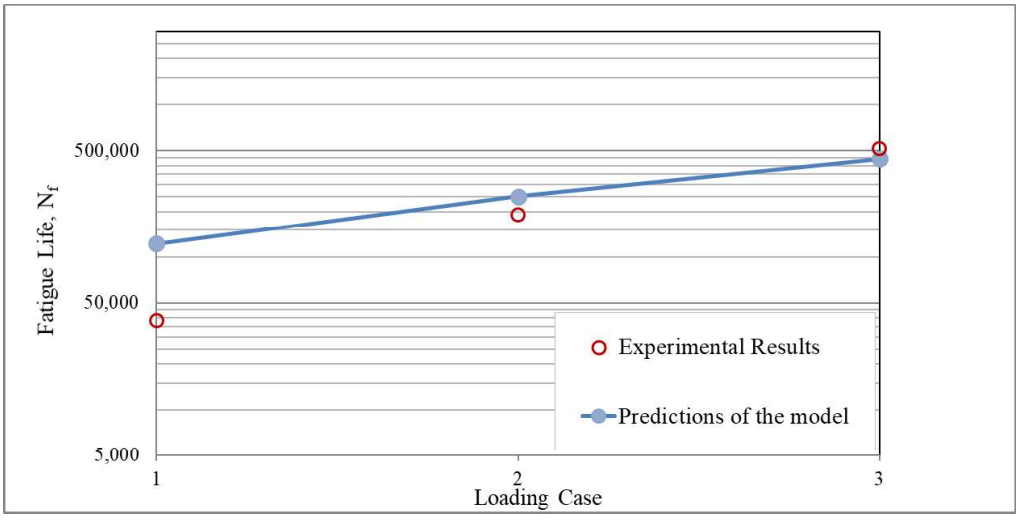

Figure 4.5. Correlation between experimental and theoretical fatigue lives of Al-Si alloy grooved round bar.

An inference based solely on visual inspection of the graph is not sufficient, it should be supported statistically. In order to determine the error range, a fatigue-life scatter analysis is performed in this study using the root mean square logarithmic error method [70]. The value of the root mean square logarithmic error, E_{RMS}, is computed as follows,

$$E_{RMS} = \sqrt{\frac{\sum_{i=1}^{n} log^2 \left(N_{f,exp}/N_{f,pre}\right)_i}{n}} \tag{4.1}$$

where n is the total number of the examined measurements. Accordingly, the mean square error, T_{RMS}, of the scatter can be determined as

$$T_{RMS} = 10^{E_{RMS}} \tag{4.2}$$

The calculated mean square error is 2.00. This means that the average scatter of the model predictions falls on the scatter bands of factor 2.00. Moreover, as seen in Figure 4.6, the ratios of predictions to experimental data are within the acceptable ranges for a fatigue model. Thus, it can be concluded that experimental fatigue lives and numerical estimates are in satisfactory agreement.

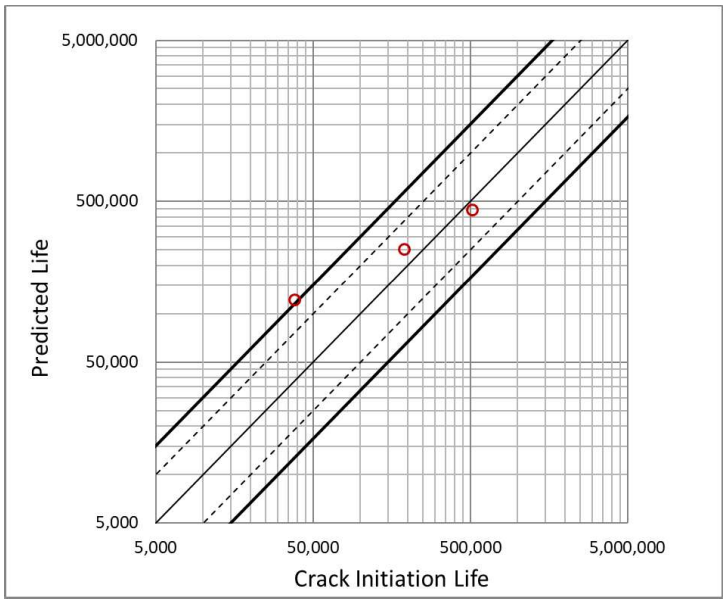

Figure 4.6. Experimental vs. predicted fatigue life for the notched specimen made of Al-Si alloy.

4.2.2. Modeling and Results for AISI 1141 Stepped and Grooved Shaft Specimens

In this section, two different notched geometries made of the same material are examined. Figure 4.7 depicts the shape and dimensions.

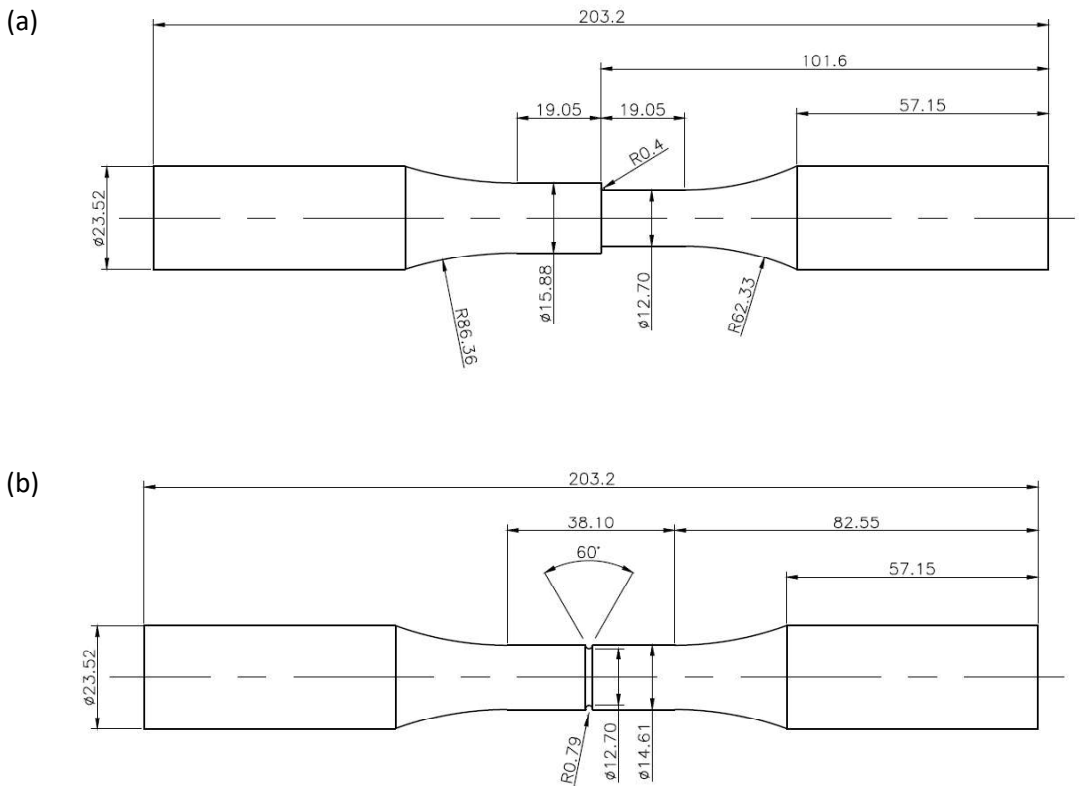

Figure 4.7. Specimen geometries and dimensions for (a) AISI 1141 steel stepped shaft specimen, (b) AISI 1141 steel grooved shaft specimen. All dimensions are given in mm.

The specimens are made of AISI 1141 steel material. Table 4.4 gives the chemical composition of AISI 1141 medium carbon steel presented in reference [71] and the static and fatigue properties of that material reported by Gates and Fatemi [72] are given in Table 4.5.

Table 4.4. Chemical composition of AISI 1141 steel in % (rest Fe) [71].

C	Mg	Si	Cu	Cr	Ni	V
0.39-0.43	1.49-1.66	0.23-0.27	0.14-0.146	0.107-0.12	0.068-0.07	0.053-0.058

Table 4.5. Mechanical properties of the AISI 1141 medium carbon steel [72].

Elastic Modulus, E (Pa)	2.00E+11
Poisson's Ratio, v	0.29
Shear Modulus, G (Pa)	8.02E+10
Axial Fatigue Strength Coefficient, σ_f' (Pa)	1.30E+09
Axial Fatigue Strength Exponent, b	-0.089
Axial Fatigue Ductility Coefficient, ε_f' (Pa)	1.0266
Axial Fatigue Ductility Exponent, c	-0.687
Yield Strength, σ_y (Pa)	5.24E+08
Ultimate Tensile Strength, σ_u (Pa)	8.75E+08

Both the specimens have axisymmetric geometries. An axisymmetric structure can be represented by a two-dimensional finite element model. As in the previous sample, PLANE83 is specified as the element type. This element tolerates geometric irregularities without much loss of accuracy. In this sense, it is ideal for axisymmetric parts experiencing stress concentration. The finite element mesh around the stress raiser is illustrated in Figure 4.8 and Figure 4.9 for the stepped and grooved shafts, respectively.

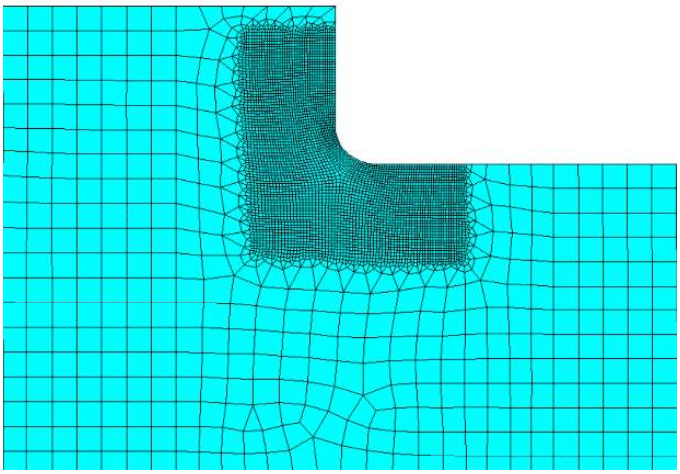

Figure 4.8. The meshed geometry of the AISI 1141 stepped shaft specimen. The finite element model includes 38,098 elements and 116,067 nodes.

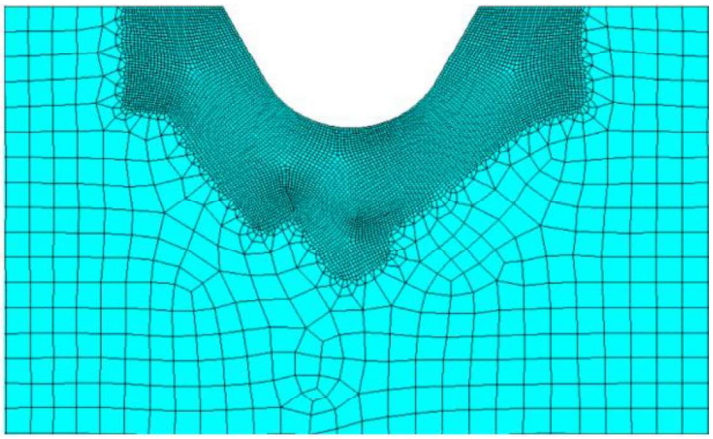

Figure 4.9. The meshed geometry of the AISI 1141 grooved shaft specimen. The finite element model includes 59,215 elements and 179,920 nodes.

The specimens are subjected to fully reversed constant-amplitude proportional tension and torsion. The boundary conditions are applied in the same way as in the previous example (see Figure 4.4).

Material endurance limit of steels ranges between 10^6 and 10^7 cycles. Accordingly, for AISI 1141 and the other steel materials considered in this study, threshold fatigue life, N_f^{th}, is taken as 5×10^6 cycles, which is the same as that of aluminium material. In the presented model, normally all the elements having calculated life less than the threshold value are considered. On the other hand, as the distance from the stress raiser increases, the effect of the elements on the fatigue life calculated in that region rapidly decreases. Accordingly, it will not be a realistic approach to consider high-energy elements far from the critical region in fatigue life evaluation. For this reason, only the sections where the maximum equivalent stress is at least 2% above the nominal equivalent stress are included in fatigue assessment. The reason for not imposing such a limitation in the previous example is that all high energy elements in that specimen are already very close to the notch.

Predictions of the presented algorithm for these parts are compared with the experimental data reported by Gates and Fatemi [72]. Experimental and estimated results for both specimens are listed together in Table 4.6 and the graphical representations are shown separately in Figure 4.10 and Figure 4.11.

Table 4.6. Experimental results for AISI 1141 notched shaft specimens reported in [72] and the estimates of the presented model.

Specimen Geometry	Loading Case	Nominal Tensile Stress (MPa)	Nominal Torsional Stress (MPa)	Equivalent Nominal Stress (MPa)	Stress Concentration Factor $K_t = \frac{\sigma_{eqv,max}}{\sigma_{eqv,nom}}$	Experimental Crack Initiation Life, $N_{f(exp)}$	Predicted Life, N_f
Stepped Shaft	1	0	344	595.8	1.74	1,767	6,916
Stepped Shaft	2	260	274	541.1	1.96	4,865	12,122
Stepped Shaft	3	0	294	509.2	1.74	14,492	31,691
Stepped Shaft	4	201	214	421.7	1.96	49,713	102,432
Stepped Shaft	5	0	240	415.7	1.74	452,785	188,813
Stepped Shaft	6	140	154	301.2	1.95	499,081	418,472
Grooved Shaft	1	0	344	595.8	1.65	1,923	4,631
Grooved Shaft	2	260	274	541.1	1.85	4,732	6,673
Grooved Shaft	3	0	294	509.2	1.65	14,912	12,470
Grooved Shaft	4	201	214	421.7	1.84	44,071	22,057
Grooved Shaft	5	0	240	415.7	1.65	645,000	58,476
Grooved Shaft	6	140	154	301.2	1.83	789,999	209,783

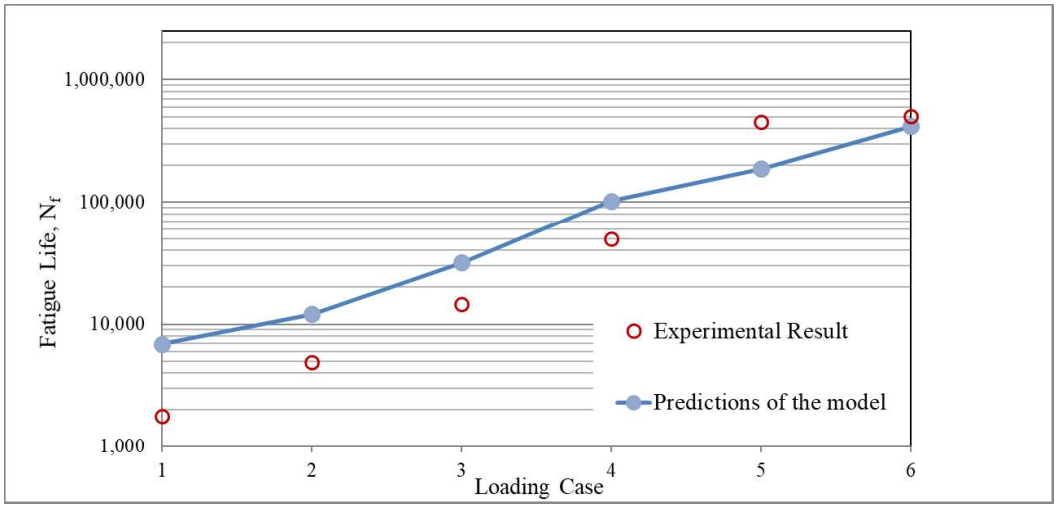

Figure 4.10. Correlation between experimental and theoretical fatigue lives of AISI 1141 stepped shaft specimen.

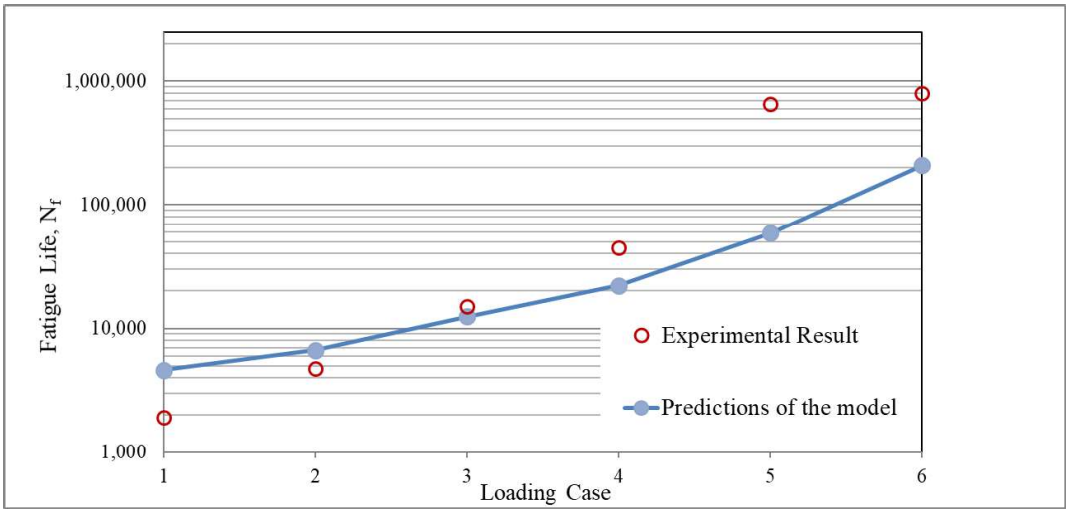

Figure 4.11. Correlation between experimental and theoretical fatigue lives of AISI 1141 grooved shaft specimen.

Thanks to the sufficient number of experimental data, the comparison between experimental and theoretical results can be made numerically by means of correlation analysis. Correlation coefficient is a measure of how strong the relationship between the two sets of values is. Its value ranges from -1 to +1 where +1 indicates the strongest positive agreement, -1 indicates the strongest negative agreement, and 0 means no relationship at all. Pearson's correlation coefficient, R, can be expressed in terms of experimental and theoretical lives as

$$R = \frac{\sum_{i=1}^{n}\left(N_{f,exp}\right)_i\left(N_{f,pre}\right)_i - n\left(\overline{N_{f,exp}}\right)\left(\overline{N_{f,pre}}\right)}{(n-1)s_{\left(N_{f,exp}\right)}s_{\left(N_{f,pre}\right)}} \tag{4.3}$$

where n is the total number of the examined measurements and, $s_{\left(N_{f,exp}\right)}$ and $s_{\left(N_{f,pre}\right)}$ are population standard deviations of experimental and predicted values, respectively. Population standard deviation can be calculated as follows,

$$s_{\left(N_{f,exp}\right)} = \sqrt{\frac{1}{n-1}\sum_{i=1}^{n}\left(\left(N_{f,exp}\right)_i - \left(\overline{N_{f,exp}}\right)\right)^2} \text{ and analogously for } s_{\left(N_{f,pre}\right)} \tag{4.4}$$

The correlation coefficient is calculated as 0.90 for the stepped shaft and 0.87 for the grooved shaft. This means that there is a satisfactory correlation between the experimental data and model estimates.

Moreover, a scatter analysis performed using Equation (4.1) and (4.2) reveals the range of deviations from the experimentally determined values. Accordingly, mean square error of the scatter is figured as 2.40 for the stepped round bar and 3.38 for the grooved one. One can say that the estimations for the grooved shaft show somewhat larger deviation. On the other hand, considering most of the results for that geometry are within the 3x band and all the relatively large deviations remain at the safe side, as seen in Figure 4.12, it can be concluded that the proposed model can be applied for this specimen.

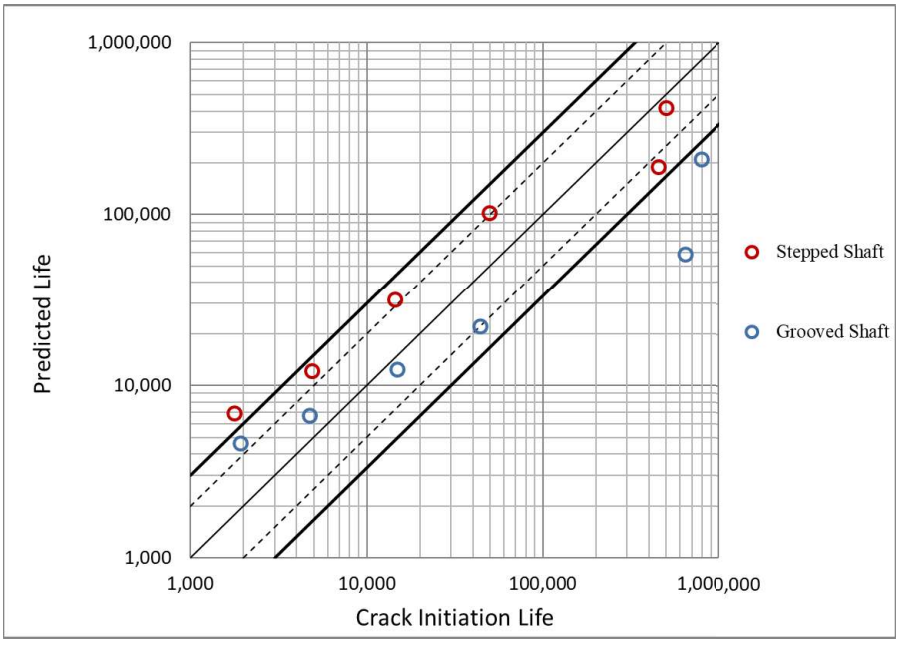

Figure 4.12. Experimental vs. predicted fatigue life for AISI 1141 notched specimens.

4.2.3. Modeling and Results for SAE 1045 Shouldered Shaft Specimen

A more comprehensive study to test the reliability of the model is carried out on SAE 1045 shouldered cylindrical shaft specimen subjected to various fully reversed proportional bending and torsion combinations utilizing the experimental data available in references [73,74]. Geometry and dimensions of the specimen are illustrated in Figure 4.13a.

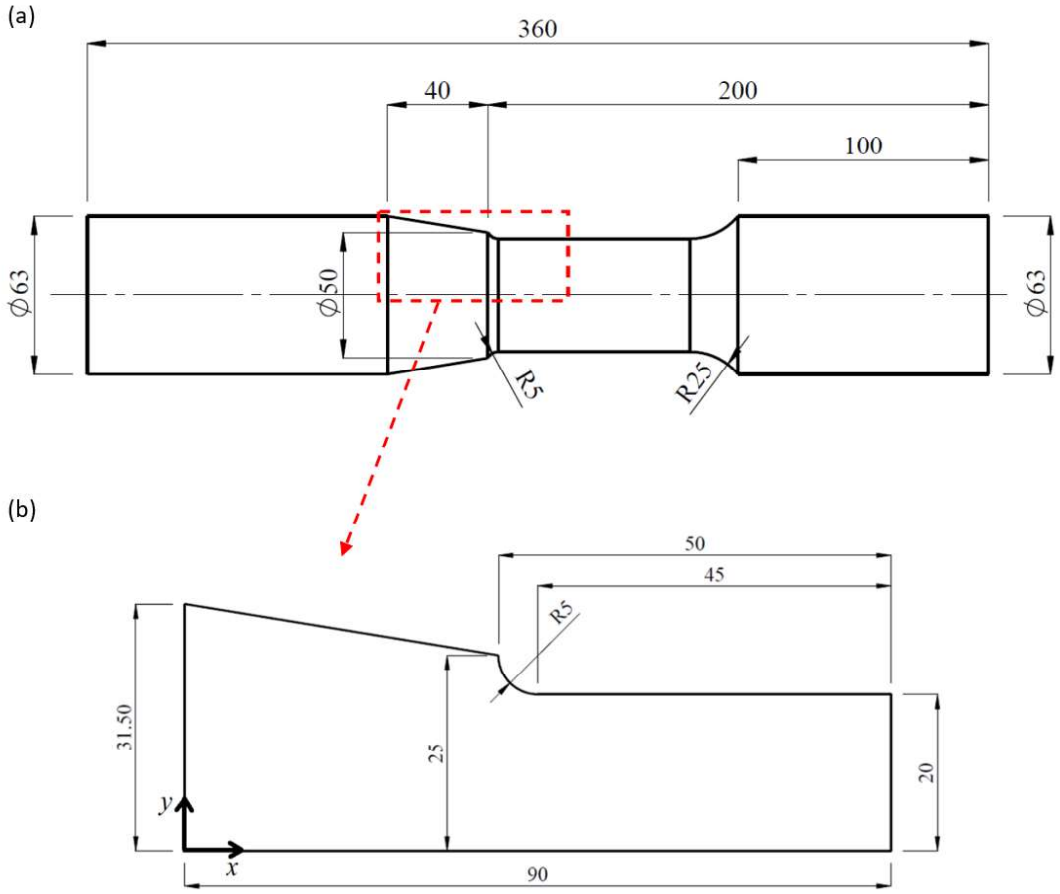

Figure 4.13. Shape and dimensions of SAE 1045 shouldered shaft specimen (a) whole body, (b) analysis domain [7]. The dimensions are in millimetres.

Since there exists a large number of experimental data, a sufficiently large zone covering the entire critical region is employed as the analysis domain to avoid long analysis times. An amplified image of the analysed axisymmetric section can be seen in Figure 4.13b. It is worth noting that such a simplification does not have a significant effect on the results. Even if a larger portion of the specimen is analysed, nearly the same results are obtained.

The specimen is made of SAE 1045 steel, which is a commonly used material in industry. Mechanical properties of SAE 1045 steel reported by Boardman [76], Leese and Morrow [75] and Fash et al. [74] are given in Table 4.7. The differences in values can be thought to arise from differences in steel forming processes and techniques.

Table 4.7. Mechanical properties of SAE 1045 steel.

	Reported by Boardman [76]	Reported by Leese and Morrow [75]	Reported by Fash et al. [74]
Elastic Modulus, E (Pa)	2.16E+11	2.024E+11	2.05E+11
Axial Fatigue Strength Coefficient, σ_f' (Pa)	1.099E+09	9.48E+08	9.80E+08
Axial Fatigue Strength Exponent, b	-0.11	-0.092	-0.11
Yield Strength, σ_y (Pa)	3.53E+08	3.82E+08	3.80E+08

The axisymmetric part to be analysed is meshed with PLANE83 element of which the characteristic features were touched in previous subsections. Additionally, such elements can take non-axisymmetric loads like bending and torsion, as the case in this example. The density of the mesh is gradually increased until no more significant change in the calculated fatigue life occurs i.e. convergence is obtained. The meshed view of the analysis domain is shown in Figure 4.14.

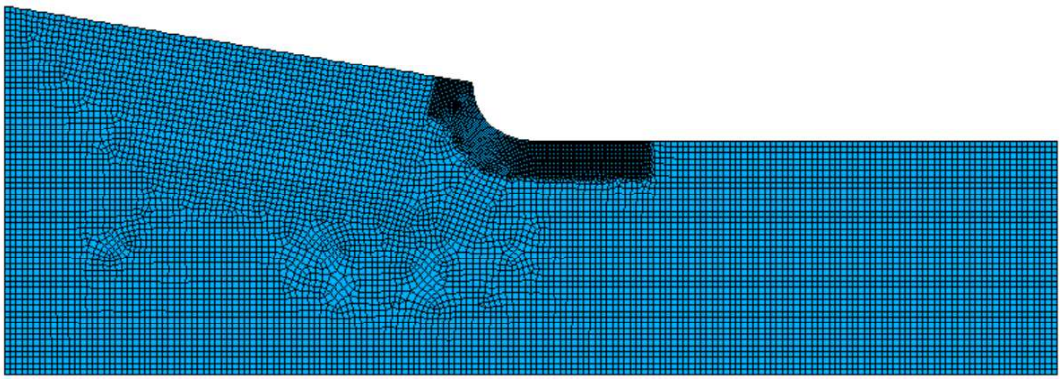

Figure 4.14. The meshed geometry of SAE 1045 shouldered shaft.

The specimen is subjected to fully reversed constant amplitude loads in the form of pure bending, in-phase bending and torsion, and pure torsion. Saint Venant's principle also states that the stress states created by two different but statically equivalent loads at distances far enough from the application points are nearly identical. In accordance with that statement, differently from the preceding examples, here, in order to avoid stress concentration due to point forces, the force in the z direction is distributed to some nodes of an attached part with the same elastic modulus to generate a given torque for each loading

case. Also, bending moment is applied by a pair of transverse forces in x direction with the same magnitude but opposite directions. Loading pattern of the specimen is depicted in Figure 4.15.

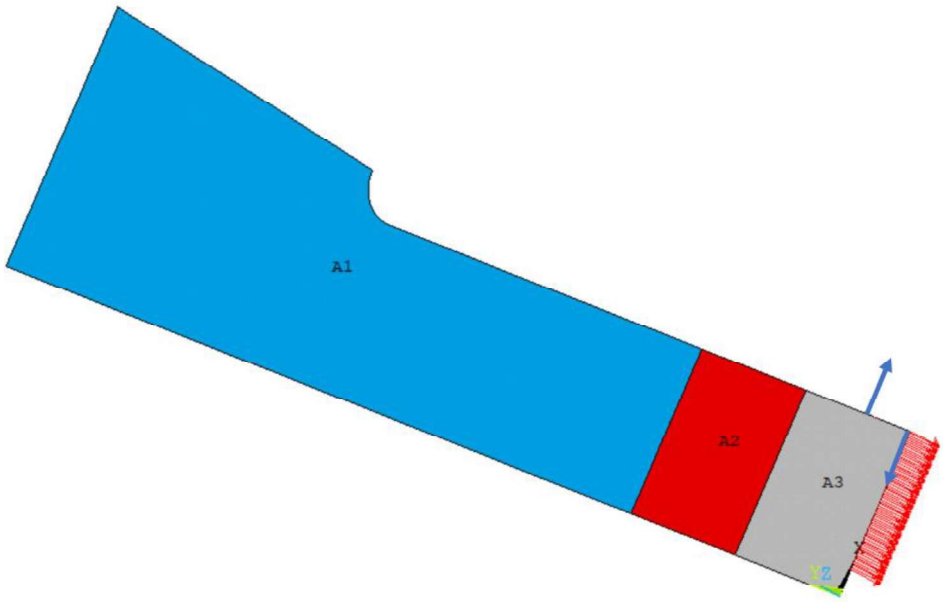

Figure 4.15. Loading pattern of SAE 1045 shouldered shaft specimen.

The elements of the added region are unselected during post-processing, here too. Besides, only the sections where the maximum equivalent stress is at least 2% above the nominal stress are considered in fatigue assessment.

Fatigue life predictions are obtained via the presented fatigue evaluation methodology and compared with the experimental data provided by the studies [73,74]. Experimental results include the number of cycles for the appearance of a 1.0 mm crack emanating from the fillet as well as the ultimate fracture. Since there is a discrepancy between the values reported by different researchers for the mechanical properties of the material, as can be seen in Table 4.7, the analyses are performed separately regarding to the values declared by Boardman [76], Leese and Morrow [75], and Fash et al. [74]. Table 4.8 gives the experimental and estimated fatigue lives corresponding to each load level and a graphical comparison can be found in Figure 4.16.

Table 4.8. Experimental results given by [73,74] and the model predictions obtained using the fatigue properties reported by (a) Boardman [76], (b) Leese and Morrow [75], and (c) Fash et al. [74].

Loading Case	Applied Bending Moment (N.m)	Applied Torsional Moment (N.m)	Experimental Life for Initiation of 1-mm Crack	Final Fracture Life	Predicted Life (a)	Predicted Life (b)	Predicted Life (c)
1	1,850	2,550	2,200	5,113	3,589	3,597	1,415
2	2,800	0	2,571	8,262	2,122	1,768	835
3	1,250	2,700	6,402	10,420	9,127	10,859	3,465
4	1,850	2,100	5,740	11,565	7,679	8,599	2,957
5	1,355	2,550	5,500	11,630	10,373	12,529	3,957
6	2,325	1,350	2,905	11,735	5,175	5,208	2,017
7	2,000	2,100	5,998	12,050	5,211	5,469	1,996
8	0	3,000	5,529	12,124	15,150	19,735	5,749
9	1,150	2,700	3,000	12,700	10,931	13,433	4,154
10	2,600	0	6,347	15,043	3,825	3,440	1,529
11	2,586	0	14,000	17,450	3,988	3,611	1,597
12	851	2,700	9,000	17,730	17,874	23,835	6,810
13	840	2,700	10,000	24,540	18,041	24,095	6,885
14	1,720	1,350	19,260	58,790	35,411	47,191	14,532
15	1,680	960	30,000	65,049	63,538	89,290	27,378
16	1,875	0	48,180	112,200	42,018	53,450	18,829
17	1,220	1,700	60,800	124,500	98,067	156,801	40,546
18	0	2,400	70,350	132,585	92,833	153,960	37,134
19	1,680	900	84,950	153,800	66,667	94,322	28,970
20	780	2,180	70,340	156,100	84,373	137,855	33,776
21	1,730	0	67,300	157,125	73,198	103,281	33,055
22	1,220	1,710	89,750	160,900	95,913	153,370	39,568
23	570	2,180	87,830	182,250	121,551	208,100	49,170
24	1,550	1,090	88,750	190,200	90,129	135,507	38,941
25	1,300	1,400	84,680	226,000	140,480	228,205	60,107
26	1,708	0	163,800	249,900	80,217	114,688	36,205
27	845	1,800	259,900	396,800	221,251	391,872	93,263
28	1,475	0	347,500	556,400	218,760	351,893	100,067
29	1,250	880	462,500	734,750	395,421	654,353	182,807
30	1,460	0	430,000	764,000	234,319	379,206	107,288
31	990	1,390	641,500	890,500	424,017	747,256	191,434
32	0	2,000	1,011,333	1,843,667	361,889	677,790	156,158

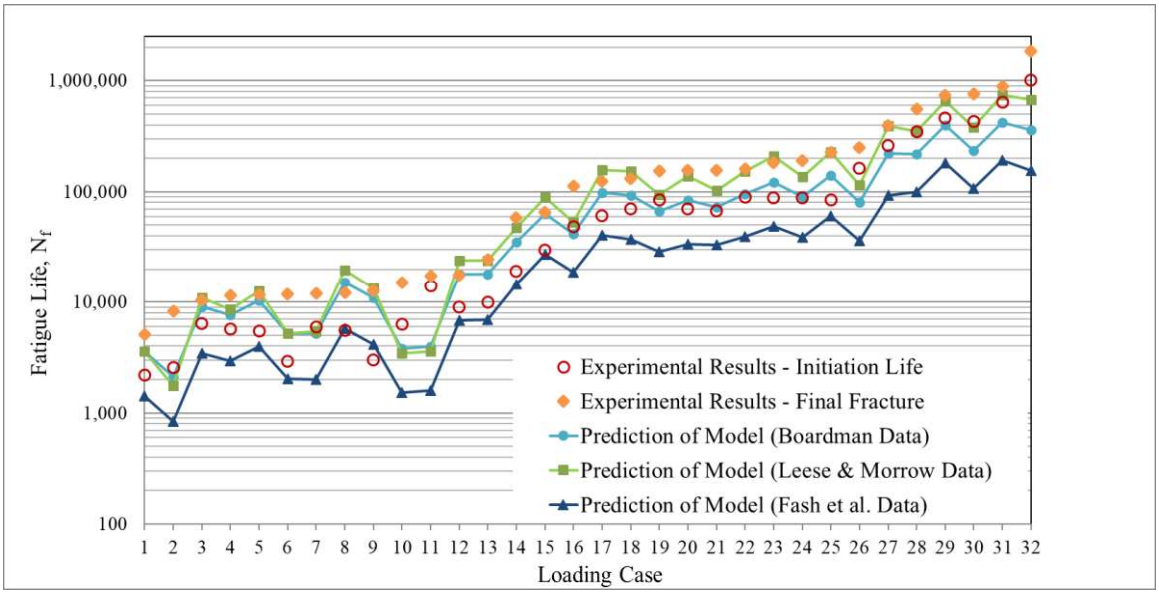

Figure 4.16. Correlation between the experimental results given by [73,74] and the model predictions obtained using the fatigue properties reported by Boardman [76], Leese and Morrow [75], and Fash et al. [74].

There is a high harmony between experimental data and model estimates in terms of increasing and decreasing trends. Correlation coefficients calculated for the three different data sets are above 0.90. Moreover, fatigue life estimations performed using the material properties reported by Boardman [76] and, Leese and Morrow [75] show satisfactorily small deviations from the experimental values. 91% of the results calculated using the data by Leese & Morrow remain within the 3x range, while only two values figured with the Boardman's data slightly exceeds this band. On the other hand, as a matter of fact, analyses based on the material properties reported by Fash et al. [74] yield a bit conservative results. Figures 4.18-20 graphically show the deviation ranges of the model predictions from the experimental values.

Figure 4.17 shows the contours of strain energy density, SED, (J/m^3) for the filleted specimen subjected to a bending moment of 1220 Nm and torsion of 1700 Nm. The fatigue lives for uniformly stressed parts corresponding to the contour values are also shown. The threshold SED is 80,633 J/m^3 for the material calculated based on the values of fatigue lives reported by Boardman [76]. Accordingly, the regions shown by the dark blue color are assumed not to contribute to the fatigue life of the specimen. A smaller region has a SED larger than 316,435 J/m^3, which corresponds to 10^4, cycles of fatigue life. The algorithm

calculates the fatigue life of the specimen as 98,067 cycles for this strain energy distribution, while the measured crack initiation and final fatigue lives are 60,800 and 124,500 cycles, respectively. It should be noted that the nominal equivalent stress is 304 MPa for this loading, which is close to the yield strength of the material; therefore, SED of regions away from the notch is above the threshold value of strain energy. In the proposed fatigue assessment model, normally all the points around the notch having SED above its threshold value are considered. However, including the regions away from the notch is not realistic in fatigue assessment; for this reason, only the part of the beam having equivalent stress 2% above the nominal stress is included in fatigue calculations. If a part contains a number of notches or SED of noncritical regions are above the threshold value, then only the regions around the notch for which fatigue assessment is made should be considered.

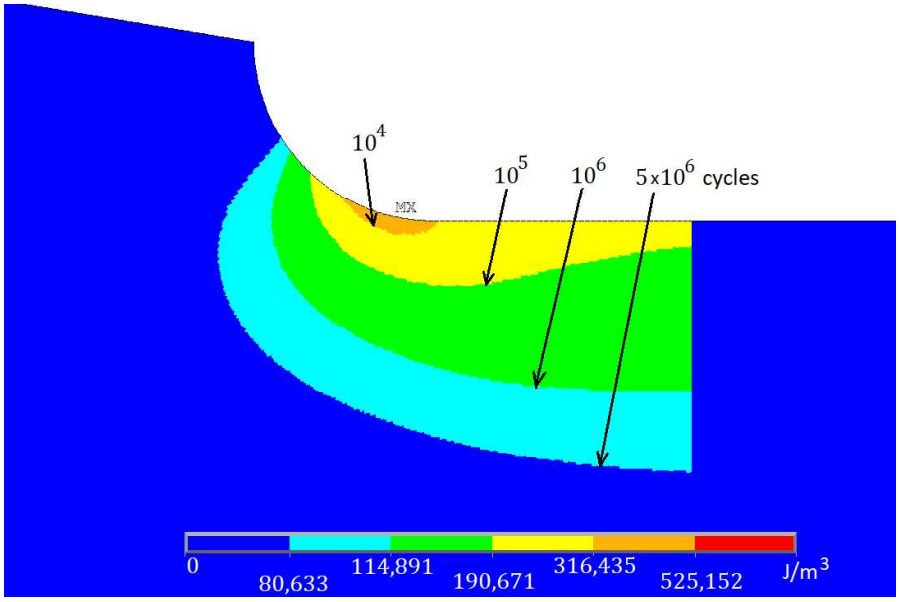

Figure 4.17. Strain energy density contours in the specimen subjected to a bending moment of 1220 Nm and torsion of 1700 Nm and the fatigue lives for uniformly stressed parts corresponding to the contour values. The threshold SED is 80,633 J/m^3 for the material.

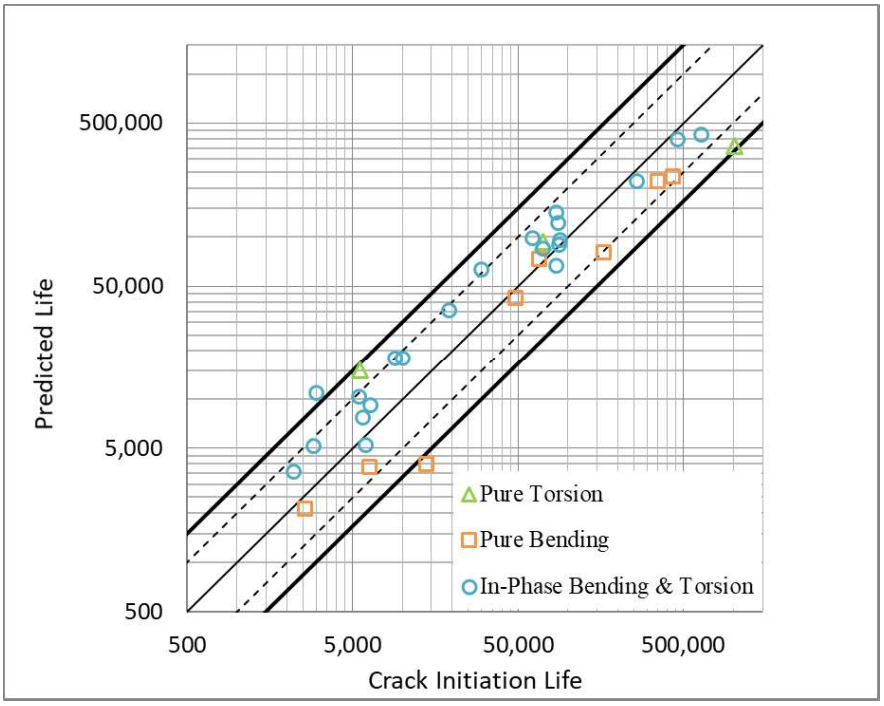

Figure 4.18. Experimental vs. predicted fatigue life computed using the material properties reported by Boardman [76]. Mean square error of the scatter is equal to 1.78.

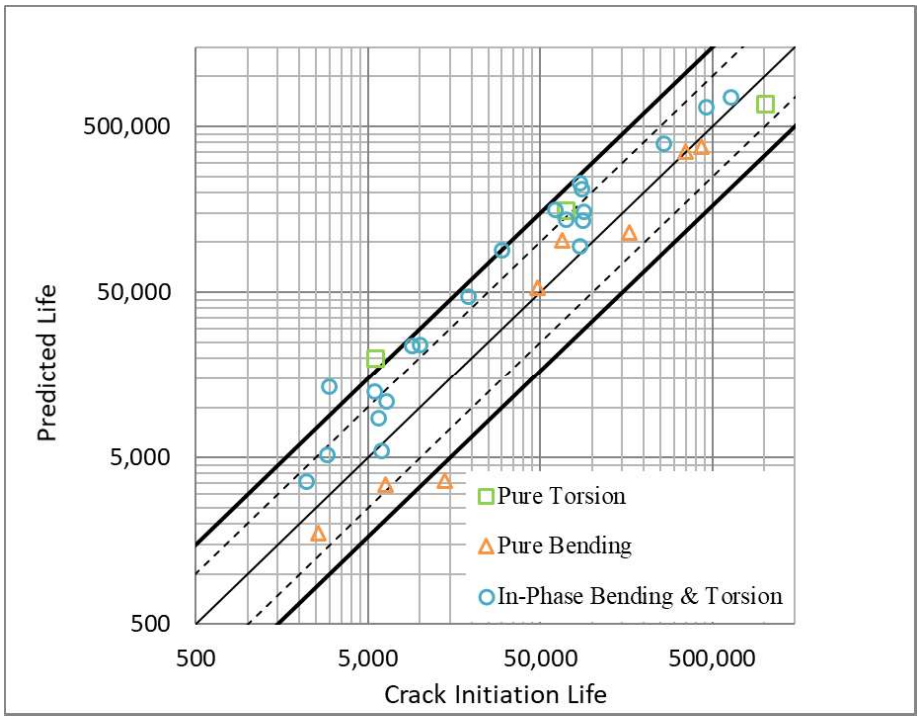

Figure 4.19. Experimental vs. predicted fatigue life computed using the material properties reported by Leese and Morrow [75]. Mean square error of the scatter is equal to 2.06.

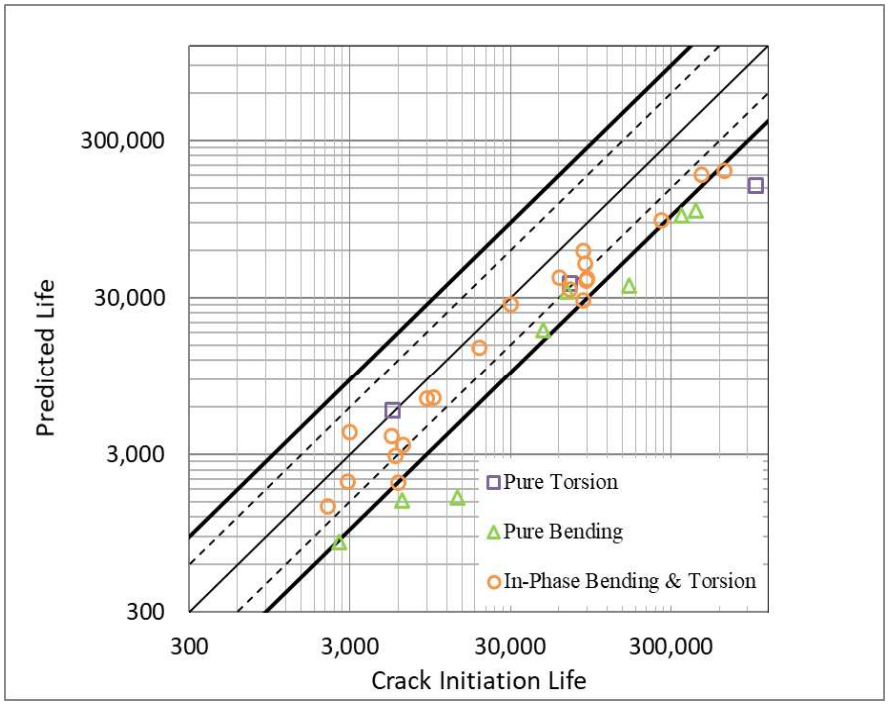

Figure 4.20. Experimental vs. predicted fatigue life computed using the material properties reported by Fash et al. [74]. Mean square error of the scatter is equal to 2.59.

4.2.4. Modeling and Results for En3B Grooved Shaft Specimens

Prediction capability of the model is further evaluated by considering the experimental data reported by Susmel and Taylor [1] for En3B steel circular shaft specimens with V-grooves of two different radii of curvature. The specimen configuration and dimensions are depicted in Figure 4.21.

Application of the proposed fatigue-life assessment methodology requires some material values to be known. On the other hand, only the static mechanical properties of the examined material are provided in the reference (see Table 4.9). The cyclic properties such as fatigue strength coefficient, σ_f', and exponent, b, are not given. Experimental determination of the values for these material properties is a very laborious and costly process. Fortunately, using some relations available in the literature, a correlation can be established between monotonic and cyclic material properties. Among these relations, the universal slopes method developed by Manson and Hirschberg [77], Bäumel-Seeger uniform material law method [78], Muralidharan-Manson modified universal slopes method [79]

and Roessle-Fatemi hardness method [28] are the most used methods in the literature for the estimation of fatigue parameters.

The modified universal slopes formula proposed by Muralidharan and Manson is given by [80],

$$\frac{\Delta\varepsilon}{2} = \varepsilon_a = 0.623\left(\frac{\sigma_u}{E}\right)^{0.832}\left(2N_f\right)^{-0.09} + 0.0196\left(\varepsilon_f\right)^{0.155}\left(\frac{\sigma_u}{E}\right)^{-0.53}\left(2N_f\right)^{-0.56} \quad (4.5)$$

where, σ_u is the ultimate tensile strength and ε_f is the true fracture ductility. Accordingly, using Equation (4.5) in conjunction with the Coffin-Manson-Basquin formula, the fatigue parameters are calculated as $\sigma_f' = 0.623E(\sigma_u/E)^{0.832}$ and $b = -0.09$.

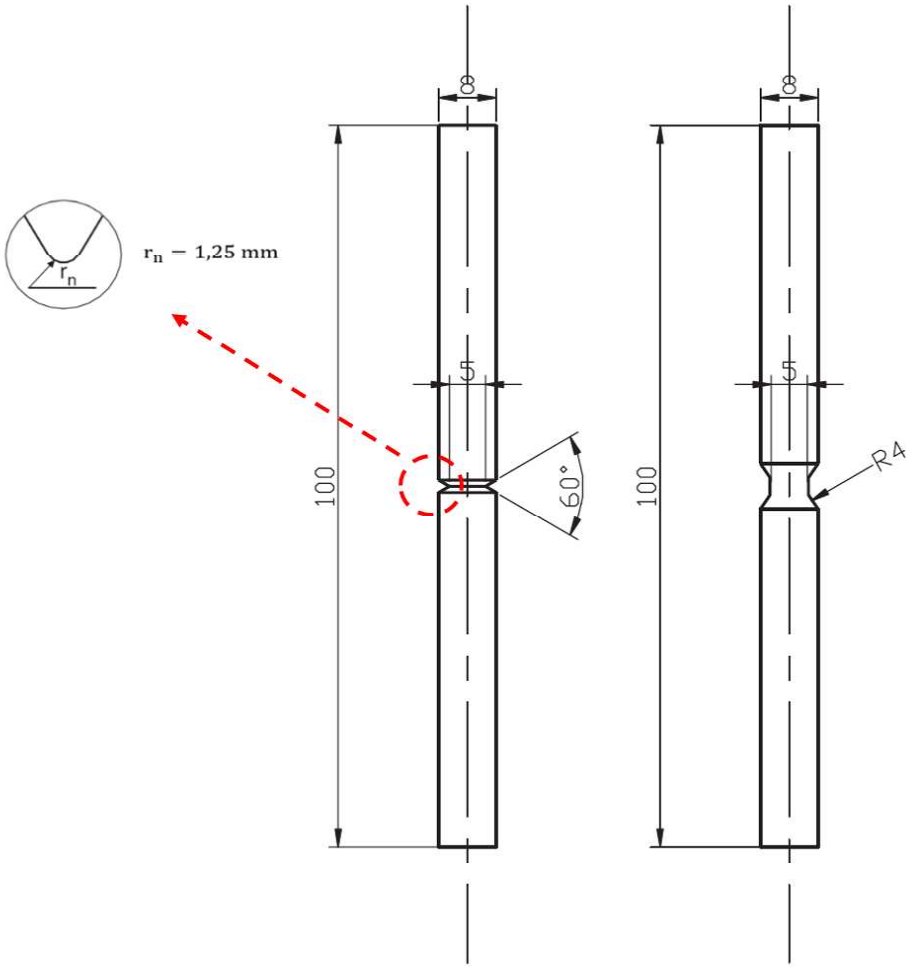

Figure 4.21. En3B notched shaft specimen geometries and dimensions [1]. All dimensions are given in mm.

Table 4.9. Static properties of En3B cold rolled low-carbon steel [1].

Elastic Modulus, E (Pa)	2.085E+11
Ultimate Tensile Strength, σ_u (Pa)	6.76E+08
Yield Strength, σ_y (Pa)	6.53E+08

The specimen geometries are axisymmetric. On the other hand, to test the correspondence between the results obtained both in two-dimensional and three dimensional spaces and to show more explicitly the application of forces and boundary conditions to the model, analyses are carried out for both 2D and 3D geometries. The finite element model in three-dimensional space is illustrated in Figure 4.22.

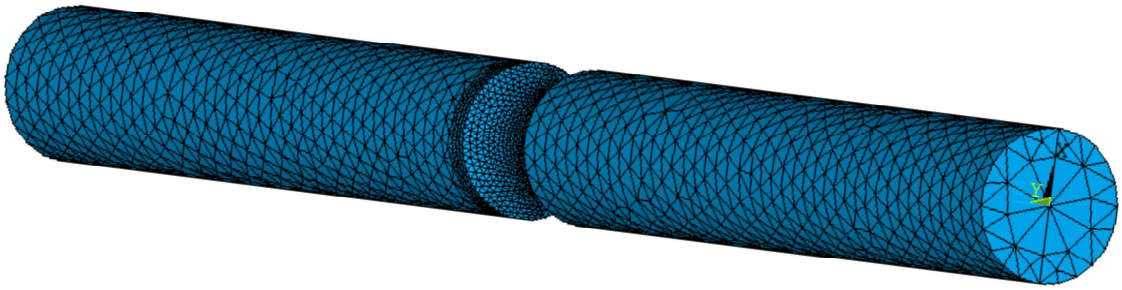

Figure 4.22. The 3D finite element model of En3B grooved shaft specimen with 4 mm radius of curvature.

The model is meshed with SOLID187 elements, which is a high order 3-D, 10 node tetrahedral structural solid element. This element has a quadratic displacement behaviour and it is well suited for irregular geometries.

The specimen is subjected to different combinations of torsional and axial loads. In order to prevent the highly stressed regions to form in the structure due to point loads, again, extra sections with the same material properties as specimen are appended to both ends of the main model of the specimen. Torsional load is applied by a force couple at the bottom end and axial stress is defined on the same surface. On the other hand, the movement of the top surface is restricted in all directions. The boundary conditions can be seen in Figure 4.23.

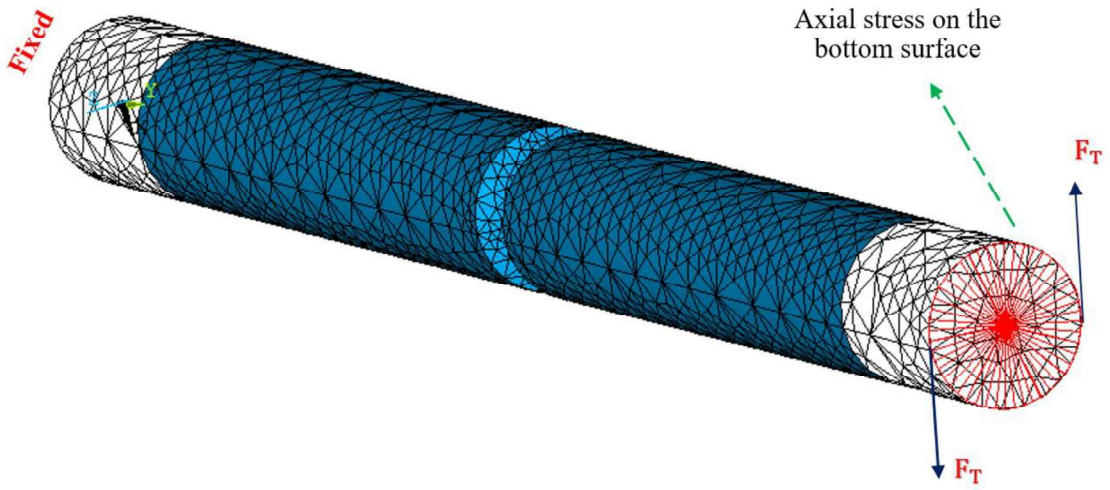

Figure 4.23. Loading pattern of En3B grooved shaft specimen.

Table 4.10 gives the empirical results reported by Susmel and Taylor [1] and the predictions of the model corresponding to the nominal tensile and shear stresses at the smallest section. It is worth noting that, since an approximate universal method is employed to determine the fatigue properties of the material based on its static strength instead of using experimentally obtained values for cyclic properties, the accuracy of the results is questionable. On the other hand, as can be seen in Figure 4.24, a graphically good correspondence is achieved. The upward/downward tendencies are correctly captured. The value of the calculated correlation coefficient is 0.96.

In reference [1], the experimental data are provided for ultimate fracture lifetimes. In this respect, remembering that the presented model is developed to predict fatigue-initiation life, it is quite reasonable that the estimates obtained from the model are somewhat conservative. Nevertheless, all but one of the results stay within the error factor of 3.0. Considering that, a significant part of fatigue life is spent on crack formation in high cycle fatigue and the estimated lives are on the conservative side, but within the acceptable band, it can be concluded that if the experimental data were given for crack initiation lives, the predicted results would show a better correlation. Figure 4.25 shows the graphic interpretation of the results. The mean square error of the scatter is calculated as 2.02. One can say that the model estimates are in sound agreement with the reported experimental data for En3B steel grooved shaft specimens.

Table 4.10. Experimental results for En3B steel notched shaft specimens reported in the study [1] and the estimates of the presented model.

Loading Case	Radius of Curvature r (mm)	Nominal Axial Stress (MPa)	Nominal Torsional Stress (MPa)	Equivalent Nominal Stress (MPa)	Stress Concentration Factor $K_t = \frac{\sigma_{eqv,max}}{\sigma_{eqv,nom}}$	Final Fracture Life	Predicted Initial Life
1	1.25	275	158.8	388.9	1.45	46,254	28,320
2	1.25	259.6	155.9	374.6	1.45	82,952	40,290
3	1.25	230	132.8	325.3	1.45	188,480	117,229
4	1.25	200	115.5	282.9	1.45	437,907	328,901
5	1.25	190	109.7	268.7	1.45	1,400,006	465,387
6	1.25	180	103.9	254.5	1.45	2,174,897	670,831
7	4	370	213.6	523.2	1.15	13,630	14,719
8	4	350	202.1	495.0	1.15	12,200	23,793
9	4	330	190.5	466.7	1.15	38,446	39,681
10	4	290	167.4	410.1	1.15	282,833	116,720
11	4	280	161.7	396.0	1.15	73,994	155,757

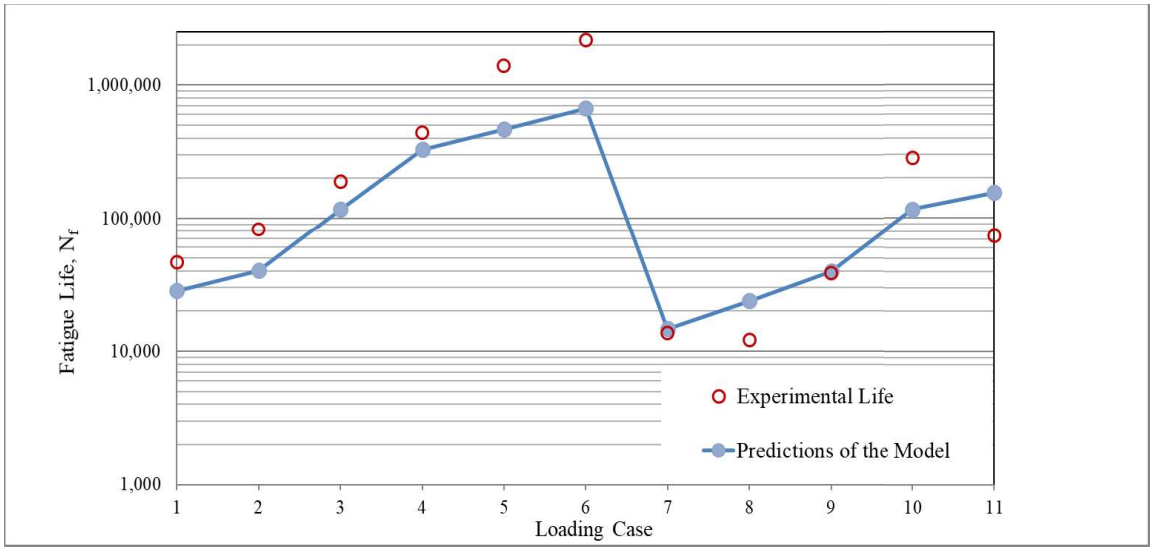

Figure 4.24. Correlation between the model predictions and the measured final fatigue lives reported by Susmel and Taylor [1].

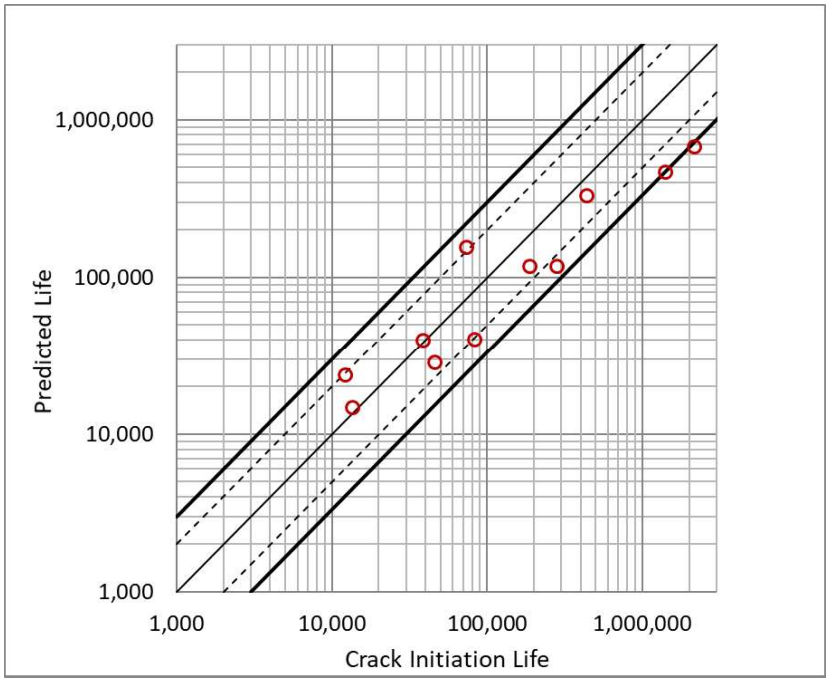

Figure 4.25. Experimental vs. predicted fatigue life for En3B notched specimens.

4.2.5. Modeling and Results for SAE 1045 Solid Cylindrical Specimen with Transverse Circular Hole

Apart from groove and fillet, another stress-increasing geometric irregularity frequently encountered in mechanical structures is holes. To support the argument that the presented model is valid for all parts regardless of their geometric characteristics, the model is further applied to SAE 1045 solid cylindrical specimens with transverse circular hole. The geometry of the specimen is drawn in Figure 4.26 and the material properties reported by Kurath et al. [81] are given in the Table 4.11.

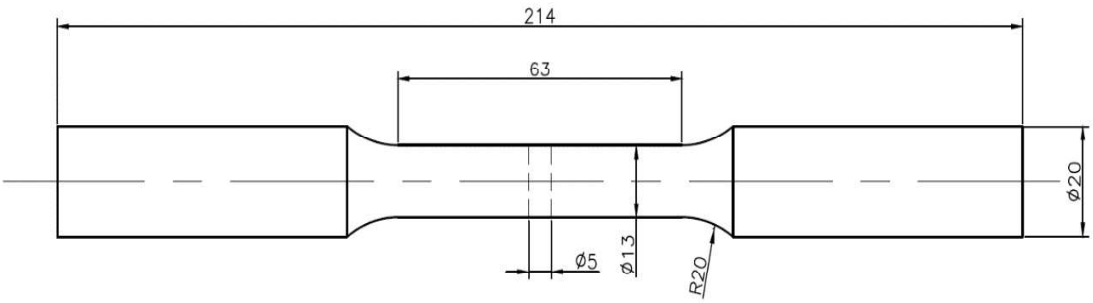

Figure 4.26. Shape and dimensions of SAE 1045 solid cylindrical specimen with transverse circular hole. All dimensions are given in mm.

Table 4.11. Mechanical properties of SAE 1045 steel material [81].

Elastic Modulus, E (Pa)	2.04E+11
Poisson's Ratio, v	0.28
Shear Modulus, G (Pa)	8.03E+10
Axial Fatigue Strength Coefficient, σ_f' (Pa)	9.3E+08
Axial Fatigue Strength Exponent, b	-0.106
Axial Fatigue Ductility Coefficient, ε_f' (Pa)	0.298
Axial Fatigue Ductility Exponent, c	-0.49
Yield Strength, σ_y (Pa)	3.8E+08
Ultimate Tensile Strength, σ_u (Pa)	6.21E+08

Unlike the samples examined previously, specimens with notches in the form of transverse circular holes do not have axisymmetric geometries. This necessitates the analyses to be carried out in three-dimensional space. The finite element model around the critical region is shown in Figure 4.27. Linear elastic finite element analysis is performed using SOLID187 type elements. Because the model is highly sensitive to changes in element size, the regions around the hole are refined as is done for other stress raisers to obtain more accurate results. The finite element model includes 718,654 elements and 987,954 nodes.

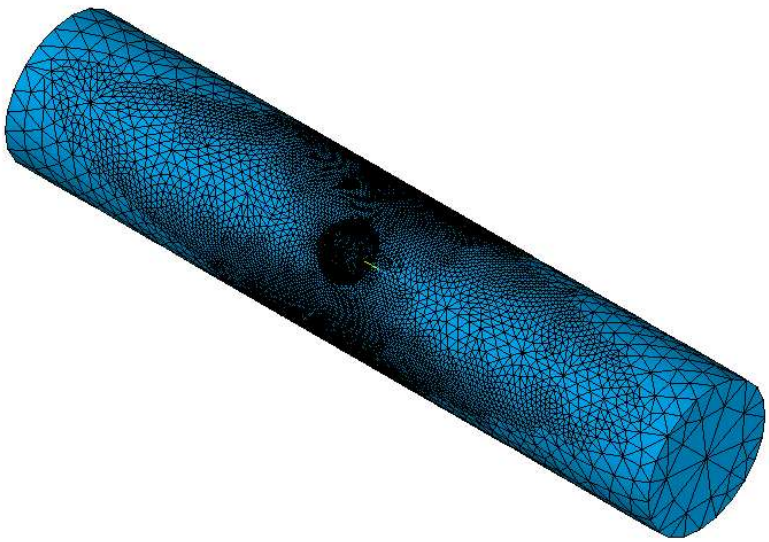

Figure 4.27. FEM meshes of SAE 1045 solid cylindrical specimen with transverse circular hole.

The circular bar is exposed to several fully reversed axial and torsional loads with four different biaxiality ratios. The values of the biaxiality ratio are 0 (pure tension), 0.5, 2 and ∞ (pure torsion). Since the application forms of loads and boundary conditions are identical to the previous sample, it will be sufficient to take a glance at Figure 4.23 to visualize the loading model.

As may be recalled, it was mentioned that as the distance from the notch increases, the effect of high-energy elements on the calculated fatigue life in that region decreases substantially. This problem was solved for specimens with groove and fillet shaped notched parts, by considering only the elements from the point where the equivalent streess reaches 2% above the nominal stress. For the parts with a hole, significant portion of the elements have calculated lives shorter than the threshold life for certain load levels. In order to prevent consideration of elements far from the hole in fatigue-life calculations, only the elements within the cylindrical region having two times the radius of the hole are taken into account.

Experimental results by Yip and Yan [82] and calculated values of crack initiation life are given in Table 4.12.

Table 4.12. Experimental results for AISI 1141 notched shaft specimens reported in [82] and the estimates of the presented model.

Loading Case	Biaxiality Ratio	Equivalent Nominal Stress (MPa)	Axial Nominal Stress (MPa)	Torsional Nominal Stress (MPa)	Stress Concentration Factor $K_t = \frac{\sigma_{eqv,max}}{\sigma_{eqv,nom}}$	Experimental Life	Predicted Life
1	0	177.4	177.4	0	4.50	1,317	457
2	0	162.6	162.6	0	4.50	2,074	1,023
3	0	147.8	147.8	0	4.51	4,372	2,454
4	0	133.0	133	0	4.50	9,735	6,331
5	0.5	196.5	148.5	74.3	3.93	1,110	1,111
6	0.5	168.5	127.3	63.7	3.94	3,659	4,534
7	0.5	159.0	120.2	60.1	3.94	4,907	7,582
8	0.5	149.7	113.2	56.6	3.93	8,577	12,826
9	2	209.8	58.2	116.4	3.02	1,696	11,190
10	2	192.4	53.4	106.7	3.03	3,543	22,161
11	2	174.9	48.5	97	3.03	5,956	43,285
12	2	157.4	43.7	87.3	3.02	15,084	82,988
13	∞	236.4	0	136.5	2.52	955	7,691
14	∞	216.7	0	125.1	2.52	2,434	15,863
15	∞	196.9	0	113.7	2.52	4,149	33,548
16	∞	177.2	0	102.3	2.52	9,538	71,463

Figure 4.28 presents the correlation of the model predictions with the experimental fatigue data. The correlation coefficient for that geometry is calculated as 0.74. As the biaxiality ratio increases, in other words, as the shear stress effect becomes dominant, it is seen in Figure 4.29 that the results of the model diverge from the experimental data. Nevertheless, the deviations do not reach very high values. The maximum value of the ratio of model estimates to experimental data is 8.08. The average scatter of the results falls on the scale band of coefficient 4.17.

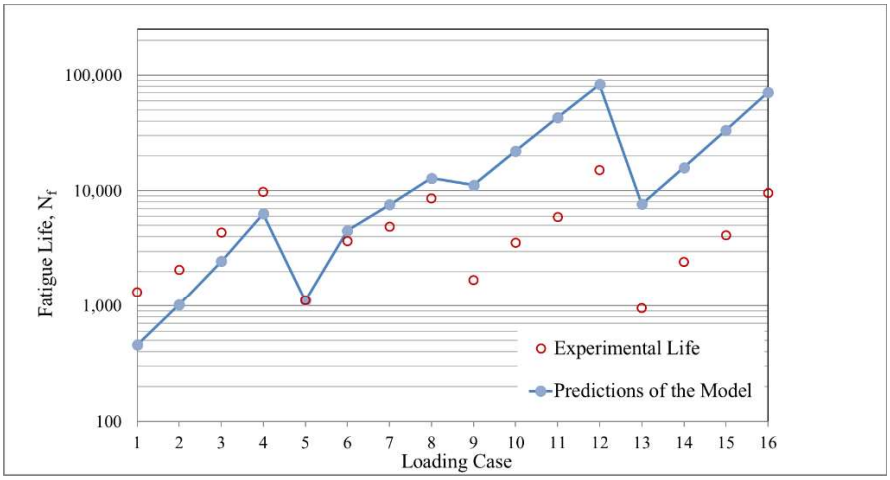

Figure 4.28. Correlation between experimental and theoretical fatigue lives of SAE 1045 solid cylindrical specimen with transverse circular hole.

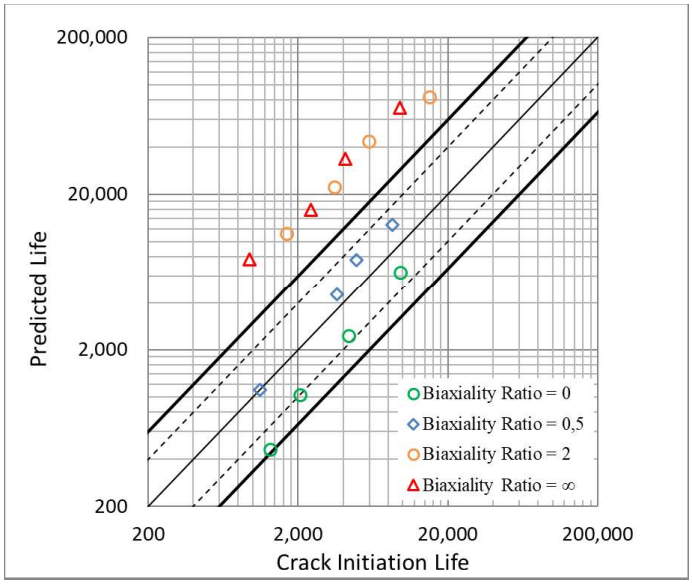

Figure 4.29. Experimental vs. predicted fatigue life for SAE 1045 solid cylindrical specimen with transverse circular hole.

4.2.6. Modeling and Results for 2024-T3 Aluminium Alloy Notched Tubular Specimen with a Hole

In order to check the accuracy of the presented methodology in estimating number of cycles for crack initiation, a tubular specimen with a transverse hole and subjected to in-phase tension and torsion is selected from the technical literature [72]. The geometry and the dimensions of the sample is sketched in Figure 4.30.

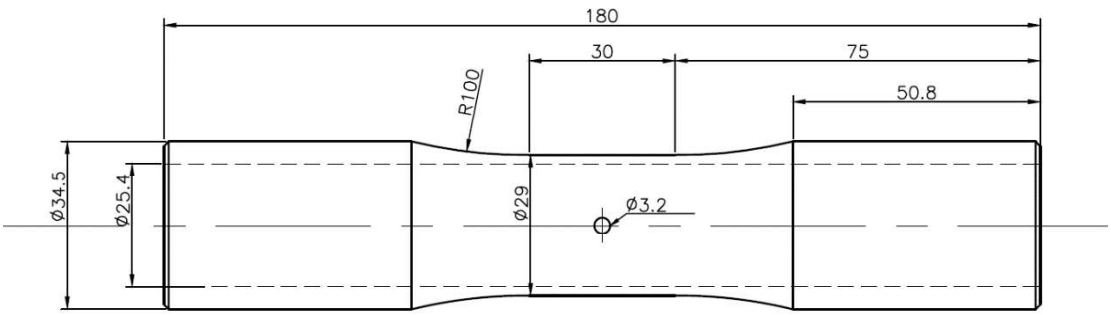

Figure 4.30. Shape and dimensions of 2024-T3 aluminium alloy notched tubular specimen. All dimensions are given in mm.

A prominent feature of the presented model that makes it stand out among many other models available in the literature is that its applicability is not confined to steel materials only. Here, a specimen made of a non-steel material is chosen to corroborate applicability of the model for other materials as in Section 4.2.1. Static and cyclic properties of 2024-T3 aluminium alloy are tabulated in Table 4.13.

Table 4.13. Mechanical properties of the 2024-T3 aluminium alloy [72].

Elastic Modulus, E (Pa)	7.34E+10
Poisson's Ratio, ν	0.343
Axial Fatigue Strength Coefficient, $\sigma_f{}'$ (Pa)	11.942E+08
Axial Fatigue Strength Exponent, b	-0.133
Axial Fatigue Ductility Coefficient, $\varepsilon_f{}'$ (Pa)	0.066
Axial Fatigue Ductility Exponent, c	-0.445
Yield Strength, σ_y (Pa)	3.30E+08
Ultimate Tensile Strength, σ_u (Pa)	4.95E+08

Since the procedure followed for the said specimen is exactly similar to the previous one, rest of this subsection will not be elaborated further.

The meshed geometry of the specimen generated with SOLID187 elements is displayed in Figure 4.31. The finite element mesh is made denser around the hole to obtain more accurately the stress and strain distribution in the notch area.

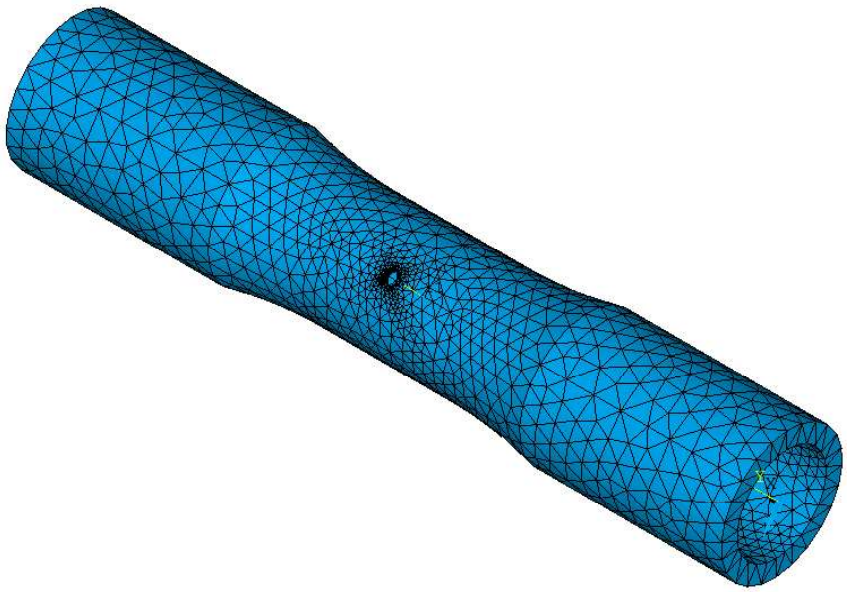

Figure 4.31. The finite element model of 2024-T3 aluminium alloy tubular specimen with a hole.

The presented model is developed to predict the fatigue life of parts under multiaxial loading conditions. However, in the literature, a vast majority of the experimental data are given for uniaxial loading for this geometry. On the other hand, considering that, uniaxial loading is a special case of multiaxial one and a multiaxial stress state occurs around a stress raiser even in cases of uniaxial loading, one can say that uniaxial test data can be used for verification purposes. Empirical and theoretical fatigue lives are listed in Table 4.14.

Table 4.14. Experimental results for 2024-T3 aluminium alloy notched tubular specimen reported in [72] and the estimates of the presented model.

Loading Case	Axial Nominal Stress (MPa)	Torsional Nominal Stress (MPa)	Equivalent Nominal Stress (MPa)	Stress Concentration Factor $K_t = \frac{\sigma_{eqv,max}}{\sigma_{eqv,nom}}$	Experimental Life	Predicted Life
1	145	0	145	3.14	9,500	32,692
2	130	0	130	3.14	26,335	71,161
3	115	0	115	3.14	140,525	158,127
4	98	0	98	3.14	735,000	226,371
5	0	108	187.1	2.36	18,500	49,052
6	0	91	157.6	2.36	66,015	161,181
7	0	76	131.6	2.36	215,000	463,792
8	125	72	176.6	2.96	5,500	14,232
9	81	50	118.6	2.94	216,000	214,256

Figure 4.32 gives a graphical interpretation to how the estimates obtained from the model match with the empirical results. The correlation coefficient is calculated as 0.49 and mean square error is 2.44. Relationship between experimental data and model predictions can be seen more clearly in Figure 4.33. The results are within the acceptable limits or close to them.

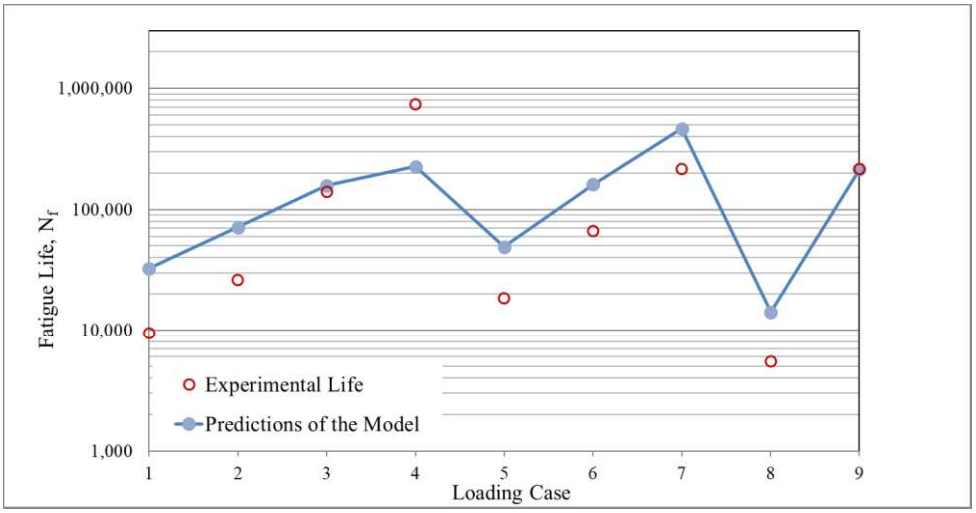

Figure 4.32. Correlation between experimental and theoretical fatigue lives of 2024-T3 aluminium alloy notched tubular specimen.

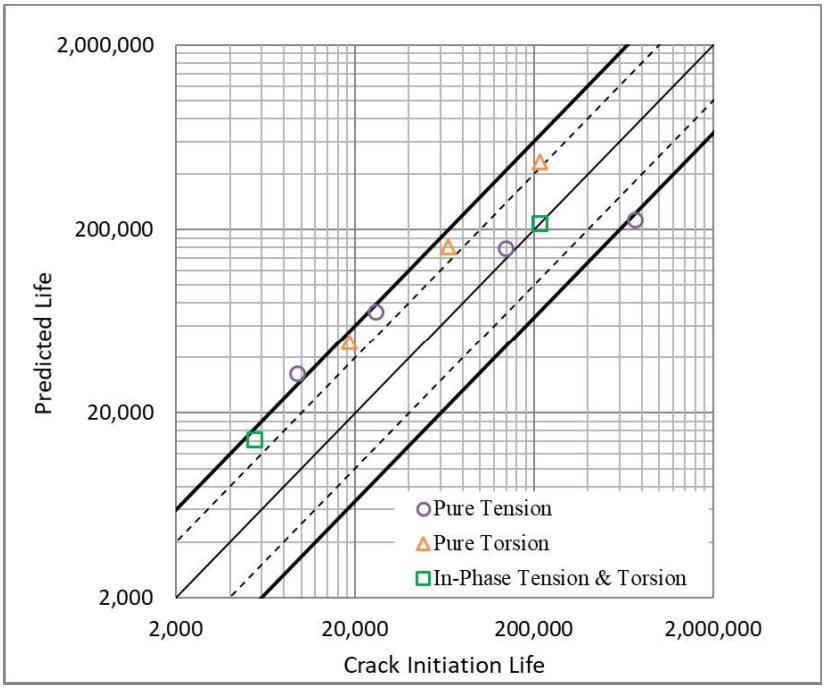

Figure 4.33. Experimental vs. predicted fatigue life for 2024-T3 aluminium alloy notched tubular specimen.

4.2.7. Modeling and Results for S460N Shouldered Shaft Specimen

The current model is lastly validated for S460N shouldered shaft specimen. Figure 4.34 picturizes the specimen geometry and dimensions. In order to avoid falling into repetition, again, only the points not mentioned in the other subsections will be detailed.

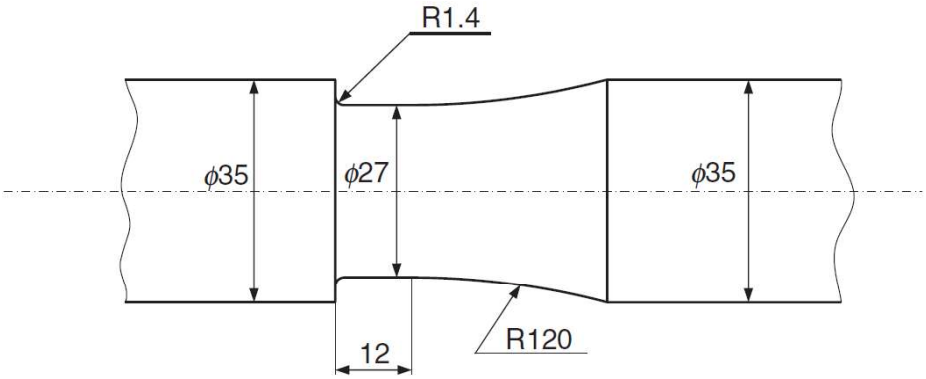

Figure 4.34. Shape and dimensions of S460N shouldered shaft specimen [83]. All dimensions are given in mm.

The specimen is made of micro alloyed fine grained structural steel S460N (FeE460). Mechanical properties of S460N steel reported by Hoffmeyer et al. [84] are listed in Table 4.15.

Table 4.15. Mechanical properties of S460N steel material [84].

Elastic Modulus, E (Pa)	2.085E+11
Poisson's Ratio, v	0.3
Shear Modulus, G (Pa)	8.02E+10
Axial Fatigue Strength Coefficient, $\sigma_f{}'$ (Pa)	9.696E+08
Axial Fatigue Strength Exponent, b	-0.086
Axial Fatigue Ductility Coefficient, $\varepsilon_f{}'$ (Pa)	0.281
Axial Fatigue Ductility Exponent, c	-0.493
Yield Strength, σ_y (Pa)	5.00E+08
Ultimate Tensile Strength, σ_u (Pa)	6.43E+08

A finite element model around the stress raiser in bi-dimensional space is depicted in Figure 4.35. In parallel with the preceding axisymmetric examples, PLANE83 is determined as the element type.

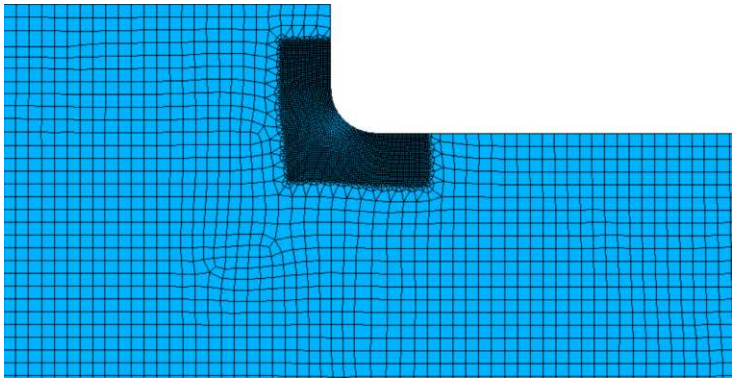

Figure 4.35. The meshed geometry of a region around the notch of S460N shouldered shaft specimen. The finite element model includes 44,995 elements and 136,762 nodes.

The specimen is subjected to in-phase tension and torsion. The loads are applied to the structure just as in the first example (see Figure 4.4). Elements belonging to the appended regions are excluded so that stress concentrations in these regions due to the applied point forces are not considered in fatigue-life calculations. Again, only the sections where the maximum equivalent stress is at least 2% above the nominal stress are considered in the calculations.

The experimental values are supplied from the Susmel's compilation [83]. The fatigue life results related to the model and the experimental study are summarized in Table 4.16.

Table 4.16. Experimental results for S460N shouldered shaft specimen available in [83] and the estimates of the presented model.

Loading Case	Nominal Tensile Stress (MPa)	Nominal Torsional Stress (MPa)	Equivalent Nominal Stress (MPa)	Stress Concentration Factor $K_t = \frac{\sigma_{eqv,max}}{\sigma_{eqv,nom}}$	Experimental Crack Initiation Life, $N_{f(exp)}$	Predicted Life, N_f
1	300	262	544.5	1.79	225	964
2	225	197	408.7	1.79	4,317	14,301
3	150	131	272.5	1.79	74,019	391,338
4	125	109	226.8	1.79	903,597	515,038

The increasing-decreasing trends of the experimental data and the model predictions can be seen in Figure 4.36 and the severity of the deviation in the predicted results is revealed by the subsequent graph. As can be seen in Figure 4.37, all values but one fall slightly out of error factor of 3.0. The calculated mean square error of the scatter is equal to 3.63.

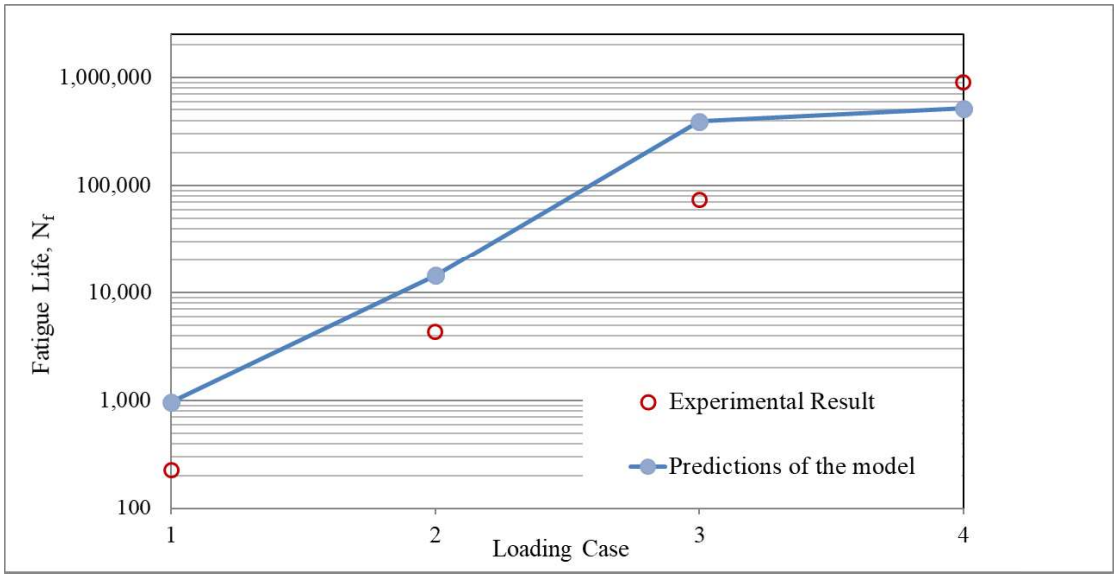

Figure 4.36. Correlation between experimental and theoretical fatigue lives of S460N shouldered shaft specimen.

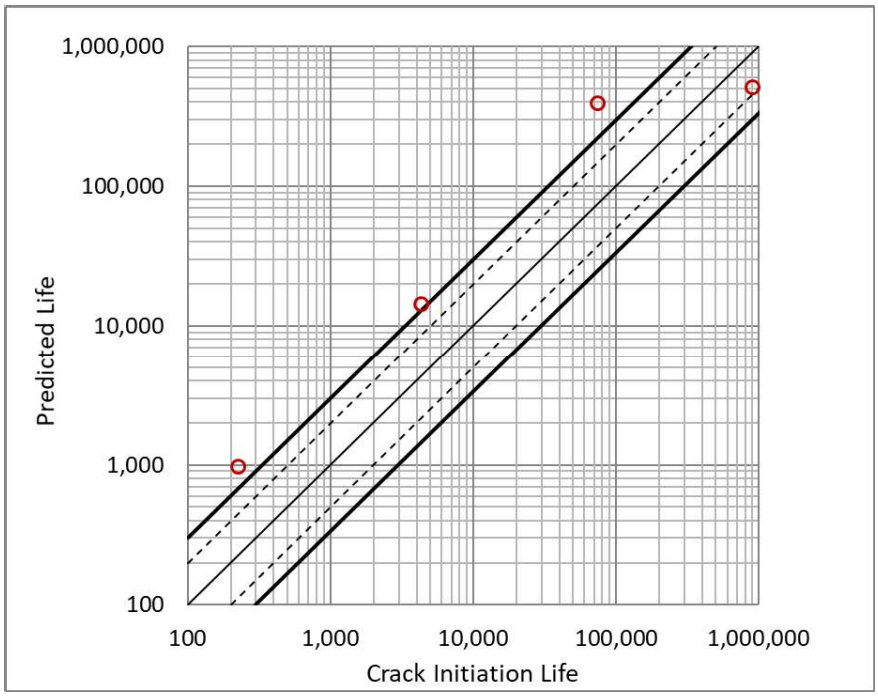

Figure 4.37. Experimental vs. predicted fatigue life for S460N notched specimen.

4.3. Mean Stress Effect

Besides fully reversed loads, fluctuating loads superposed on a static load also appear commonly in engineering applications. Accordingly, it is extremely important to consider the mean stress effect in fatigue design processes in order to extend the scope of applicability of a model. On the other hand, in the presence of geometric discontinuities, accurately modelling the mean stress effect is a quite complicated issue. The first steps in understanding the influence of non-zero mean stress on fatigue were taken by Sines [85] and Smith [86]. Sines' studies have shown that tensile mean stresses have a detrimental effect on fatigue life while compressive mean stresses lead to positive effects. Also, Smith has found that mean shear stress has no significant effect on fatigue life.

Mean stress effect is incorporated in fatigue parameters in different ways. Fatemi and Socie [3], in order to reflect the effects of asymmetric loads, replaced the normal component of the strain in Brown and Miller's model by the maximum value of normal stress (see Equation (2.2)). Ince and Glinka [44], on the other hand, took into account the mean shear stress effect via the maximum shear stress term in their so-called generalized strain energy (GSE) damage parameter (see Equation (2.35)). Susmel and Taylor [1] accounted for this effect with a newly introduced stress ratio parameter. Their parameter included a material dependent constant called mean stress sensitivity index (see Equation (2.28)).

The common feature of the above-mentioned models is that they all work on the critical plane basis. It is known that critical plane approaches are superior in reflecting loading-dependent effects such as mean stress and non-proportionality. For the presented model, such corrections alone will not be sufficient in explaining the effect in question. Nevertheless, the model can be reformulated to adequately account for the mean stress effect. For this purpose, Smith-Watson-Topper (SWT) model is taken as the starting point in this study. According to SWT model [25], the fatigue life, N_f, can be obtained using the following relation:

$$\sigma_{max}\varepsilon_a E = \sigma_{max}\sigma_a = \sigma_f'^{2}\left(2N_f\right)^{2b} + \sigma_f'\varepsilon_f' E\left(2N_f\right)^{b+c} \tag{4.6}$$

This equation implies that any applied combination of non-zero mean stress and alternating stress is expected to result in the same life as an equivalent alternating stress applied in a reversed cycle. Accordingly, such an equivalent alternating stress, σ_{ea}, can be expressed as follows

$$\sigma_{ea} = \sqrt{\sigma_{max}\sigma_a} \tag{4.7}$$

To account for the mean stress effect, equivalent alternating strain energy density, U_{ea}, is multiplied by an introduced mean-stress factor, R_m, and an alternative value for strain energy density is obtained as

$$U'_{ea} = R_m U_{ea} \tag{4.8}$$

where R_m is the ratio of equivalent alternating stress, σ_{ea}, in Equation (4.7) to alternating stress, σ_a, given as

$$R_m = \frac{\sigma_{ea}}{\sigma_a} = \frac{\sqrt{\sigma_{max}\sigma_a}}{\sigma_a} = \sqrt{\frac{\sigma_{max}}{\sigma_a}} \tag{4.9}$$

For multiaxial stress states, σ_{max} is the peak value of Von Mises stress and σ_a is the alternating Von Mises stress.

4.3.1. Modeling and Results for En3B Grooved Shaft Specimens in the Presence of Asymmetric Loads

The reliability of the new form of the proposed model to account for the effects of mean stress is first tested on the En3B grooved shaft specimens, dealt with in Section 4.2.4, subjected to in-phase tension and torsion. Since the information about the geometry, material and modelling are given in detail in the mentioned section, only the results will be discussed in this section.

The loading cases and the corresponding experimental and theoretical fatigue lives are given in Table 4.17.

Table 4.17. Experimental results for En3B steel notched shaft specimens reported in reference [1] and the estimates of the presented model in the presence of asymmetric loads.

Loading Case	Radius of Curvature r (mm)	Amplitude of Nominal Tensile Stress (MPa)	Amplitude of Nominal Torsional Stress (MPa)	Load Ratio (Min/Max) R	Biaxiality Ratio $\lambda = \frac{\sigma_a}{\tau_a}$	Experimental Life	Predicted Life
1	1.25	190	190	0	1	34,298	15,846
2	1.25	180	180	0	1	28,108	25,212
3	1.25	170	170	0	1	110,056	41,903
4	1.25	165	165	0	1	249,286	53,364
5	1.25	160	160	0	1	370,618	68,152
6	1.25	150	150	0	1	844,615	115,071
7	4	250	144.3	0	3^(1/2)	60,384	94,735
8	4	245	141.5	0	3^(1/2)	235,611	112,315
9	4	240	138.6	0	3^(1/2)	340,599	131,747
10	4	230	132.8	0	3^(1/2)	316,599	186,049
11	4	220	127	0	3^(1/2)	488,018	266,691
12	4	200	115.5	0	3^(1/2)	476,345	533,309

Due to aesthetic concerns, unlike what is done in Section 4.2.4, correlation charts are arranged separately for two different geometries. Conformity of the model estimates with the experimental data is shown in Figures 4.38 and 4.39. The correlation coefficients are calculated as 0.99 for the specimen with a groove of 1.25 mm radius of curvature and 0.73 for the other one with 4.0 mm radius of curvature. Although the former seems superior in terms of upward / downward trends, when it comes to scattering, the predictions for the specimen with a groove of 4.0 mm radius of curvature is more consistent as can be seen in Figure 4.40. The overall mean square error of the scatter is 2.84. One should also note that there are inconsistencies in the experimental results. In the second test, although the load was reduced compared to the first test, fatigue life decreased.

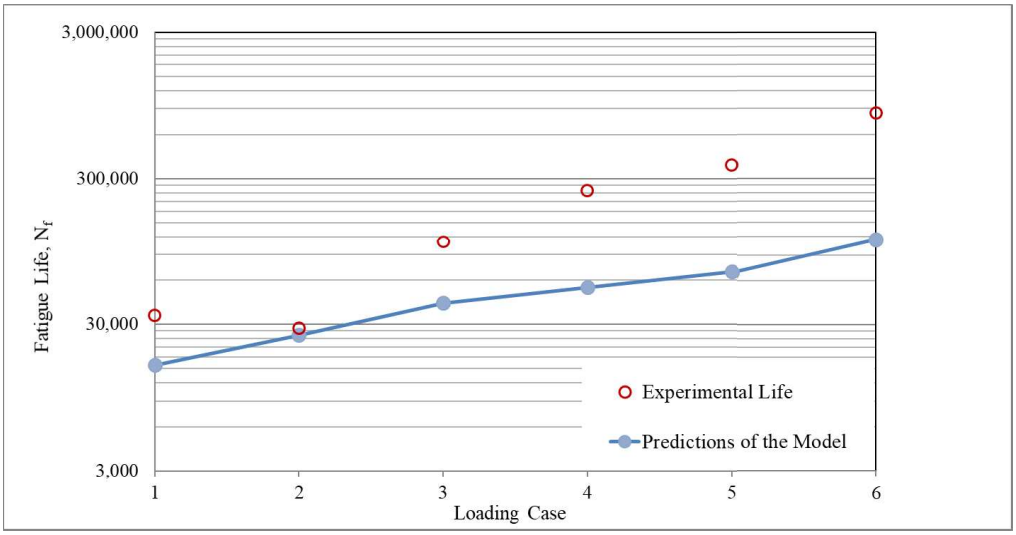

Figure 4.38. Correlation between the model predictions and the final fatigue lives for specimen with a groove of 1.25 mm radius of curvature in the presence of asymmetric loads.

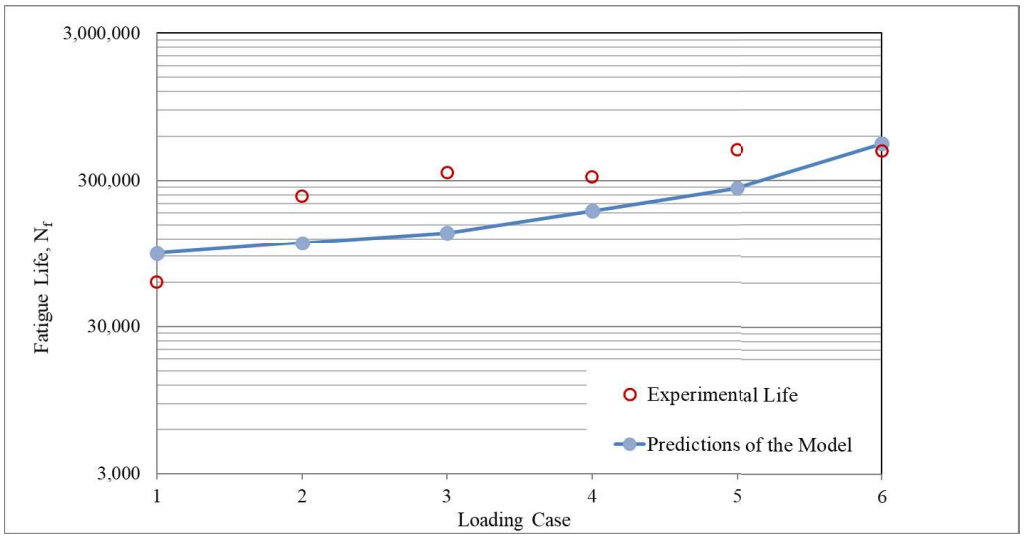

Figure 4.39. Correlation between the model predictions and the final fatigue lives for specimen with a groove of 4.0 mm radius of curvature in the presence of asymmetric loads.

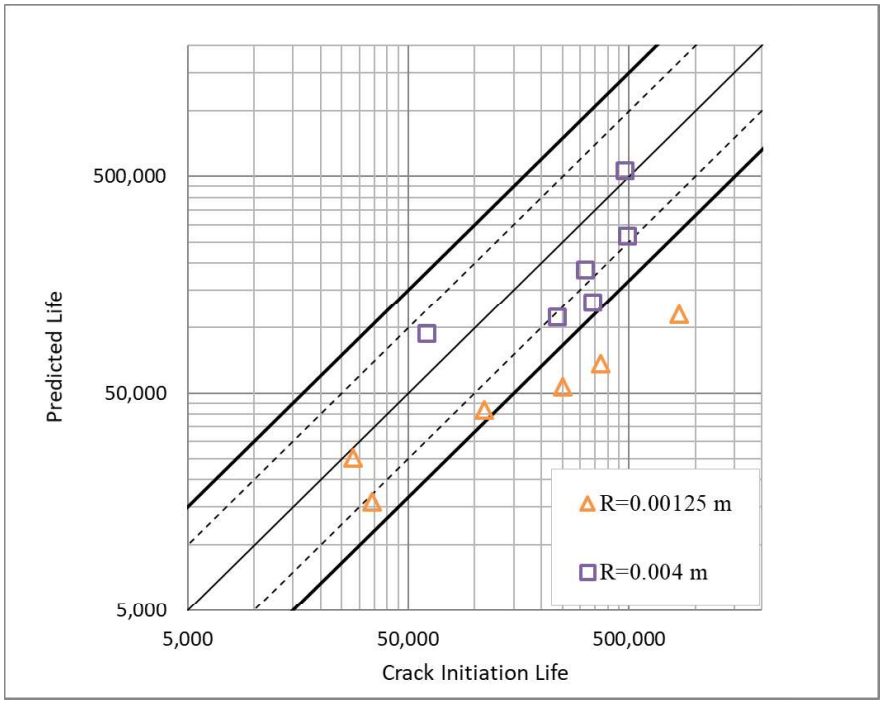

Figure 4.40. Experimental vs. predicted fatigue life for En3B notched specimens in the presence of asymmetric loads.

4.3.2. Modeling and Results for DIN 34CrNiMo6 Round Bar with a Lateral U-Shaped Notch in the Presence of Asymmetric Loads

The capability of the model to account for the effects of non-zero mean stress is checked lastly on the DIN 34CrNiMo6 round bar with a lateral U-shaped notch using the experimental data reported by Branco et al. [4,50,51]. Figure 4.41 illustrates a drawing of the geometry of the specimen.

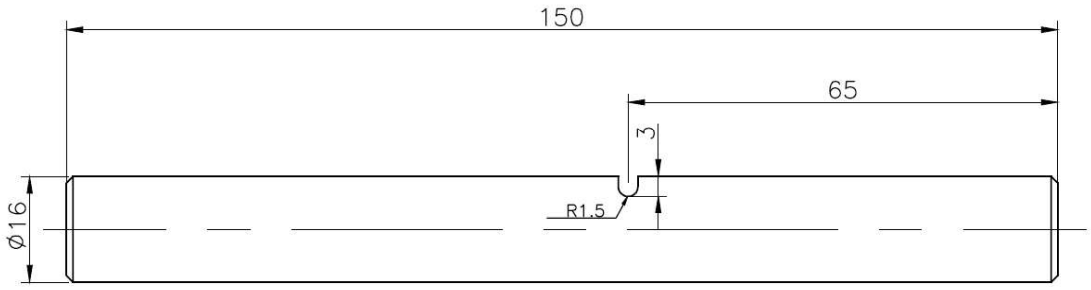

Figure 4.41. Shape and dimensions of DIN 34CrNiMo6 specimen with a lateral U-shaped notch. All dimensions are given in mm.

Monotonic and fatigue properties of DIN 34CrNiMo6 high strength steel material provided by reference [50] are summarized in Table 4.18.

Table 4.18. Mechanical properties of DIN 34CrNiMo6 high strength steel [50].

Elastic Modulus, E (Pa)	2.098E+11
Poisson's Ratio, v	0.296
Axial Fatigue Strength Coefficient, $\sigma_f{}'$ (Pa)	11.837E+08
Axial Fatigue Strength Exponent, b	-0.0545
Axial Fatigue Ductility Coefficient, $\varepsilon_f{}'$ (Pa)	0.4697
Axial Fatigue Ductility Exponent, c	-0.6059
Yield Strength, σ_y (Pa)	9.67E+08
Ultimate Tensile Strength, σ_u (Pa)	1.035E+09

The FE mesh of the geometric model for the specimen generated using SOLID187 elements is shown in Figure 4.42.

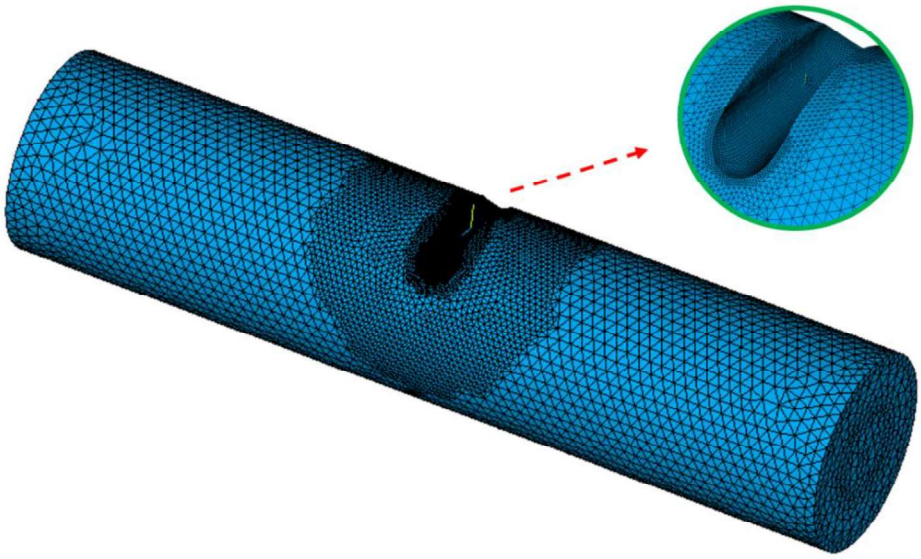

Figure 4.42. The finite element model of 34CrNiMo6 shaft with a lateral U-shaped notch.

The specimen is subjected to various combinations of synchronized periodic bending and torsion. Figure 4.43 shows the boundary conditions applied to the part. As can be seen

from the figure, no extra section that carries the boundary conditions is defined for this geometry. Instead, the elements in sufficiently large regions at either ends of the sample are excluded in the calculations so that the highly stressed zones formed around the application points of the loads do not affect the results. Bending moments are generated via a pair of forces applied to one end of the bar in the z-direction equal in magnitude but oppositely directed and twisting moments are generated by a force couple in y direction. The nodes on the other end are fixed.

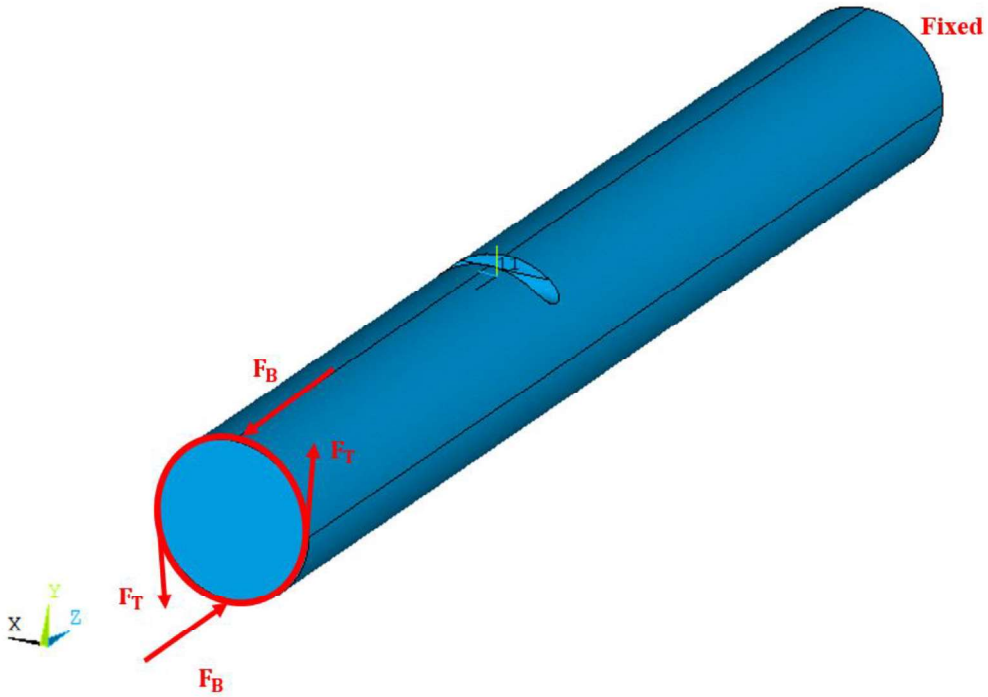

Figure 4.43. Boundary conditions of 34CrNiMo6 specimen with a lateral U-shaped notch.

The validity of the model for this geometry is examined by comparing model predictions with the experimental results reported in [4,50,51]. Fatigue lives calculated for various load levels are presented in Table 4.19 together with those determined experimentally by Branco and his co-workers [4,50,51]. Although large fluctuations are observed for a few values, in general, a good similarity in terms of increasing / decreasing trends of fatigue lives is obtained. The correlation coefficient between the two data sets is calculated as 0.86. The convergence of the model estimates to the empirical values can be seen in more detail from Figure 4.44. Also, the scatter map of the results is given in Figure 4.45. The mean square error of the scatter is 4.53.

Table 4.19. Experimental results for 34CrNiMo6 specimen with a lateral U-shaped notch reported in [4,50,51] and the estimates of the present model for given asymmetric loads.

Loading Case	Alternating Nominal Normal Stress (MPa)	Mean Normal Stress	Stress Ratio $R = \frac{\sigma_{min}}{\sigma_{max}}$	Alternating Nominal Shear Stress (MPa)	Mean Shear Stress	Biaxiality Ratio $\lambda = \frac{\sigma_a}{\tau_a}$	Experimental Life	Predicted Life
1	179.1	194	0.04	44.8	48.5	4	102,386	569,326
2	223.8	238.7	0.03	56	59.7	4	49,103	54,156
3	298.4	313.3	0.02	74.6	78.3	4	24,207	1,607
4	179.1	194	0.04	89.6	97	2	77,527	172,126
5	223.8	238.7	0.03	111.9	119.4	2	26,317	13,742
6	298.4	313.3	0.02	149.2	156.7	2	8,314	749
7	179.1	189	0.03	134.3	141.8	1.333	50,261	35,195
8	223.8	233.8	0.02	167.9	175.4	1.333	17,967	3,178
9	298.4	308.4	0.02	223.8	231.3	1.333	4,099	2,420
10	197.4	208.1	0.03	0	0	-	100,425	352,100
11	218.8	229.3	0.02	0	0	-	53,742	119,794
12	219.3	228.5	0.02	0	0	-	37,108	117,804
13	288.6	297.6	0.02	0	0	-	13,816	4,323

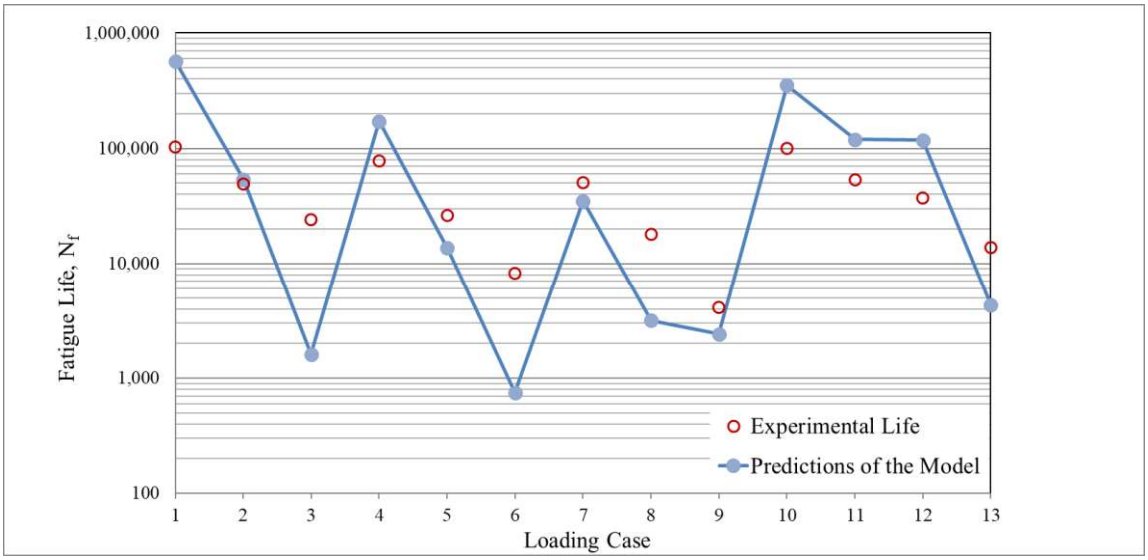

Figure 4.44. Correlation between experimental and theoretical fatigue lives of 34CrNiMo6 specimen with a lateral U-shaped notch.

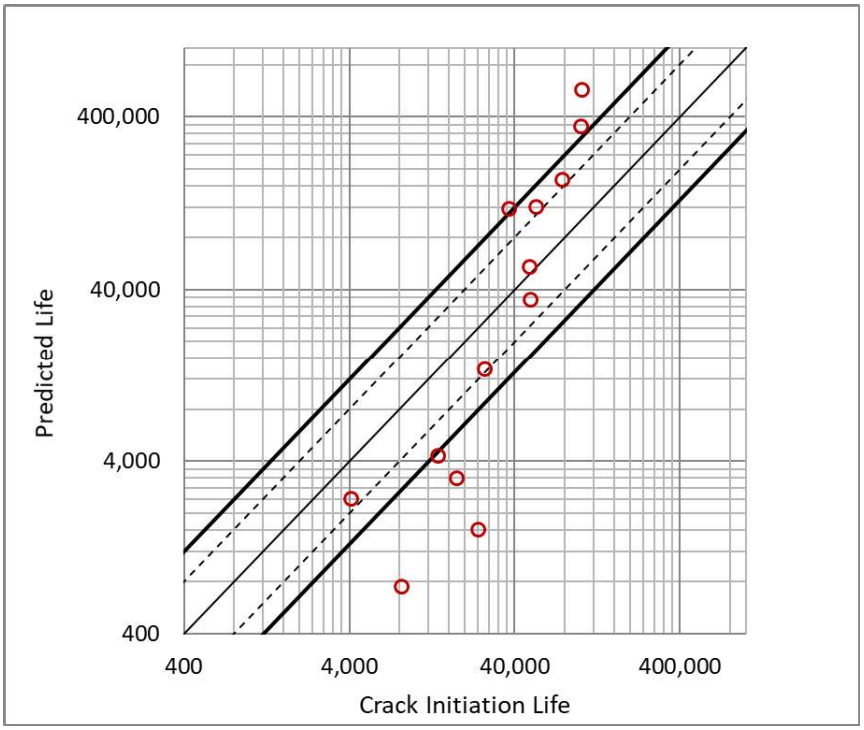

Figure 4.45. Experimental vs. predicted fatigue life for 34CrNiMo6 specimen with a lateral U-shaped notch in the presence of asymmetric loads.

Figure 4.46 shows the contour plot of the equivalent stress around the notch where the calculated fatigue life is shorter than the threshold life, N_f^{th}, corresponding to the 7th loading case in Table 4.19. In this geometry, only a small region around the notch is critical, that means only the elements in close proximity to the notch have calculated fatigue lives shorter than the threshold life. Besides, the maximum equivalent stress is obtained as 1458 MPa using the linear elastic FE analysis. This value exceeds even the ultimate strength of the material. That means significant plastic deformation occurs at the notch. Even though the stress levels are not accurate, fatigue-life calculations based on strain energy approximates the measured lives.

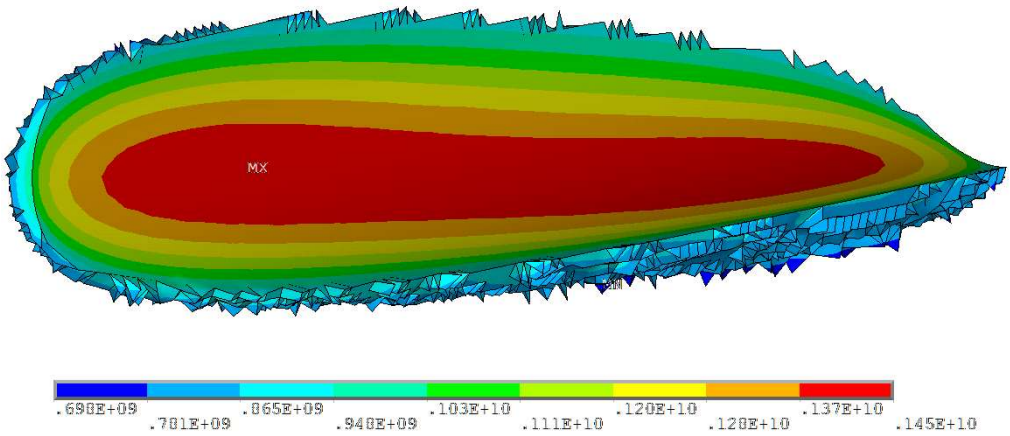

Figure 4.46. Equivalent-stress contour plot of the region where fatigue life is shorter than the threshold life, N_f^{th}.

An overall comparison between the experimental results and the model estimates for all examined specimens in this section is given in Figure 4.47 and Figure 4.48, for fully reversed and asymmetric loading conditions, respectively.

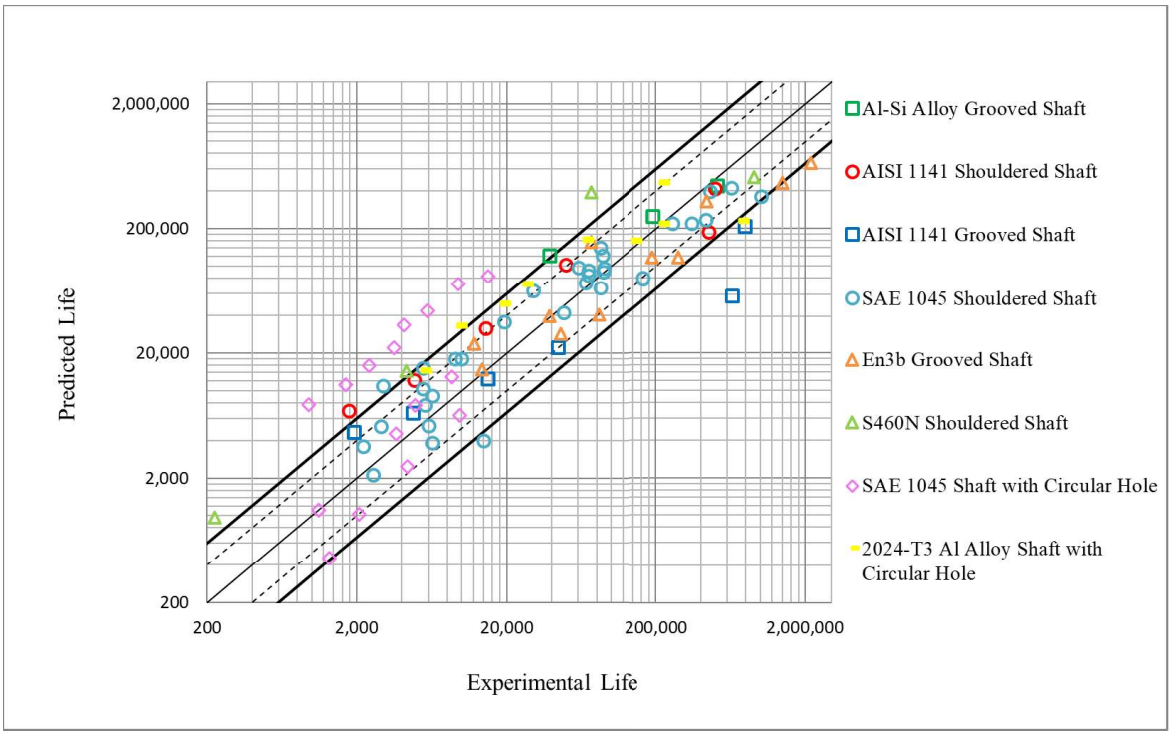

Figure 4.47. An overall comparison between the experimental results and the model estimates for fully reversed proportional loading.

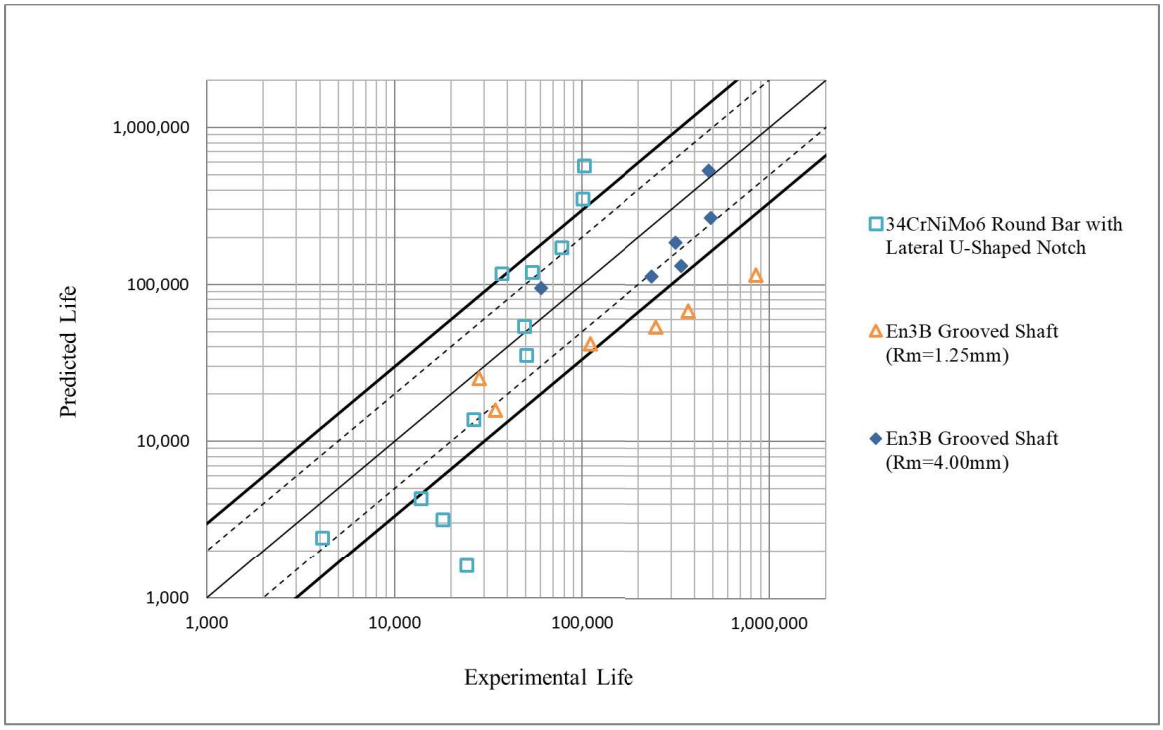

Figure 4.48. An overall comparison between the experimental results and the model estimates in the presence of asymmetric loads.

5. CONCLUSIONS

In the present study, a new strain energy based multiaxial fatigue analysis methodology is proposed to estimate high cycle fatigue life of structures with geometric irregularities leading to stress concentration. A new energy parameter called equivalent strain energy density is introduced as a measure of material damage. The Coffin-Manson-Basquin type relationship is adapted to relate the new parameter to the number of cycles to failure. The contribution of plastic deformation to material damage is assumed to be small in high-cycle fatigue compared to elastic deformation. Accordingly, the value of the newly defined parameter is computed based solely on elastic strain energy distribution within the parts. Stress and strain states prevailing on the part are determined by a finite element analysis. The material is assumed be linear elastic. Only the elements around the notch having calculated fatigue life shorter than the threshold life are considered in fatigue evolution.

The presented model can be applied to the parts under constant amplitude proportional loading conditions. In addition to fully reversed loads, the model is well adapted to asymmetric loads with a non-zero mean stress. On the other hand, since the determination of the degree of material hardening caused by asynchronous loads requires additional analysis, the effects of non-proportional loads is not considered in the presented model. Accounting for the effects of non-proportional loads remains as a future study.

The reliability of the proposed methodology is validated using extensive experimental data from the literature. The predicting performance of the model is checked for 10 different specimen geometries made of 7 different materials (Al-Si alloy, AISI 1141, SAE 1045, En3B, 2024-T3 Al alloy, S460N and DIN 34CrNiMo6). Four different notch geometries are considered; V-shaped circumferential groove, fillet, circular transverse hole, and lateral U-shaped groove. The specimens examined in this study are subjected to either various bending and torsion combinations or torsion combined with axial loads.

The agreement between the empirical fatigue lives and theoretical estimates for proportional loading is fairly good. 77% of the predictions obtained for 88 different test

conditions fall within the scatter band with a factor of 3. Moreover, the model adequately accounts for the non-zero mean stress effect. 60% of the predictions obtained from the model for 25 test conditions with asymmetric loads remain within the error factor of about 3 compared to the experimental data. Differences between the correlation coefficients calculated for different specimens may be attributed to the inconsistency in some test data or to the fact that material properties and experimental results for some specimens are provided from different sources in this study. On the other hand, considering that, low correlations are observed for specimens with circular holes, it may be due to fact that the presented fatigue-life assessment model may show different predicting performance for diverse notch geometries. Nevertheless, on the whole, it can be said that the proposed methodology is highly promising. As long as extensive local yielding does not occur, it can give accurate estimations.

The formulation contains only material constants available in material data sheets. Applicability of the proposed approach is independent of specimen geometry as well as loading conditions. On the other hand, experimental verification of the model is carried out by considering only the samples with standard notch geometries. Ensuring the general applicability of the presented methodology for arbitrary geometries requires a more comprehensive study.

APPENDIX A: FATIGUE LIFE PREDICTIONS IN ABSENCE OF CYCLIC PROPERTIES

As one may remember, since only monotonic characteristics are given for En3B steel in the reference [1], Muralidharan-Manson modified universal slopes method was utilized in Section 4.2.4 to approximate cyclic properties of that material. In order to make certain of the followed course's reliability, said approximation is further applied to some of the other examined specimens made of various steel materials.

Approximate solutions obtained for AISI 1141 shouldered shaft and grooved shaft specimens are listed in Table A.1 and Table A.2, respectively. To determine the fatigue properties approximately, the static material values given in Table 4.5 is used.

Table A.1. Approximate solution results for AISI 1141 shouldered shaft specimen.

Loading Case	Nominal Tensile Stress (MPa)	Nominal Torsional Stress (MPa)	Experimental Life	Predicted Life	Predicted Life (Approximate Solution)	$\frac{\text{Predicted Life (app)}}{\text{Predicted Life}}$
1	0	344	1,767	6,916	9,950	1.439
2	260	274	4,865	12,122	16,730	1.380
3	0	294	14,492	31,691	44,030	1.389
4	201	214	49,713	102,432	134,993	1.318
5	0	240	452,785	188,813	246,620	1.306
6	140	154	499,081	418,472	433,507	1.036

Table A.2. Approximate solution results for AISI 1141 grooved shaft specimen.

Loading Case	Nominal Tensile Stress (MPa)	Nominal Torsional Stress (MPa)	Experimental Life	Predicted Life	Predicted Life (Approximate Solution)	$\frac{\text{Predicted Life (app)}}{\text{Predicted Life}}$
1	0	344	1,923	4,631	5,666	1.223
2	260	274	4,732	6,673	7,407	1.110
3	0	294	14,912	12,470	16,349	1.311
4	201	214	44,071	22,057	28,753	1.304
5	0	240	645,000	58,476	76,382	1.306
6	140	154	789,999	209,783	261,898	1.248

The goodness of fit of the results is visualized with the subsequent conformity and dispersion graphs.

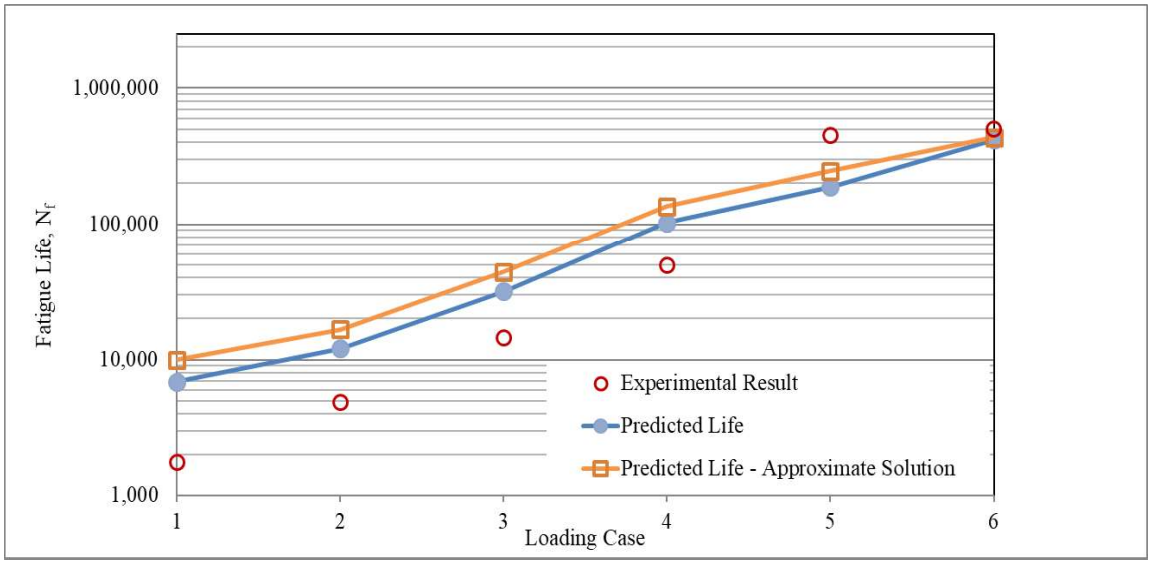

Figure A.1. Conformity of the approximate solution for AISI 1141 shouldered shaft specimen.

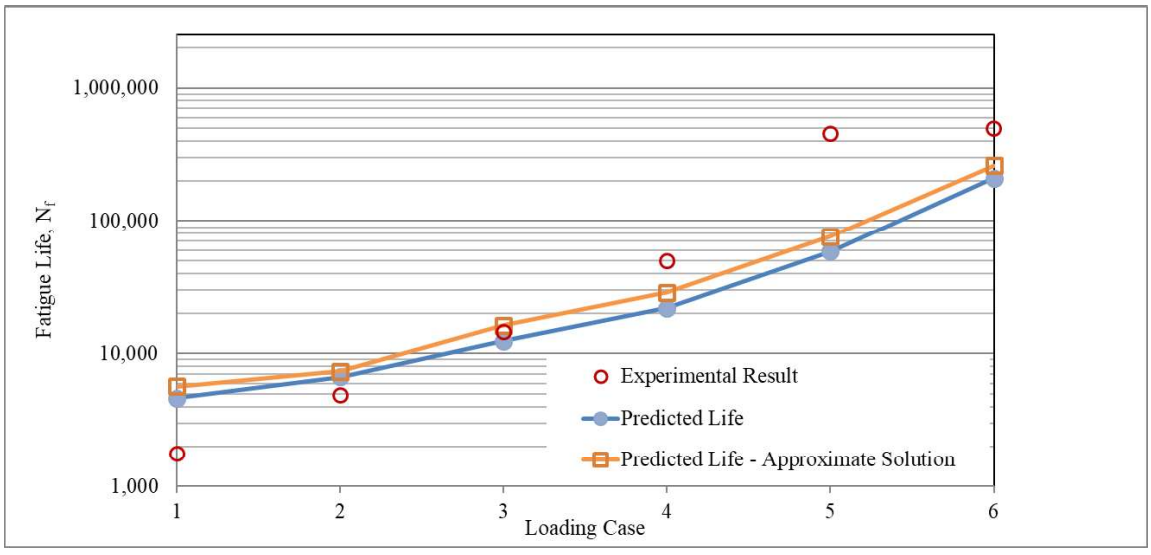

Figure A.2. Conformity of the approximate solution for AISI 1141 grooved shaft specimen.

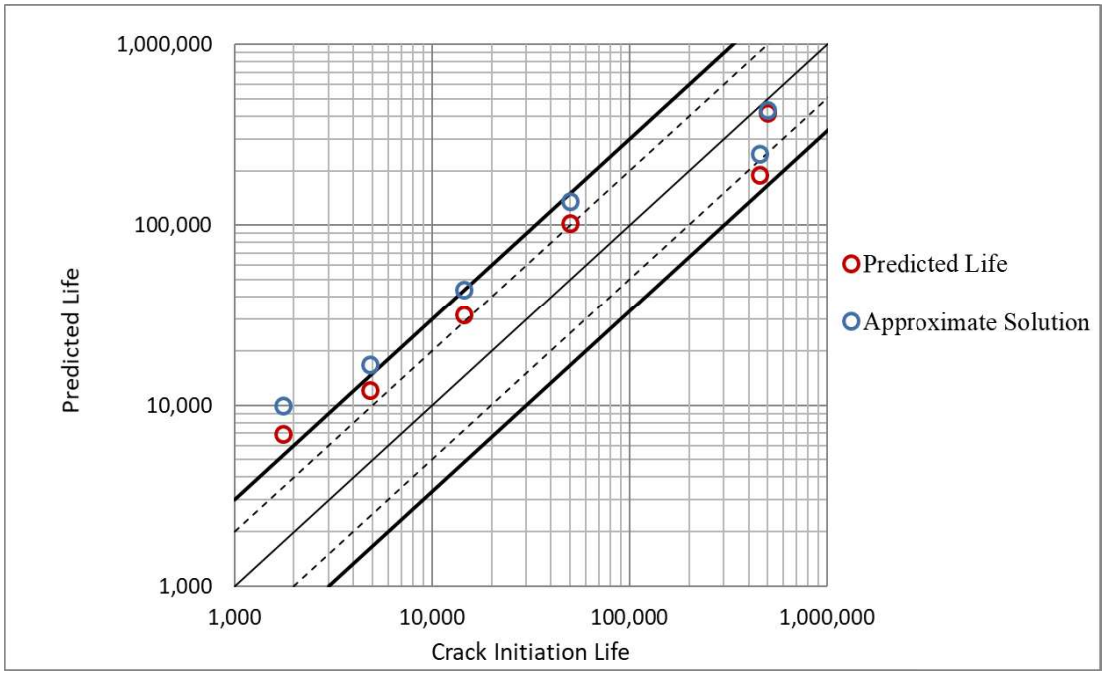

Figure A.3. A comparative dispersion chart for approximate solution related to AISI 1141 shouldered shaft specimen.

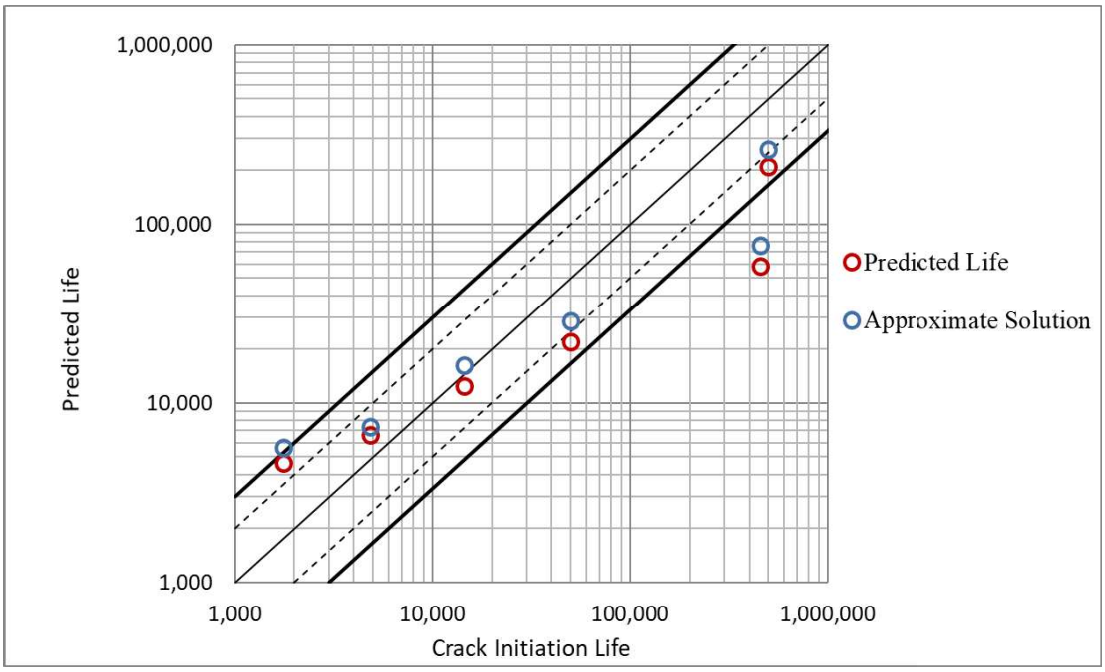

Figure A.4. A comparative dispersion chart for approximate solution related to AISI 1141 grooved shaft specimen.

Similar procedure is followed for SAE 1045 shouldered shaft specimen. The number of cycles to failure calculated based on the uncertain material values obtained with equation 4.5 can be accessed from Table A.3.

Table A.3. Approximate solution results for SAE 1045 shouldered shaft specimen.

Loading Case	Nominal Bending Moment (N.m)	Nominal Torsional Moment (N.m)	Final Fracture Life	Experimental Life for Initiation of 1-mm Crack	Predicted Life (Approximate Solution)
1	1,850	2,550	5,113	2,200	4,589
2	2,800	0	8,262	2,571	2,156
3	1,250	2,700	10,420	6,402	14,119
4	1,850	2,100	11,565	5,740	11,047
5	1,355	2,550	11,630	5,500	16,306
6	2,325	1,350	11,735	2,905	6,521
7	2,000	2,100	12,050	5,998	6,959
8	0	3,000	12,124	5,529	25,920
9	1,150	2,700	12,700	3,000	17,545
10	2,600	0	15,043	6,347	4,199
11	2,586	0	17,450	14,000	4,399
12	851	2,700	17,730	9,000	31,374
13	840	2,700	24,540	10,000	31,658
14	1,720	1,350	58,790	19,260	60,625
15	1,680	960	65,049	30,000	115,102
16	1,875	0	112,200	48,180	67,793
17	1,220	1,700	124,500	60,800	204,052
18	0	2,400	132,585	70,350	202,668
19	1,680	900	153,800	84,950	120,987
20	780	2,180	156,100	70,340	181,979
21	1,730	0	157,125	67,300	132,118
22	1,220	1,710	160,900	89,750	200,004
23	570	2,180	182,250	87,830	273,331
24	1,550	1,090	190,200	88,750	174,222
25	1,300	1,400	226,000	84,680	295,627
26	1,708	0	249,900	163,800	146,006
27	845	1,800	396,800	259,900	506,087
28	1,475	0	556,400	347,500	443,010
29	1,250	880	734,750	462,500	774,309
30	1,460	0	764,000	430,000	474,689
31	990	1,390	890,500	641,500	909,512
32	0	2,000	1,843,667	1,011,333	861,834

As with the fatigue properties given for the material in question, there is no agreement in the time-independent material values. On the other hand, according to American Society for Metals' (ASM) data, the ultimate tensile strength of SAE 1045 hot rolled medium carbon steel can be taken as 565 MPa [87,88]. Taking this value as the starting point, convergence of the approximate solution results is illustrated in Figure A.5.

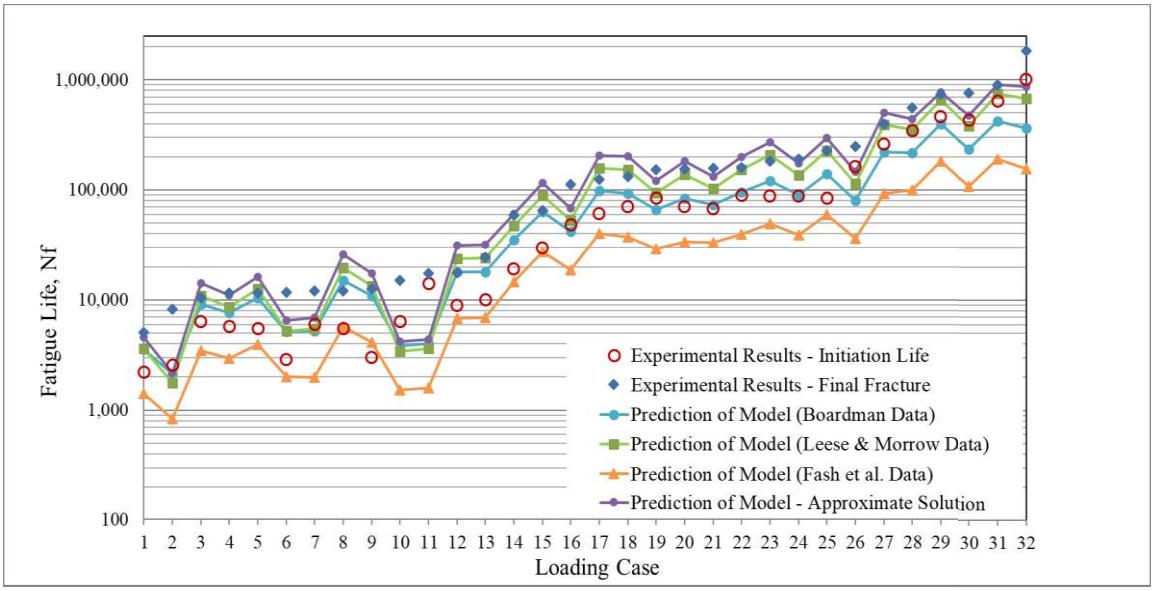

Figure A.5. Conformity of the approximate solution for SAE 1045 shouldered shaft specimen.

Similarity solutions are lastly carried out for the S460N shouldered shaft specimen. The table and figures below reflect the consistency of the values.

Table A.4. Approximate solution results for S460N shouldered shaft specimen.

Loading Case	Nominal Tensile Stress (MPa)	Nominal Torsional Stress (MPa)	Experimental Life	Predicted Life	Predicted Life (Approximate Solution)	$\frac{\text{Predicted Life (app)}}{\text{Predicted Life}}$
1	300	262	225	964	1,776	1,842
2	225	197	4,317	14,301	22,555	1,577
3	150	131	74,019	391,338	494,687	1,264
4	125	109	903,597	515,038	598,062	1,161

Figure A.6. Conformity of the approximate solution for S460N shouldered shaft specimen.

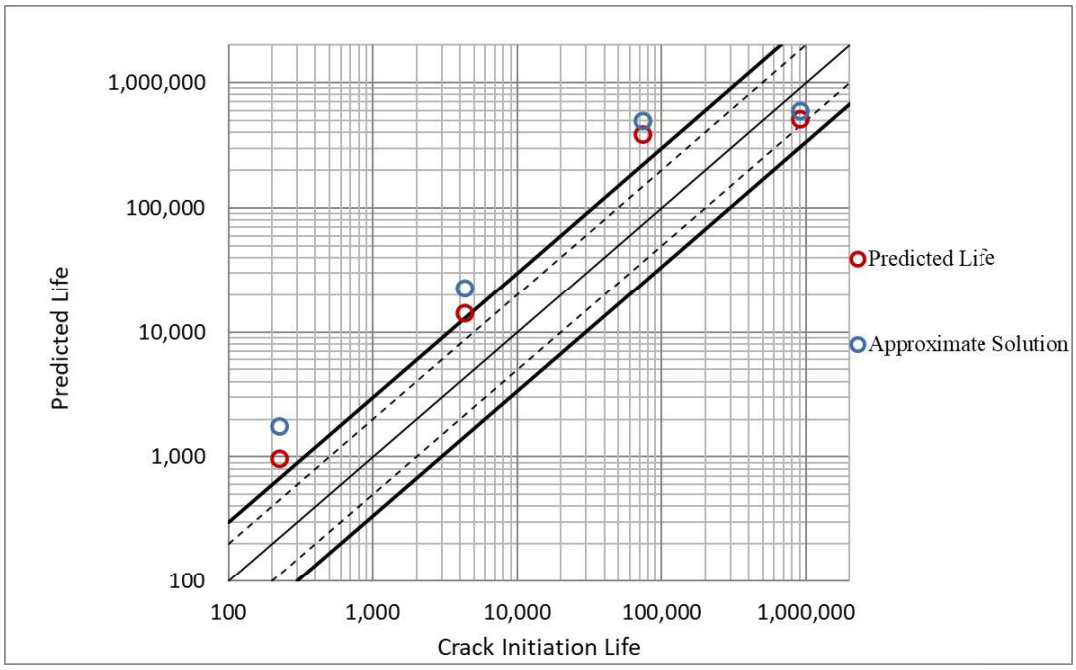

Figure A.7. A comparative dispersion chart for approximate solution related to S460N shouldered shaft specimen.

As can be seen from the numerical and visual data, the results obtained by using the material fatigue parameters calculated with the modified universal slopes method are slightly non-conservative in comparison with the estimations evaluated using experimentally determined material constants. Consequently, it is clear that the model is reasonable.

REFERENCES

1. Susmel, L., and D. Taylor, “The Modified Wöhler Curve Method Applied Along with the Theory of Critical Distances to Estimate Finite Life of Notched Components Subjected to Complex Multiaxial Loading Paths”, *Fatigue and Fracture of Engineering Materials and Structures* Vol. 31, pp. 1047-1064, 2008.

2. Carpinteri, A., A. Spagnoli, S. Vantadori and D. Viappiani, “A Multiaxial Criterion for Notch High-Cycle Fatigue Using a Critical-Point Method”, *Engineering Fracture Mechanics*, 2008, Vol. 75, No. 7, pp. 1864–1874, 2008.

3. Fatemi, A., and D. F. Socie, ‘‘A Critical Plane Approach to Multiaxial Fatigue Damage Including Out-of-phase Loading’’, *Fatigue & Fracture of Engineering Materials & Structure*, Vol. 11, No. 3, pp. 149-165, 1988.

4. Branco, R., J. D. Costa, F. Berto, and F. V. Antunes, ‘‘Fatigue Life Assessment of Notched Round Bars Under Multiaxial Loading Based on the Total Strain Energy Density Approach’’, *Theoretical and Applied Fracture Mechanics*, Vol. 97, pp. 340-348, 2018.

5. Papadopoulos, I. V., ‘‘Long Life Fatigue Under Multiaxial Loading’’, *International Journal of Fatigue,* Vol. 23, pp. 839-849, 2001.

6. Sönmez, F. Ö., and C. Ö. Karadeniz, ‘‘Fatigue Assessment of Notched Parts Under Multiaxial Loading Without Relying on Load or Geometry Factors’’, in preparation.

7. Karadeniz, C. Ö., *Strain Energy Based Fatigue Model for Notched Part Subjected to Multiaxial Loading*, M.S. Thesis, Boğaziçi University, İstanbul, 2013.

8. Neuber, H., *Theory of Notch Stresses: Principles for Exact Stress Calculation,* Edwards Brothers Inc., Ann Arbor, Michigan, 1946.

9. Neuber, H., *Theory of Notch Stresses: Principles for Exact Stress Calculation of Strength with Reference to Structural Form and Material,* 2nd edition, Springer Verlag, Berlin, 1958.

10. Peterson, R. E., ‘‘Notch Sensitivity’’, In: G. Sines, and J. L. Waisman (Eds), *Metal Fatigue,* McGraw-Hill, New York, pp. 293-306, 1959.

11. Taylor, D., ‘‘Geometrical Effects in Fatigue: A Unifying Theoretical Model’’, *International Journal of Fatigue,* Vol. 21, No. 5, pp. 413-420, 1999.

12. Bellet, D., D. Taylor, S. Marco, E. Mazzeo, J. Guillois and T. Pircher, ‘‘The Fatigue Behavior of Three-Dimensional Stress Concentrations’’, *International Journal of Fatigue,* Vol. 27, No. 3, pp. 207-221, 2005.

13. Hult, J., ‘‘CDM - Capabilities, Limitations and Promises’’, In: K. E. Easterling (Eds), *Mechanisms of Deformation and Fracture,* Pergamon, Oxford, pp. 233-247, 1979.

14. Lemaitre, J., and J. L. Chaboche, ‘‘Aspect Phénoménologique de la Rupture par Endommagement’’, *Journal de Mécanique Appliquée*, Vol. 2, No. 3, pp. 317-365, 1978.

15. Lemaitre, J., ‘‘Damage Modelling for Prediction of Plastic or Creep Fatigue Failure in Structures’’, In: IASMiRT, *5th International Conference on Structural Mechanics in Reactor Technology,* Berlin, 1979, North-Holland Publishing Co., Netherlands, 1979.

16. Lemaitre, J., ‘‘A Continuous Damage Mechanics Model for Ductile Fracture’’, *Journal of Engineering Materials and Technology, Transactions of the ASME*, Vol. 107, No. 1, pp. 83-89, 1985.

17. Chaboche, J. L., ‘‘Continuous Damage Mechanics: A Tool to Describe Phenomena Before Crack Initiation’’, *Nuclear Engineering and Design,* Vol. 64, No. 2, pp. 233-247, 1981.

18. Chaboche, J. L., ‘‘Continuum Damage Mechanics: Part I - General Concepts’’, *Journal of Applied Mechanics, Transactions ASME*, Vol. 55, No. 1, pp. 59-64, 1988.

19. Chaboche, J. L., ‘‘Continuum Damage Mechanics: Part II - Damage Growth, Crack Initiation, and Crack Growth’’, *Journal of Applied Mechanics,* Vol. 55, No. 1, pp. 65-72, 1988.

20. Krajcinovic, D., ‘‘Constitutive Equations for Damaging Materials’’, *Journal of Applied Mechanics,* Vol. 50, pp. 355-360, 1983.

21. Krajcinovic, D., and G. U. Fonseka, ‘‘The Continuous Damage Theory of Brittle Materials: Part 1 and Part 2’’, *Journal of Applied Mechanics, Transactions of the ASME*, Vol. 48, pp. 809-824, 1981.

22. Taylor, D., *The Theory of Critical Distances: A New Perspective in Fracture Mechanics,* Elsevier Science Ltd., 2007.

23. Brown, M. W., and K. J. Miller, ‘‘A Theory for Fatigue Under Multiaxial Stress-Strain Conditions’’, *Proceedings of the Institution of Mechanical Engineers,* Vol. 187, No. 1, pp. 745-755, 1973.

24. Socie, D. F., ‘‘Multiaxial Fatigue Damage Models’’, *ASME Journal of Engineering Materials and Technology*, Vol. 109, pp. 293-298, 1987.

25. Smith, K. N., P. Watson, and T. H. Topper, ‘‘ A Stress-Strain Function for the Fatigue of Materials’’, *Journal of Materials*, Vol. 5, No. 4, pp. 767-778, 1970.

26. Shamsaei, N., and A. Fatemi, ‘‘Effect of Hardness on Multiaxial Fatigue Behaviour and Some Simple Approximations for Steels’’, *Fatigue and Fracture of Engineering Materials and Structures*, Vol. 32, No. 8, pp. 631-646, 2009.

27. Fatemi, A., N. Shamsaei, ‘‘Multiaxial Fatigue: An Overview and Some Approximation Models for Life Estimation’’, *International Journal of Fatigue*, Vol. 33, No. 8, pp. 948-958, 2011.

28. Roessle, M. L., and A. Fatemi, ‘‘Strain-Controlled Fatigue Properties of Steels and Some Simple Approximations’’, *International Journal of Fatigue*, Vol. 22, No. 6, pp. 495-511, 2000.

29. Lagoda, T., and E. Macha, ‘‘Energy-Based Approach to Damage Cumulation in Random Fatigue’’, In: R. A. Smith (Eds), *Reliability Assessment of Cyclically Loaded Engineering Structures*, Kluwer Academic Publishers, pp. 435-442, 1997.

30. Lagoda, T., and E. Macha, ‘‘Energy Approach to Fatigue Under Combined Cyclic Bending with Torsion of smooth and Notched Specimens’’, *Materials Science,* Vol. 34, No. 5, pp. 630-639, 1998.

31. Neuber, H., ‘‘Theory of Stress Concentration for Shear-Strained Prismatical Bodies With Arbitrary Nonlinear Stress-Strain Law’’, *Journal of Applied Mechanics, Transactions of the ASME*, Vol. 28, pp. 544-550, 1961.

32. Molski, K., G. Glinka, ‘‘A Method of Elastic-Plastic Stress and Strain Calculation at A Notch Root’’, *Materials Science and Engineering*, Vol. 50, No. 1, pp. 93-100, 1981.

33. Papadopoulos, I. V., Fatigue Limit of Metals Under Multiaxial Stress Conditions: The Microscopic Approach, Technical note no. 1.93.101, ISEI/IE 2495/93. Commission of the European Communities, Joint Research Centre, 1993.

34. Carpinteri, A., and A. Spagnoli, ‘‘Multiaxial High-Cycle Fatigue Criterion for Hard Metals’’, *International Journal of Fatigue,* Vol. 23, pp. 135-145, 2001.

35. Carpinteri, A., A. Spagnoli, C. Ronchei, and S. Vandatori, ‘‘A Strain-Based Multiaxial Fatigue Criterion Connected to the Critical Plane Approach’’, *Procedia Engineering,* Vol. 74, pp. 317-320, 2014.

36. Socie, D. F., L. A. Waill, and D. F. Dittmer, ‘‘Biaxial Fatigue of Inconel 718 Including Mean Stress Effects’’, In: K. J. Miller, and M. W. Brown (Eds), *STP853-EB Multiaxial Fatigue,* ASTM International, West Conshohocken, PA, pp. 463-481, 1985.

37. Fatemi, A., and R. I. Stephens, ‘‘Biaxial Fatigue of 1045 Steel Under In-phase and 90 Degree Out-of-phase Loading’’, In: E. L. Gail, and D. F. Socie (Eds), *Multiaxial Fatigue: Analysis and Experiments, AE-14,* SAE International, Warrendale, pp. 121-138, 1989.

38. Susmel, L., and P. Lazzarin, ‘‘Bi-parametric Wöhler Curve for High Cycle Multiaxial Fatigue Assessment’’, *Fatigue and Fracture of Engineering Materials and Structures,* Vol. 25, pp. 63-78, 2002.

39. Papadopoulos, I. V., ‘‘Critical Plane Approaches in High-cycle Fatigue: On the Definition of the Amplitude and Mean Value of the Shear Stress Acting on the Critical Plane’’, *Fatigue and Fracture of Engineering Materials and Structures,* Vol. 21, pp. 269-285, 1998.

40. Lazzarin, P., and L. Susmel, ‘‘A Stress-Based Method to Predict Lifetime Under Multiaxial Fatigue Loadings’’, *Fatigue and Fracture of Engineering Materials and Structures,* Vol. 26, pp. 1171-1187, 2003.

41. Walat, K., M. Kurek, P. Ogonowski, and T. Lagoda, ‘‘The Multiaxial Random Fatigue Criteria Based on Strain and Energy Damage Parameters on the Critical Plane for the Low-Cycle Range’’, *International Journal of Fatigue,* Vol. 37, pp. 100-111, 2012.

42. Glinka, G., G. Shen, and A. Plumtree, ‘‘A Multiaxial Fatigue Strain Energy Density Parameter Related to the Critical Plane’’, *Fatigue and Fracture of Engineering Materials and Structures*, Vol. 18, No. 1, pp. 37-46, 1995.

43. Varvani-Farahani, A., ‘‘A New Energy-Critical Plane Parameter for Fatigue Life Assessment of Various Metallic Materials Subjected to In-Phase and Out-of-Phase Multiaxial Fatigue Loading Conditions’’, *International Journal of Fatigue*, Vol. 22, pp. 295-305, 2000.

44. Ince, A., and G. Glinka, ‘‘A Generalized Damage Parameter for Multiaxial Fatigue Life Prediction Under Proportional and Non-Proportional Loadings’’, *International Journal of Fatigue*, Vol. 62, pp. 34-41, 2014.

45. Susmel, L., G. Meneghetti, and B. Atzori, ‘‘A Simple and Efficient Reformulation of the Classical Manson–Coffin Curve to Predict Lifetime Under Multiaxial Fatigue Loading. Part I: Plain Materials’’, *Journal of Engineering Materials and Technology, Transactions of the ASME*, Vol. 131, No. 2, pp. 021009 [1-9], 2009.

46. Susmel, L., G. Meneghetti, and B. Atzori, ‘‘A Simple and Efficient Reformulation of the Classical Manson–Coffin Curve to Predict Lifetime Under Multiaxial Fatigue Loading. Part II: Notches’’, *Journal of Engineering Materials and Technology, Transactions of the ASME*, Vol. 131, No. 2, pp. 021010 [1-8], 2009.

47. Liu, X. Y., T. X. Su, Y. Zhang, and M. N. Yuan, ‘‘A Multiaxial High-Cycle Fatigue Life Evaluation Model for Notched Structural Components’’, *International Journal of Fatigue*, Vol. 80, pp. 443-448, 2015.

48. Carpinteri, A., M. Kurek, T. Łagoda, and S. Vandatori, ‘‘Estimation of Fatigue Life Under Multiaxial Loading by Varying the Critical Plane Orientation’’, *International Journal of Fatigue*, Vol. 100, pp. 512-520, 2017.

49. ASTM E 739-91, ‘‘Standard Practice for Statistical Analysis of Linear or Linearized Stress-Life (S-N) and Strain Life Fatigue Data’’, In: Annual Book of ASTM Standards, Vol. 03.01, Philadelphia, pp. 614-628, 1999.

50. Branco, R., P. A. Prates, J. D. Costa, F. Berto, and A. Kotousov, ‘‘New Methodology of Fatigue Life Evaluation for Multiaxially Loaded Notched Components Based on Two Uniaxial Strain-Controlled Tests’’, *International Journal of Fatigue*, Vol. 111, pp. 308-320, 2018.

51. Branco, R., P. A. Prates, J. D. Costa, L. P. Borrego, F. Berto, A. Kotousov, and F. V. Antunes, ‘‘Rapid Assessment of Multiaxial Fatigue Lifetime in Notched Components Using An Averaged Strain Energy Density Approach’’, *International Journal of Fatigue*, Vol. 124, pp. 89-98, 2019.

52. Ellyin, F., *Fatigue Damage, Crack Growth and Life Prediction*, Chapman & Hall, London, 1997.

53. Liao, D., and S. P. Zhu, ‘‘Energy Field Intensity Approach for Notch Fatigue Analysis’’, *International Journal of Fatigue*, Vol. 127, pp. 190-202, 2019.

54. Yao W. X., ‘‘Stress Field Intensity Approach for Predicting Fatigue Life’’, *International Journal of Fatigue*, Vol. 15, No. 3, pp. 243-246, 1993.

55. Brown, M. W., and K. J. Miller, ‘‘Mode I Fatigue Crack Growth Under Biaxial Stress at Room and Elevated Temperature’’, In: K. J. Miller, and M. W. Brown (Eds), *STP853 Multiaxial Fatigue,* American Society for Testing and Materials, Philadelphia, pp. 135-152, 1985.

56. Dugdale, D. S., ‘‘Yielding of Steel Sheets Containing Slits’’, *Journal of the Mechanics and Physics of Solids,* Vol. 8, No. 2, pp. 100-104, 1960.

57. Bilby, B. A., A. H. Cottrell, and K. H. Swinden, ‘‘The Spread of Plastic Yield from A Notch’’, *Proceedings of the Royal Society London*, Series A, Vol. 272, No. 1350, pp. 304-314, 1963.

58. Tomkins, B., ‘‘Fatigue Crack Propogation-An Analysis’’, *The Philosophical Magazine: A Journal of Theoretical Experimental and Applied Physics,* Vol. 18, No. 155, pp. 1041-1066, 1968.

59. Brown, M. W., H. W. Liu, A. P. Kfouri, and K. J. Miller, ‘‘An Analysis of Fatigue Crack Growth Under Yielding Conditions’’, In: D. Francois (Eds), *Advances in Fracture Research,* Pegamon Press, Oxford, Vol. 2, pp. 891-898, 1980.

60. Paris, P. C., ‘‘The Fracture Mechanics Approach to Fatigue’’, In: J. J. Burke, N. L. Reed, and V. Weiss (Eds), *Fatigue-An Interdisciplinary Approach,* Syracuse University Press, Syracuse, N. Y., pp. 107-127, 1964.

61. Tanaka, K., ‘‘Fatigue Crack Propagation from a Crack Inclined to the Cyclic Tensile Axis’’ *Engineering Fracture Mechanics,* Vol. 6, No. 1, pp. 493-507, 1974.

62. Qian, J., and A. Fatemi, ‘‘Mixed Mode Fatigue Crack Growth: A Literature Survey’’, *Engineering Fracture Mechanics*, Vol. 55, No. 6, pp. 969-990, 1996.

63. Xiangqiao, Y., D. Shanyi, and Z. Zehua, ‘‘Mixed Mode Fatigue Crack Growth Prediction in Biaxially Stretched Sheets’’, *Engineering Fracture Mechanics*, Vol. 43, No. 3, pp. 471-475, 1992.

64. Kujawski, D., ‘‘A Fatigue Crack Driving Force Parameter with Load Ratio Effects’’, *International Journal of Fatigue*, Vol. 23, pp. 239-246, 2001.

65. Walker, K., ‘‘The Effect of Stress Ratio During Crack Propagation and Fatigue for 2024-T3 and 7075-T6 Aluminum’’, In: M. Rosenfeld (Eds), *STP462-EB Effects of Environment and Complex Load History on Fatigue Life*, Atlanta, 1968, ASTM International, West Conshohocken Philadelphia, pp. 1-14, 1970.

66. Noroozi, A. H., G. Glinka, and S. Lambert, ‘‘A Two Parameter Driving Force for Fatigue Crack Growth Analysis’’, *International Journal of Fatigue*, Vol. 27, pp. 1277-1296, 2005.

67. Morrow, J. D., ‘‘Cyclic Plastic Strain Energy and Fatigue of Metals’’, In: B. Lazan (Eds), *ASTM STP 378 Internal Friction, Damping, and Cyclic Plasticity,* ASTM International, West Conshohocken Philadelphia, pp. 45-87, 1965.

68. Basquin, O. H., ‘‘The Exponential Law of Endurance Tests’’, *Proceedings of the American Society for Testing and Materials,* Vol. 10, pp. 625-630, 1910.

69. Liu, X. Y., T. X. Su, Y. Zhang, and M. N. Yuan, ‘‘A Multiaxial High-Cycle Fatigue Life Evaluation Model for Notched Structural Components’’, *International Journal of Fatigue,* Vol. 80, pp. 443-448, 2015.

70. Walat, K., and T. Łagoda, ‘‘Lifetime of Semi-Ductile Materials Through the Critical Plane Approach’’, *International Journal of Fatigue*, Vol. 67, pp. 73-77, 2014.

71. Lagoda, T., G. Robak, and J. Slowik, “Fatigue Life of Steel Notched Elements Including the Complex Stress State”, *Materials and Design*, Vol. 51, pp. 935-942, 2013.

72. Gates, N., A. Fatemi, “Notch Deformation and Stress Gradient Effects in Multiaxial Fatigue”, *Theoretical and Applied Fracture Mechanics,* Vol. 84, pp. 3-25, 2016.

73. Fırat, M., “A Numerical Analysis of Combined Bending-Torsion Fatigue of SAE Notched Shaft”, *Finite Elements in Analysis and Design,* Vol. 54, pp. 16-27, 2012.

74. Fash, J. W., D. F. Socie, and D. L. McDowell, ‘‘Fatigue Life Estimates for a Simple Notched Component Under Biaxial Loading’’, In: K. J. Miller, and M. W. Brown (Eds), *STP853 Multiaxial Fatigue,* American Society for Testing and Materials, Philadelphia, pp. 497-513, 1985.

75. Leese G. E., and J. Morrow, ‘‘Low Cycle Fatigue Properties of a 1045 Steel in Torsion’’, In: K. J. Miller, and M. W. Brown (Eds), *STP853 Multiaxial Fatigue,* American Society for Testing and Materials, Philadelphia, pp. 482-496, 1985.

76. Boardman, B. ‘‘Fatigue Resistance of Steels’’, *Properties and Selection: Irons, Steels, and High-Performance Alloys,* ASM Handbook, Vol. 1, ASM International, pp. 673-688, 1990.

77. Manson, S. S., ‘‘Fatigue: A Complex Subject – Some Simple Approximations’’, *Exp. Mech. SESA,* Vol. 5, No. 1, pp. 193-226, 1965.

78. Bäumel, A., T. Seeger, and C. Boller, *Materials Data for Cyclic Loading: Supplement 1,* Elsevier Science Publishers, Amsterdam, 1990.

79. Muralidharan, U., and S. S. Manson, ‘‘A Modified Universal Slopes Equation for Estimation of Fatigue Characteristics of Metals’’, *Journal of Engineering Materials and Technology*, Vol. 110 No.1, pp. 55-58, 1988.

80. Shamsaei, N., and S. A. McKelvey. “Multiaxial Life Predictions in the Absence of Any Fatigue Properties” *International Journal of Fatigue*, Vol. 67, pp. 62-72, 2014.

81. Kurath, P., S. D. Downing, and D. R. Galliart, ‘‘Summary of Non-Hardened Notched Shaft-Round Robin Program’’, In: G. E. Leese and D. F. Socie (Eds), *Multiaxial Fatigue: Analysis and Experiments, AE-14,* SAE International, Warrendale, PA, pp. 13-32, 1989.

82. Yip, M. C., and Y. M. Jen, ‘‘Biaxial Fatigue Crack Initiation Life Prediction of Solid Cylindrical Specimens with Transverse Circular Holes’’, *International Journal of Fatigue*, Vol. 18, pp. 111-117, 1996.

83. Susmel, L., *Multiaxial Notch Fatigue, From Nominal to Local Stress-Strain Quantities*, Woodhead Publishing, Cambridge, 2009.

84. Hoffmeyer, J., R. Döring, T. Seeger, and M. Vormwald, “Deformation Behaviour, Short Crack Growth and Fatigue Lives Under Multiaxial Nonproportional Loading”, *International Journal of Fatigue*, Vol. 28, pp. 508–520, 2006.

85. Sines, G., ‘‘The Prediction of Fatigue Fracture Under Combined Stresses at Stress Concentrations’’, *Bulletin of JSME,* Vol. 4, pp. 443-53, 1961.

86. Smith, J. O., ‘‘Effect of Range of Stress on Fatigue Strength of Metals’’ *University of Illinois, Engineering Experiment Station*, Bulletin No. 334, Vol. 39, 1942.

87. Delgado, F., ‘‘Failure Analysis of a Removable Support of a Cockpit Seat in a STOL Airplane’’, In: Abdel Wahab M. (Eds), *Proceedings of the 7th International Conference on Fracture Fatigue and Wear,* Belgium, 2018, Springer, Singapore, 2018.

88. Davis, J. R. (Eds), *ASM Specialty Handbook - Carbon and Alloy Steels*, ASM International, Metals Park, OH, 1996.